Dissertation

New Concepts in Interfacial Dipole Engineering by Self-Assembled Monolayers

Eric Sauter

2018

INAUGURAL-DISSERTATION

zur

Erlangung der Doktorwürde

der

Naturwissenschaftlich-Mathematischen
Gesamtfakultät

der

Ruprecht-Karls-Universität
Heidelberg

vorgelegt von

M.Sc. Eric Sauter
aus Speyer

Tag der mündlichen Prüfung: 16.11.2018

New Concepts in Interfacial Dipole Engineering by Self-Assembled Monolayers

Gutachter:

Prof. (apl) Dr. Michael Zharnikov

Prof. (apl) Dr. Hans-Robert Volpp

To my wife Désirée and my family.

Zusammenfassung

Selbst-aggregierende Monolagen (SAMs) werden häufig für die Grenzflächentechnik in der organischen Elektronik und Photovoltaik eingesetzt. Von besonderem Interesse ist die Manipulation von Injektionsbarrieren durch Einführung eines bestimmten Dipolmoments an den Grenzflächen zwischen Elektroden und benachbarten organischen Schichten (z.B. einem organischen Halbleiter (OSC)). Diese Manipulation wird in der Regel durch die Auswahl einer geeigneten dipolaren Endgruppe an der SAM-Umgebungsschnittstelle erreicht, die jedoch einige wesentliche Nachteile aufweist. Dieser Ansatz wurde kürzlich durch die Einbettung von Dipolgruppen in das molekulare Rückgrat von SAMs ergänzt, wobei sowohl aliphatische als auch aromatische SAMs entwickelt wurden und die gemischten aromatische SAMs mit entgegengesetzt orientierten Dipolgruppen untersucht wurden.

Das Hauptziel dieser Arbeit ist die Erweiterung und Optimierung des eingebetteten Dipol-Ansatzes, zusammen mit einigen anderen Konzepten im allgemeinen Kontext der Grenzflächendipoltechnik. Zuerst untersuchte ich die gemischten aliphatischen SAMs, die aus Molekülen bestanden, die durch eine in das Alkylgerüst (ATs) eingebettete dipolare Estergruppe in zwei verschiedenen Ausrichtungen modifiziert wurden, nämlich mit dem Dipol nach oben und unten vom Substrat ausgesehen. Mit Hilfe der Röntgenphotoelektronenspektroskopie (XPS) als Hilfsmittel zur Untersuchung der Morphologie konnte ich abschätzen, dass die gemischten SAMs homogene, intermolekulare Mischungen beider Komponenten bis auf die molekulare Ebene darstellen, wobei die Existenz von „*Hot-Spots*“ für die Ladungsinjektion ausgeschlossen ist. Die Zusammensetzung der gemischten SAMs wurde gleich dem Mischungsverhältnis beider Komponenten in Lösung gefunden, aus denen diese SAMs hergestellt wurden und ahmt diese vollständig nach, was auf eine geringe Rolle der Dipol-Dipol-Wechselwirkungen in der Gesamtbilanz der strukturbildenden Kräfte schließen lässt. Durch Variation dieser Zusammensetzung konnte die Austrittsarbeit des Goldsubstrats linear und kontrolliert im Bereich von ~1.1 eV zwischen den Endwerten der beiden Einkomponenten-Monolagen abgestimmt werden.

Als nächste Aufgabe untersuchte ich die Anwendbarkeit des eingebetteten Dipolkonzepts auf verschiedene Substrate am Beispiel von Ag(111). Die aromatischen SAMs der eingebetteten Pyrimidin-Gruppe erwiesen sich in diesem Zusammenhang als wesentlich robuster als die aliphatischen (mit eingebetteter Ester-Gruppe), was die zuerst genannten Systeme besonders im Rahmen der elektrostatischen Grenzflächentechnik nützlich macht.

Angesichts der günstigeren Eigenschaften war die folgende Aufgabe die Optimierung der aromatischen SAMs mit eingebetteter Pyrimidin-Gruppe. Dies wurde durch eine Verkürzung des molekularen Rückgrats und dem Ausschluss von aliphatischen Bausteinen erreicht. Die daraus resultierenden, optimierten Monolagen bewahrten alle vorteilhaften Eigenschaften ihrer Vorläufer, zeigten aber wesentlichen bessere elektrische Transporteigenschaften, die es unseren Partnern ermöglichten, organische Dünnschichttransistoren mit hoher Leistung und extrem niedrigem Übergangswiederstand herzustellen.

Ein weiteres vielversprechendes Werkzeug zur Abstimmung der Dipolattribute und der jeweiligen Austrittsarbeit war die Elektronenbestrahlung. Dies wurde am Beispiel von aromatischen SAMs mit der eingebetteten Pyrimidin-Gruppe und der terminalen Pyridin-Gruppe gezeigt. Das beobachtete Verhalten hängt mit spezifischen chemischen Transformationen zusammen, die das Stickstoffatom in diesen Einheiten betreffen. Es führt zu

mehreren praktischen Implikationen, einschließlich der Austrittsarbeit-Lithographie, die durch repräsentative Muster demonstriert werden konnten.

Als Alternative zur Einbettung einer Dipolgruppe wurde am Beispiel von Dithiocarbamat-basierenden SAMs eine Modifikation des Verankerungsmotivs im Rahmen der Grenzflächendipoltechnik versucht. Die Kombination der spektroskopischen und Austrittsarbeitsdaten mit den Ergebnissen der von unseren Partnern durchgeführten theoretischen Simulationen ermöglicht es, die Struktur und die elektronischen Eigenschaften dieser Monolagen sehr genau zu verstehen und den Weg für ihre Anwendung zu ebnen.

Abstract

Self-assembled monolayers (SAMs) are frequently used for interfacial engineering in organic electronics and photovoltaics. The manipulation of injection barriers by introduction of a specific dipole moment at the interfaces between the electrodes and adjacent organic layers (e.g., an organic semiconductor (OSC)) is of a particular interest. This manipulation is usually achieved by selection of a suitable dipolar terminal tail group comprising the SAM-ambient interface, which however has several essential drawbacks. This approach has been recently complemented by embedding dipolar groups into the molecular backbone of the SAMs, with both aliphatic and aromatic SAMs being engineered and mixed aromatic SAMs comprised of the molecules with the oppositely oriented dipolar groups being studied.

The major goal of this work is extension and optimization of the embedding dipole approach, along with several other concepts in general context of interfacial dipole engineering. At first, I studied the mixed aliphatic SAMs comprised of molecules which were modified by a dipolar ester group embedded into the alkyl backbone at two different orientations, viz. with the dipole directed upwards and downwards from the substrate. Applying X-ray photoelectron spectroscopy (XPS) as a morphology tool, I could estimate that the mixed SAMs represent homogeneous intermolecular mixtures of both components, down to the molecular level, excluding existence of "hot spots" for charge injection. The composition of the mixed SAMs was found to mimic fully the mixing ratio of both components in solutions from which these SAMs were prepared, which suggests a minor role of the dipole-dipole interaction in the overall balance of the structure-building forces. Varying this composition, work function of the gold substrate could be tuned linearly and in controlled fashion within a ~1.1 eV range, between the ultimate values for the single-component monolayers.

As the next task, I studied the applicability of the embedded dipole concept to the different substrates, taking Ag(111) as a representative example. The aromatic SAMs with the embedded pyrimidine group were found to be much more robust in this context as compared to the aliphatic ones (with the embedded ester group), which makes the former systems especially useful in context of the electrostatic interface engineering.

In view of these favorable properties, the next task was optimization of the aromatic SAMs with the embedded pyrimidine group. This was achieved by shortening the molecular backbone and excluding aliphatic building blocks. The resulting, optimized monolayers preserved all useful properties of their prototypes in context of dipole engineering but exhibited much better electrical transport properties, which allowed our partners to fabricate organic thin film transistors with high performance and extremely low contact resistance.

Another promising tool for tuning the dipole attributes and the respective work function was found to be electron irradiation. This was demonstrated by the example of aromatic SAMs with the embedded pyrimidine group and terminal pyridine group. The observed behavior is presumably related to specific chemical transformations involving the nitrogen atom in these moieties. It leads to several practical implications, including work function lithography, which could be demonstrated by representative patterns.

Alternatively, to the embedding of a dipolar group, the selection of a specific anchoring motif was tried in context of interfacial dipole engineering, taking dithiocarbamate-based SAMs as a representative example. The combination of the spectroscopic and work function data with the results of theoretical simulations performed by our partners allowed understanding the

structure and electrostatic properties of these monolayers in very detail, paving the way for their applications.

Table of Contents

1. Introduction

The performance of organic electronics and photovoltaics devices relies to a large extent on the energy level alignment between the adjacent electrode, buffer and active layers. This can be achieved by selection of suitable materials, tuning of their properties (e.g. by exact chemical composition, doping or morphology) but also by introduction of intermediate monomolecular films - self-assembled monolayers (SAMs) - providing suitable electrostatic shift at the relevant interfaces.[1-14] Such films usually consist of three building blocks, viz. docking group, molecular backbone and terminal tail group, mediating bonding to a particular substrate, promoting efficient molecular assembly, and defining specific physicochemical identity of the SAM-ambient interface, respectively.[15-17] Adjustment of the electrostatic shift provided by a particular SAM is usually achieved by selection of a suitable dipolar tail group which either increases ($-CF_3$, $-C_6F_5$ or $-CN$) or decreases ($-CH_3$ or $-NH_2$) the work function of the substrate.[2,3,5,6,8,11] This approach has, however, several drawbacks, viz. possible influence of the selected tail group on the morphology of the adjacent layer (e.g. organic semiconductor) and, vice versa, possible reorientation or even chemical modification of this group induced by the adjacent layer, which can distort the desired energy level alignment. The modification of the docking group can potentially lead to good results as well, but is less frequently used.[18]

Alternative strategies, suggested recently, involve the use of a dipolar molecular backbone or embedding of a dipolar group into the backbone, decoupling thus, completely or at least to a significant extent, dipole engineering and interfacial chemistry and protecting the dipolar group from possible modification or reorientation upon deposition of a buffer or organic semiconductor layer during the assembly of an organic solar cell or an organic transistor.[18-22] In particular, the concept of embedded dipoles was successfully demonstrated for both aliphatic and aromatic SAMs, using the dipolar ester and pyrimidine mid-chain groups, respectively.[19,22] These groups were introduced in two opposite orientations with respect to the backbone, with the dipole moment directed either from or to the substrate, resulting in a work function difference of 1-1.1 eV.[19,22] By the example of the aromatic SAMs with pyrimidine mid-chain groups, it was also demonstrated that the molecules with the differently oriented, embedded dipolar groups can be combined together as a mixed SAM. By varying the portions of both components, the work function could then be flexibly varied between the ultimate values corresponding to the one-component SAMs with a certain orientation of the mid-chain dipolar group. Interestingly, this variation did not occur as a linear but as an S-shape curve as a function of the composition of both components in the primary mixed solutions. This was explained by a different composition of the films on the surface compared to the situation in solution with a 50:50 mixture being energetically favorable because of the stabilizing head-to-tail arrangement of the neighboring dipoles,[18] that is, because of the active participation of the dipole−dipole interaction in the balance of the SAM building forces.

The above state of research was the starting point of my work, which major goal was an extension and optimization of the embedding dipole approach, along with several other concepts in general context of interfacial dipole engineering. The work was performed within several collaboration projects, with a variety of partners with complementary expertise (synthesis, theory, device fabrication, etc.) from Germany and abroad; they will be specifically mentioned in the respective chapters. My part within these joint projects was (i) development of new concepts in the field of interfacial dipole engineering (together with all the partners), (ii) preparation of the samples and their characterization by a variety of different experimental

techniques used in our group, (iii) characterization of the electrostatic and electrical transport properties of the samples, and (iv) analysis and implementation of the results (together with all the partners).

At first, relying on the already mentioned concept of the mixed self-assembled monolayers, I applied it to the aliphatic SAMs films with a dipolar ester group embedded into the alkyl backbone.[22-25] The selected precursors, $SH(CH_2)_{10}COO(CH_2)_9CH_3$ and $SH(CH_2)_{10}OOC(CH_2)_9CH_3$, abbreviated as C10EC10-up and C10EC10-down, respectively (aliphatic SAMS, Figure 1.1), form well-defined single-component SAMs on gold with the work function differing by ~1.1 eV,[22] providing, thus, an ideal platform for studying their mixture in context of electrostatic interfacial engineering. The particular questions were the (i) structure of the mixed SAMs, (ii) relation between the solution and in-SAM compositions of both constituents, (iii) tunability and exact behavior of the work function upon the variation of the SAM composition, and (iv) morphology of the mixed monolayers. The results of this subproject are described in Chapter 4.1.

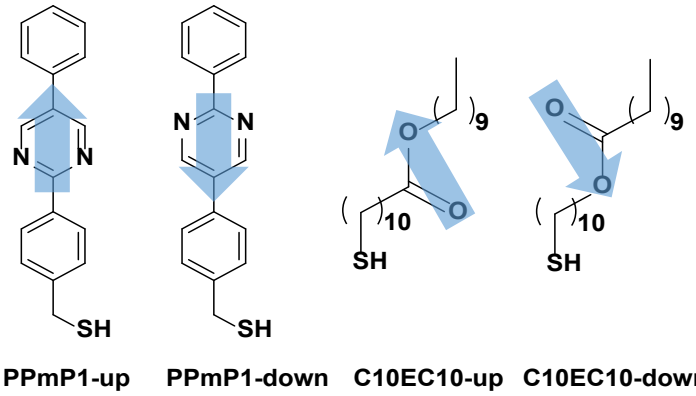

PPmP1-up **PPmP1-down** **C10EC10-up** **C10EC10-down**

Figure 1.1. Structures of the aromatic and aliphatic SAM precursors used in this thesis, along with their acronyms. For the aromatic SAMs, Pm, P, and "1" mean pyrimidine, phenyl, and number of the methylene groups in the aliphatic linker, respectively. For the aliphatic SAMs, C_n refers to the number of the methylene and methyl moieties in the segments above ("top") and below ("bottom") of the ester (E) group. The directions of the dipole moments of the embedded dipolar pyrimidine and ester groups with respect to the molecular backbone (upright molecular orientation with the thiolate anchor to the substrate) are marked by blue arrows. They are included as "up" and "down" in the acronyms.

The next step in my work was to test to what extent the concept of embedded dipole, working excellently in the case of Au, is applicable to an alternative support, taking Ag(111) as a representative example, following the approach of ref [26]. Along these lines, I studied both aliphatic and aromatic SAMs (Figure 1.1) with the suitable embedded dipolar groups (ester and pyrimidine, respectively) directed electrostatically either to or from the substrate as well as mixed monolayers comprising the molecules with the opposite orientations of the embedded dipoles. Additional goals of this part were to prove the validity of the electrostatic effects in photoemission for an arbitrary substrate and to test the correlation between these effects and work function. The choice of Ag(111) for this study was related to its general suitability for formation of thiolate SAMs but distinctly different properties in terms of molecular self-assembly compared to Au(111),[14,17,23,27] which potentially allows to achieve different adsorption geometries and, consequently, different electrostatic properties of the monolayers. The results of this subproject are described in Chapter 4.2.

The results of the experiments for Ag(111) suggested that aromatic SAMs with the embedded pyrimidine group are more robust in terms of electrostatic interface engineering as compared to the aliphatic ones. In view of these favorable properties, the next task was optimization of the aromatic SAMs with the embedded pyrimidine group. The initial design of these monolayers disregarded an important aspect, viz. their electrical resistance, which can also affect the efficiency of the charge injection at the electrode-SAM-organic semiconductor interface. This design included a long aromatic backbone (three rings) and a methylene linker connecting this backbone to the thiolate docking group (see Figure 1.1).[19] A long backbone means a lower conductance, with an exponential dependence on the length,[28-31] while the introduction of the methylene linker decouples to some extent the electronic subsystems of the metal substrate and conjugated segment,[32-34] resulting in a further decrease of the conductance. Thus, for application in organic electronics, this structural element, which typically helps to improve the molecular packing and lateral order in the SAMs,[35-37] needed to be avoided. With all the aforementioned considerations in mind, a new set of SAMs, based on the pure aromatic precursors with two rings in the molecular backbone (PmP-up and PPm-down, Figure 1.2), was designed and investigated. As a polar element, we used again the pyrimidine ring ("Pm"), which was built into a biaryl system in two different orientations, combining it with the phenyl ring (P). Along with the optimization of the SAM preparation procedure, I studied in very detail the basic parameters and properties of the respective monolayers, crucially important in context of their applications. A particular attention was paid to their electrostatic and electrical transport properties in context of their applications. The results of this subproject are described in Chapter 4.3.

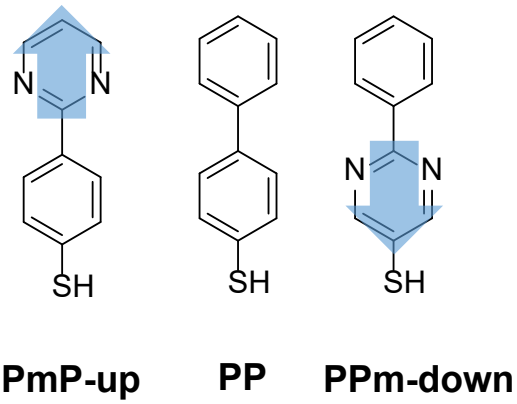

Figure 1.2: Structures of the optimized aromatic SAM precursors used in this project. The directions of the dipole moments of the embedded dipolar groups are marked by blue arrows. They are included as "up" and "down" in the acronyms. PP is considered as the reference system.

Along with the optimization of the pyrimidine-substituted SAMs, I studied their modification by electron irradiation, in context of interfacial dipole engineering. It is generally known that along with the flexibility of chemical design, additional possibilities are provided by modification of SAMs by physical means, such as ultraviolet light and electron irradiation. The respective options include, among others, preparation of sophisticated mixed SAMs,[38,39] SAM metallization,[40,41] SAM-based lithography and derived nanofabrication,[42-53] and fabrication of SAM-based carbon nanomembranes (CNMs).[54-60] In context of lithography and CNM fabrication, aromatic SAMs are of particular importance. In contrast to aliphatic monolayers, which become mostly disintegrated upon electron irradiation,[61] the reaction of aromatic SAMs to this treatment is dominated by extensive cross-linking, following the cleavage of C−H bonds

in the SAM matrix.[42,61-64] Such a cross-linking transforms the molecular assembly into a stable and homogeneous 2D film, preventing, at the same time, desorption of molecular fragments and complete damage of the SAM−substrate interface. Accordingly, aromatic SAMs can potentially serve as a negative resist for electron lithography[42,44,61] and, after a separation from the substrate, represent CNMs,[54−60] which can also be transformed into graphene-like sheets by subsequent pyrolysis.[59,60,65]

As a preliminary sub-project, performed in collaboration with my colleague, Dr. Can Yildirim, I studied modification of the pyridine-substituted SAMs by electron irradiation, finding that heteroaromatic SAMs exhibit behavior similar to that of homoaromatic monolayers, viz. a progressive and extensive cross-linking, preventing release of individual molecules and their fragments and slowing down and hindering the damage of the SAM/substrate interface. On this basis, I studied the modification of pyrimidine-substituted SAMs by electron irradiation, paying a particular attention to the work function behavior. As test systems, I took initially the most robust films, viz. a non-substituted aromatic SAM (terphenyl-4-methanethiol; TP1 (PPP1))[36,37,66-68] as well as TP1-derived monolayers with the terminal pyridine group (PyPP1)[69] and embedded pyrimidine groups (PPmP1-up and PPmP1-down, Figure 1.1)[19,20]. Note that the TP1 monolayers have already been studied with respect to their response to electron irradiation,[70] but not in context of work function modification. Within the further experiments, I also studied the optimal pyrimidine-substituted SAMs with a shorter, pure aromatic backbone, viz. PmPm-up and PmPm-down. In this part the particular questions were the (i) influence of the pyrimidine moieties on the irradiation process, (ii) stability and morphology of the irradiated monolayers and, (iii) tunability and exact behavior of the work function upon the irradiation of the SAMs. The result of this subproject are described in Chapter 4.4.

As an alternative to the embedded dipole approach, I also addressed the issue of interfacial dipole engineering by selection of a specific docking group. Generally, the docking group is predominantly chosen based on the affinity to a particular substrate serving as an electrode or, in context of organic photovoltaics, also as a buffer layer. Examples of docking groups comprise, in particular, phosphonic acids for zinc oxide surfaces[10,71] (a popular interfacial layer material in organic electronics devices), phosphonic acids and triethoxy- or trichlorsilanes for indium tin oxide.[9,71,72] Recently, as an alternative to thiolate and selenolate, dithiocarbamate (DTC) anchor group[12,73-77] has also been suggested as a basis for the functionalization of gold nanoparticles, for molecular electronics, and as anchoring group for dipolar SAMs in organic electronics.[78,79] In combination with either piperazine or piperidine as an intermediate linker, this group provides a versatile and robust platform for the attachment of different spacer moieties, as well as tail groups (Figure 1.3). In particular, the piperidine/piperazine linker, forming the link between the DTC group and the aromatic substituents, ensures the rod-like symmetry of the molecular backbone,[32,34] thus allowing a perpendicular orientation of the molecular axis relative to the substrate (a feature which was not available in the earlier aromatic DTC derivatives).[73,76,81] This allows the realization of a new type of monolayers which provide work functions of SAM-covered Au electrodes between 4.8 eV and 3.2 eV.[78] Although the performance of DTC-docked systems in polymer junctions has been demonstrated and a first spectroscopic characterization of the films along with molecule-based calculations has been provided,[78] the precise structure and molecular orientation of DTC-based SAMs was still largely unexplored. In addition, a deeper understanding of the electronic properties of such SAMs was of fundamental interest in view of the largely unexplored potential of the used unconventional docking group. Of particular relevance in this context was the question which of the contained functional blocks is actually responsible for the shift in the electronic landscape

that gives rise to the comparably large work function changes. Consequently, I tried to address the above questions within this particular subproject. The primary focus in this part of my work was put on the two very basic systems, namely, phenyl-piperidine-DTC (PPd) and phenyl-piperazine-DTC (PPz) SAMs on Au(111). These monolayers represent highly suitable model systems, which were specifically designed to address the distinct properties of the piperidine-DTC and piperazine-DTC docking platforms. The terminal phenyl ring of both molecules is a non-polar and well-defined structural unit supporting the formation of ordered SAMs. In addition, few other DTC derivatives were investigated which were derived from these two basic systems by a simple substitution of the phenyl ring in the para position or by its fluorination. The result of this subproject are described in Chapter 4.5.

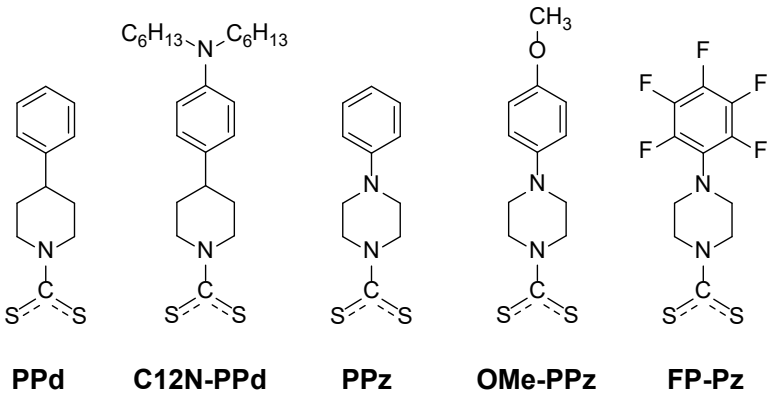

Figure 1.3: Schematic structures of the DTC-based SAM constituents used in this study along with the respective abbreviations.[30]

The basic information about SAMs is provided in the next chapter, along with background information about the characterization techniques used in this thesis. The experimental details regarding the sample preparation and characterization used in this work are given in Chapter 3. In Chapter 4, the results of the spectroscopic, electrical transport, and work function experiments are presented and discussed in detail. The conclusions of the PhD work are compiled in Chapter 5, and, finally, the most important supplementary data of our partners are presented in the Appendix.

Most of the results presented in this thesis have already been published or are in the final stage of preparation to be published. In each section the respective publications will be cited. In addition, all publications are listed in the Appendix. The publications have been prepared in cooperation with our partners and their contributions are specifically described as those in the text and in the captions of the corresponding figures, as far as these data are necessary for the general understanding of the issues discussed in the given thesis.

2. Basics and Background

2.1. Self-Assembled Monolayers

Self-assembled monolayers (SAMs) are monomolecular films, which are formed by the adsorption of organic molecules onto a suitable substrate. Most commonly used substrates are a variety of different metal, metal-oxides and noble-metal surfaces. One of the most extensively studied SAM systems are thiolates on noble-metal substrates like gold,[27,82-89] silver,[27,90,91] copper,[27] palladium,[92,93] platinum,[94] and mercury.[95] One of the more favored surfaces is gold as a substrate, due to its many advantages. Thin gold layers, varying from a few nanometers up to several hundreds of nanometers can be easily prepared by physical vapor deposition (PVD) and any weak or strong bound contamination can be easily removed by exposition of the surfaces to ultraviolet (UV) light. Due to its inertness, it will not form any oxide layers even if it is treated under ambient conditions. Silver in contrast will oxidize under these conditions and needs to be treated under inert gas conditions. Using thiols in combinations with these metal surfaces has the benefit of a high binding energy which will displace nearly all possible adsorbed impurities or unwanted molecules from the surface. SAMs consist of three major parts, the anchor (head) group, the backbone (molecular chain) and the tail group (functional group) (see Figure 2.1).

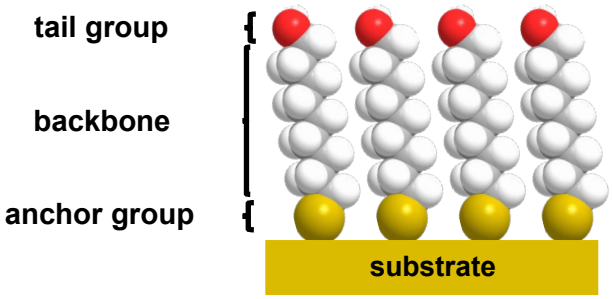

Figure 2.1: Ideally ordered self-assembled monolayer. SAM components are described on the left side. Drawn with ChemDraw.[96]

The anchor group binds the molecule covalently to the substrate and is connected to the backbone. Most SAMs consist largely of carbon atoms and can be described from two major motives, generally consisting out of an aliphatic or aromatic backbone. The backbone is used to define the film thickness and will protect the substrate surface from external influences if a well-defined and dense monolayer is build. The most common thickness of a SAM lies in the range of 1-3 nm, but is strongly dependent on the length and the tilt-angle of the adsorbed molecules. On top of the SAM lies the tail group which determines most of the chemical and physical properties of the formed SAM.

The process of SAM formation can be described by the model shown in Figure 2.2. The SAM formation is separated into five major steps. At the first step several molecules will be physisorbed in a lying arrangement at the surfaces. These molecules can be seen as a “lattice-gas” on the surface (A). Afterwards isolated, ordered islands are build, which are in equilibrium with the lattice-gas (B). The island growth will stop at the point where the whole surface is covered with the molecules (C). Up to this point, almost all molecules will lie flat on the surface

in a “lying-down” arrangement. Now, mostly by lateral pressure, to be able to adsorb more molecules some will change their orientation into a “standing-up” arrangement (D). This will lead to “standing-up” islands in a predominant “lying-down” arrangement until a 100% “standing-up” arrangement is achieved which is energetically favored (E).[82]

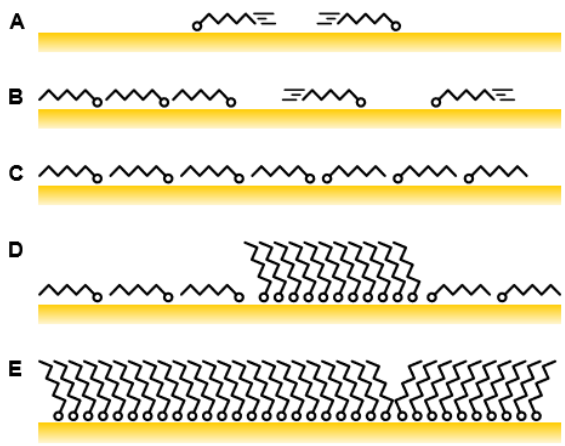

Figure 2.2: Schematic picture of the SAM-building process: physisorption (A), lying-down Islands (B), full-coverage with lying down (C), raising (D), full coverage in standing-up modification (E). Adapted from ref 82**.**

The sulfur is covalently bound to the gold as a thiol. Following Wood's notation, alkanethiol SAMs on Au(111) form a $(\sqrt{3}\times\sqrt{3})R30°$ monolayer with a c(4×2) superlattice. The spacing between the sulfur atoms is 4.97 Å and the calculated area per molecule is around 0.214 nm^2.[15] In most cases, preparation and storage of SAMs does not require ultrahigh vacuum (UHV) or other specialized conditions. Which results in an easy to prepare and investigate material in the area nanoscience and nanotechnology. They will form on various surfaces of different size or shape and the individual characteristic structure affects the interfacial behavior. Different effects of these monolayers can induce changes of the surface properties in terms of wetting, adhesion or friction and optical or electronic coupling. All these various possibilities makes them an interesting and multi-functional tool for thin films and most importantly in organic electronics.

2.2. X-ray Photoelectron Spectroscopy

2.2.1. Basic Information

Photoelectron spectroscopy is a common tool in surface science to get a quantitative and qualitative understanding of the top most layer (~10 nm) of a surface.[97-99] A variation of different energies can be used to excite differently bound electrons in the surface. In this context, two main techniques can be distinguished: (i) ultraviolet photoelectron spectroscopy (UPS), using excitation energies of $h\nu$ ~10 eV up to 100 eV and (ii) X-ray photoelectron spectroscopy (XPS), using excitation energies of $h\nu$ ~100 eV up to 1500 eV respectively. While UPS can only give certain information about the electrons in the valence bond (density of states (DOS) and electronic structure), due to its lower excitation energy, XPS can also probe the core electrons. For this reason, XPS is a popular investigation method due to its sensitivity and

selectivity (element of interest >0.05 atomic %). Almost all known elements can be detected with XPS, if they are not more than 10 nm deep into the investigated surface. The only exceptions are H and He, due to their low photoelectron cross sections. The kinetic energy (E_{kin}) of photoelectrons, emitted upon, is characteristic for each chemical element, with their own specific chemical environment.

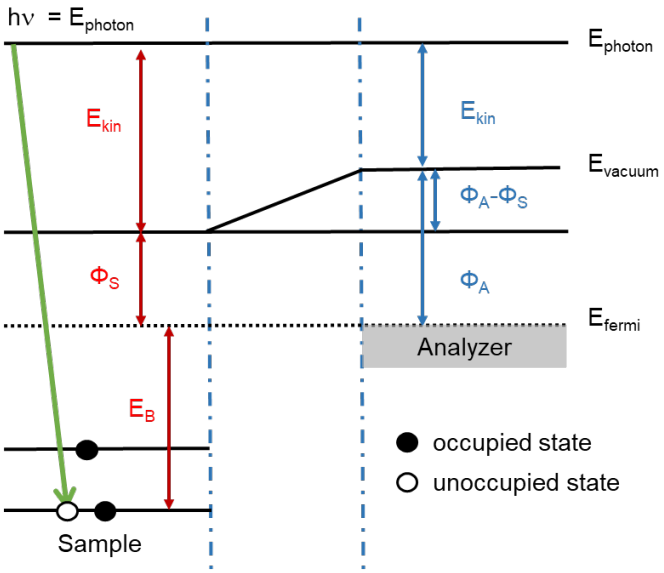

Figure 2.3: Energy levels in XPS.[61]

If the investigated sample is conducting and connected to the analyzer, their Fermi levels (E_F) will equalize and the kinetic energy of the electrons measured by the analyzer can be given by the following equation:[97,98]

$$E_{kin} = h\nu - E_B - \Phi_A \quad \textbf{(2.1)}$$

Where hν is the excitation energy of the photon source. The most commonly used photon source is a magnesium cathode with an excitation energy of 1253.6 eV. The binding energy (E_B) is the energy of the excited electrons according to the E_F, and Φ_A is the work function of the instrument, not the work function of the sample (Φ_S). The most relevant energies for XPS are shown in Figure 2.3. The analyzer work function Φ_A can also be determined with a metallic reference sample, who's E_B was set to zero (Ag or Ni for example). After energy calibration, Φ_A becomes zero and E_B and E_{kin} are directly related through the following equation:[98]

$$E_{kin} = h\nu - E_B \quad \textbf{(2.2)}$$

2.2.2. Spectrometer

A simplified XPS setup is shown in Figure 2.4, which consists most importantly out of three major parts: (i) the X-ray source, (ii) the energy analyzer and (iii) the detector. Most of the conventional and laboratory XPS setups use a X-ray source equipped with either Mg-anodes or Al-anodes, with their characteristic photon energies of MgK_α (hν = 1253.6 eV) and AlK_α (hν = 1486.6 eV). One of the most important parts is the energy analyzer, which determines E_{kin} of the photoelectrons, here shown as a spherical analyzer. The electrons are going into

the analyzer through a small slit and are circularly directed with the help of lens system through the hemisphere according to their E_{kin}. Only electrons with a pre-defined energy will reach the exit slit and are detected. The main task of the detector is to count the electrons according to their energy and intensity (in counts per second).[98]

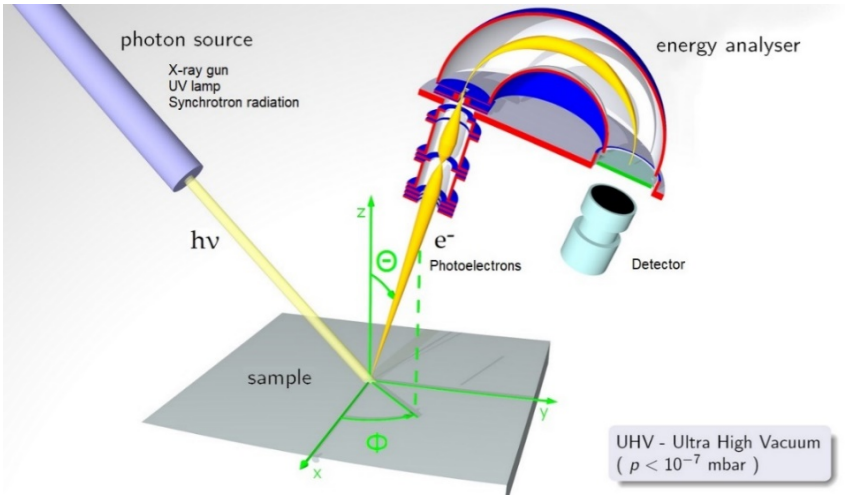

Figure 2.4: Scheme of a hemispherical XPS setup. The photons from the source produce photoelectrons, which are directed through a lens system to the analyzer. Electrons with a specific energy can pass the analyzer and are measured by the detector.[100]

2.2.3. Photoelectron spectra

The counted electrons will result in a spectra measured in counts per second (intensity) versus the given E_B. Figure 2.5 shows an overview spectrum of an exemplary hexadecanethiol (HDT, C16) SAM on Au, exhibiting the characteristic Au 4f, C 1s and S 2p (not visible at this magnification) resonances.

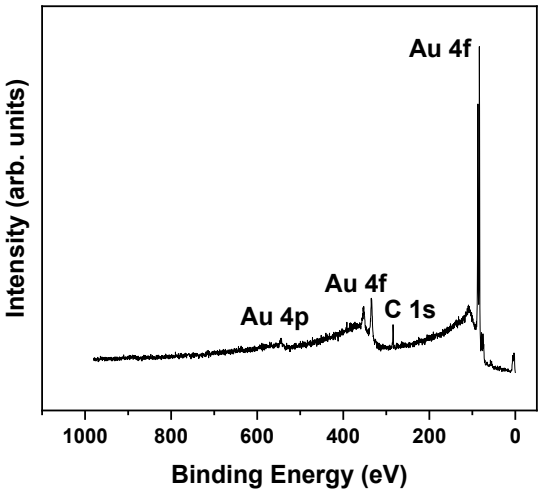

Figure 2.5: XPS overview spectrum of a hexadecanethiol SAM on Au(111) recorded with the MAX200 XPS-setup using its MgK_α X-Ray source.

The Au $4f_{7/2}$ peak is used as reference and shifted to 84 eV. All s-orbitals are visible as singlets and peaks of p, d and f levels are visible as doublets with their respective energy and splitting. XPS spectra can also contain Auger electron peaks beside the photoelectron peaks resulting from core level and valence band electrons.

2.2.4. Chemical Shift

The peak position during XPS measurements are strongly affected by the chemical environment (oxidation state, change of substituents, hybridization), it affects the energy of the emitted photoelectrons and is therefore visible in the spectral characteristics. This phenomenon is the so-called “chemical shift” and is one of the major interests in XPS utilization today. As an example, one can compare two different situation in which an atom bound two different neighboring atoms with low and high electronegativity. In the given case the charge transfer to the atom with higher electronegativity is more strongly and the partial charge of the second atom increases depending on the electronegativity of the neighboring atom. This increases also its E_B and at the same time decreases the E_B of the bound neighbor. Based on these observations and the resulting applications, in history XPS received also his second description: electron spectroscopy for chemical analysis (ESCA).

2.2.5. Quantitative Analysis

In addition to the qualitative analysis, possible with XPS, it is also suitable for detailed quantitative analysis like the stoichiometric composition or the thickness of the investigated film on top of the surface. In both cases, the intensity of the respective XPS signals are needed. To calculate the area of the resonances, a simple background has to be subtracted. It is possible to either subtract a linear, Tougaard or Shirly-type background (most commonly used).[98,101,102] After the background subtraction, the area of the peaks is calculated using a mixed Gaussian-Lorentzian or Voigt function to recreate the shape of the respective orbitals.[61] Also the model of the inelastic mean free path (IMFP) has to be introduced. It is described as the distance a moving electron can travel between collisions, which will have influence on the electron energy or direction. According to the universal curve by Seah and Dench,[61] the IMFP of electrons in solids is in the range of 1 nm to 3 nm for energies relevant in XPS. This IMFP is the so called “attenuation length” (λ) of electrons and adds a correction term that considers some elastic scattering effects as well. The attenuation length is an experimental value, which describes the distance where the intensity of a photoelectron has dropped to the value of e^{-1} while travelling through the material. This is also a main limiting factor for the analysis depth which is up to 3 λ. To calculate λ in alkanethiol SAMs on gold, the following equation can be used:

$$\lambda = kE^p \qquad \textbf{(2.3)}$$

Where k and p are empirical constants. With a radiation energy of the photon source in the range of 300 eV to 1000 eV, the constants in equation 2.3 are as follows:

$$\lambda = 0.3E^{0.64} \qquad \textbf{(2.4)}$$

A list of different attenuation lengths depending on their respective energies can be found in literature.[103] To calculate the molecular thickness of an organic SAM on a gold substrate, one needs to look at the relation between the intensities of the emission lines of the substrate before (I_{Au}^{o}) and after (I_{Au}) assembly of the molecular film, as the intensity should be weakened due to the damping effect of the film or any contamination on top of the substrate. To calculate the effective thickness equation 2.5 can be used:

$$\frac{I_{Au}}{I_{Au}^{0}} = \exp[-\frac{d_{SAM}}{\lambda \cos(\alpha)}] \quad \textbf{(2.5)}$$

with α as the angle between the analyzer and the surface. The intensity (I_{Au}^{o}) can also be obtained from a clean part of the substrate measured seperatly. An additional way to calculate the film thickness is to use a reference monolayer with well-defined and known thickness (for example HDT on Au(111) with a thickness (d_{ref}) of 1.89 nm, calculated from alkyl chain length, inclination and Au-S distance).[90,104,105] In this case, the signal of the substrate I_{Au} and the intensity of the carbon signal I_C of the sample are needed:

$$\frac{I_C}{I_{Au}} = k\frac{1-(exp\frac{d_{SAM}}{\lambda_C})}{\exp(\frac{d_{SAM}}{\lambda_{Au}})} \quad \textbf{(2.6)}$$

Rearrangement and calculation of the equations 2.5 or 2.6 will give the effective film thickness,[103] as well as the stoichiometric composition:

$$\frac{N_A}{N_B} = \frac{I_A}{I_B}\frac{\lambda_B}{\lambda_A}\frac{\sigma_A}{\sigma_B} \quad \textbf{(2.7)}$$

With the intensity of the XPS peaks (I_A to I_B), the attenuation length (λ) and the cross section (σ). With this analysis method, each sample can be characterized and described in detail.[97,98,,106]

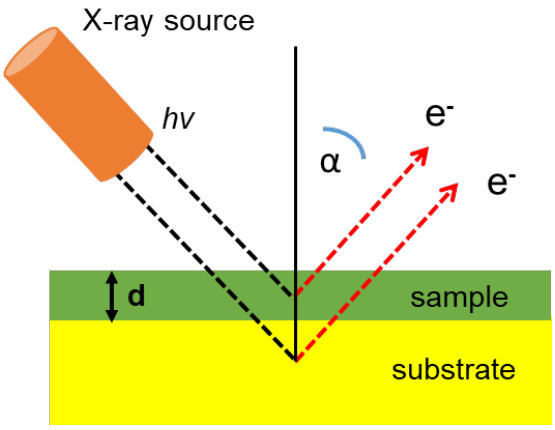

Figure 2.6: Schematic drawing of the geometry for film thickness (d) calculation.

2.3 Electron Irradiation of SAMs

When SAMs form on top of a surface, they will change the surface properties of the underlying substrate such as wettability, biocompatibility, (non-specific or specific) adsorption (of biomolecules), electronic structure and so forth.[17,104,107] Along with their ability to modify the properties of the surfaces they are formed on, the SAMs themselves can be modified by

irradiating them with electrons,[43,108-110] UV light,[111-114] and X-rays[115,116] as well. Among these modification tools, electron irradiation utilizes both primary and secondary electrons coming from the substrate to modify the monolayer. The electrons lead to changes in the hydrocarbon matrix and at the SAM-substrate interface. The character of the modification depends on the identity of the molecules forming the monolayer, most importantly on the molecular backbone. Monolayers consisting aliphatic molecules are strongly damaged under electron irradiation.[108,110,117,118] When aliphatic SAMs are exposed to electron irradiation, their response to the irradiation is a degradation of the SAM constituents, desorption of aliphatic fragments and weak cross-linking of the remaining aliphatic chains. This damaged film cannot protect the underlying substrate anymore against etchants; therefore, can be used as a positive e-beam resist (Figure 2.7).

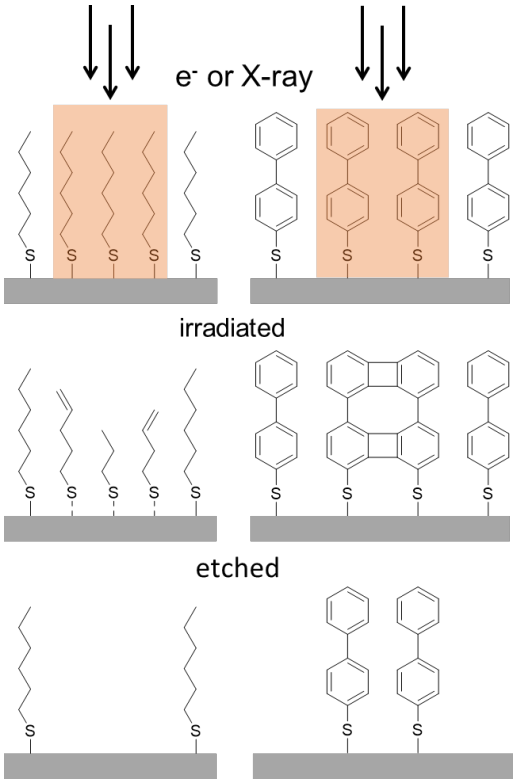

Figure 2.7: Schematic drawing of electron and X-ray lithography with aliphatic (a) and aromatic (b) SAMs as positive and negative resist materials, respectively.[119]

In contrast to the aliphatic SAMs, aromatic systems are not severely damaged but instead modified by electron irradiation. The adjacent aromatic chains in the SAMs are laterally cross-linked, which reduces the extent of damage to the monolayer such as desorption of the SAM constituents and results in formation of a 2D hydrocarbon film with chemical and mechanical resistance.[43,60] Note that cross-linking of aromatic SAMs with low-energy electrons (50-100 eV) are generally done by a dose of ~50 mC/cm^2 which roughly equals to 3000 electrons per nm^2.[60] Accordingly, aromatic SAMs behave as a negative e-beam resist (Figure 2.7). The simplest and most studied system for lithographic application is based on aromatic SAMs containing biphenyl units.[43,60] Even though the aromaticity of the monolayer seems to be the only prerequisite for cross-linking, a study[120] based on aliphatic but ring-shaped bicyclohexyl SAM has shown that not the aromaticity, but the ring structure is responsible for cross-linking. In that study, ring-shaped bicyclohexylthiol SAMs have also been laterally cross-linked under e-beam irradiation and have acted as a negative resist.[120]

In addition, when aromatic SAMs with nitrile[107] or nitro[44,121] tail groups are treated with electron irradiation, these terminal groups are converted (reduction) into amino groups which can be coupled over many chemical reactions, thus, aromatic SAMs can also be used as a template for surface functionalization and related fabrication of nanostructures.

Besides their abilities to be used as negative e-beam resist and to functionalize the surfaces, cross-linked aromatic SAMs form CNMs[54,57,59,60,122-127]] after removing their underlying substrate. The obtained CNMs can further be transformed into graphene-like sheets by annealing the CNMs at elevated temperatures.[59,123,124,126]

2.4 Synchrotron

Besides the already mentioned X-ray sources (Mg and Al), other light sources can also be used for XPS and other experimental techniques. One of the most popular ones, an efficient source of all different kinds of X-rays, is synchrotron irradiation. Any acceleration of charged particles will cause the emission of light. This general behavior is used by synchrotron accelerators, which accelerate charged particles following a circular trajectory by using magnetic fields. Every time the electrons pass through the strong magnetic field induced by banding magnets, the synchrotron radiation is emitted tangentially to the electron orbit and can be collected for further experiments at so-called beamlines. Since the energy of the radiation depends strongly on the E_{kin} of the electrons with help of electromagnetic elements, the photon energy can be tuned precisely to the desired values. The high resolution (0.1 eV or better) and the selectivity are a few of the major advantages of a synchrotron source. Contrary, samples, especially organic ones, could be destroyed even faster than with regular X-rays. This, as well as the cost and the availability is another important aspect and limitation of high resolution X-ray spectroscopy on synchrotron facilities.[60,61]

2.4.1 High Resolution X-Ray Photoelectron Spectroscopy

Synchrotron radiation has a number of certain properties, which make it advantageous for the XPS measurements if compared to the radiation obtained from the conventional laboratory source. First, the synchrotron radiation is much more intense. Indeed, to be at least somehow comparable to the synchrotron source the laboratory X-ray tubes have to operate on a very high wattage. The second asset of the synchrotron radiation is a variable excitation energy. The conventional laboratory source can usually provide the X-rays of a fixed excitation energy 1486.6 eV AlKα or 1253.4 eV MgKα depending on the anode type. If a synchrotron is used as a source of photon excitation, the excitation energy can be varied precisely in a broad range. This means that the surface sensitivity will be much higher than that of a conventional laboratory source. With a variable energy from the synchrotron, a non-destructive depth profile can be obtained as a function of electron kinetic energy. One can maximize the cross section of the given element by selecting an appropriate wavelength. By making a measurement using different excitation energies, one can easily eliminate the Auger lines avoiding the misinterpretation of the XPS data caused by overlapping of the Auger and XPS lines. At last, it is important that synchrotron is a clean radiation source and it will be hardly possible to contaminate the samples in UHV conditions.[128]

2.4.2 Near Edge X-ray Absorption Fine Structure Spectroscopy

Near-edge X-ray Absorption Fine Structure (NEXAFS) spectroscopy samples the electron structure of unoccupied molecular orbitals.

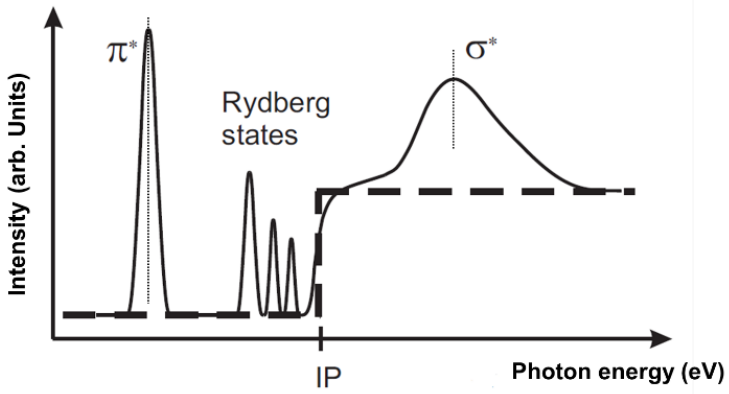

Figure 2.8: NEXAFS absorption spectrum. The thick dashed line corresponds to the photoabsorption cross section of an electron located in a single bound state (core level).[69,70]

Near edge X-ray absorption fine structure (NEXAFS) spectroscopy is a highly surface sensitive method to resolve the electronic structure and orientation of adsorbates (e.g. SAMs) on metal surfaces. NEXAFS is a synchrotron-based method and the best results can be achieved when probing light molecules such as carbon, nitrogen or oxygen using the soft X-ray region (100 eV to 700 eV). The X-ray adsorption edge describes the point, at which the energy of the X-ray photons is just enough to excite the electrons of a certain shell. Transitions from a deep core shell (mostly K shell) to unoccupied molecular orbitals are analyzed. NEXAFS spectra are usually recorded from just below the edge up to around 50 eV above. The step function (thick dashed line) in Figure 2.8 describes the simplest case of a core level electron in the absence of any other empty electronic state, when scanning the photon energy and passing the ionization threshold. Before the ionization potential (IP) no absorption takes place and after the IP the core electron is excited.

Figure 2.9a depicts a free single atom, which already has more final states than the simple model case mentioned above. Bound states (valence and Rydberg[129]), just below the IP, and unbound states (molecular antibonding), just above the IP. Figure 2.9b shows an energy scheme for a diatomic molecule with the according NEXAFS spectrum in Figure 2.8 (solid black line). Empty molecular orbitals are marked by an asterisk (σ* & π*).

The lowest unoccupied molecular orbital (LUMO) in a sp^3-C would be σ*, which results in a broad resonance (C1s→ σ*). The transition C1s→ π* or a π*-resonance is only observable in π-bonds, viz., double and triple bonds or in aromatic compounds. This transition shows a sharp resonance (Figure 2.8 π*). Transitions to the Rydberg orbitals, which are located between the π*-resonance and the IP, result in sharp but weak resonances.

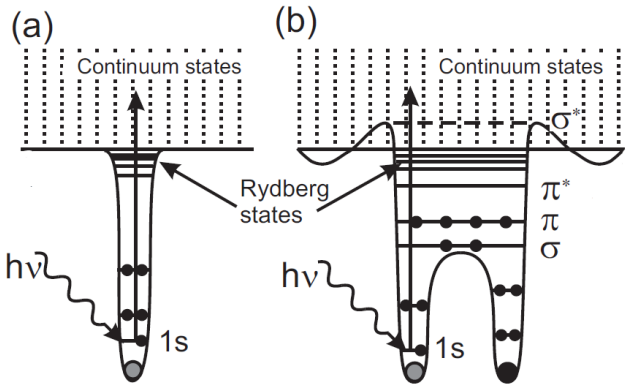

Figure 2.9: (a) Schematic potential for an atom and (b) schematic potential of a diatomic molecule. In addition to Rydberg states and a continuum of empty states similar to those expected for atoms, empty molecular orbitals are present, which are marked by an asterisk label (σ* & π*).[130,131]

Besides the resolution of the instrument, the lifetime of the excited state determines the peak broadening as well. Short lifetime results in sharp peaks. De-excitation can happen through Auger-transitions, fluorescence or falling back of the excited electron. As an easy rule, regarding the line shape of the spectrum, one can generally say that the higher a resonance lies in the continuum the larger is its linewidth. The NEXAFS spectroscopy takes the most information from π*-resonance, and thus is most suitable for the analysis of the according orbitals.[130,131]

2.4.3 Angular dependence & linear dichroism in X-ray absorption

As mentioned above, NEXAFS spectroscopy is a suitable technique to determine the molecular structure and the orientational order of a molecule, precisely the molecular orbitals, in relation to the surface normal of the substrate. The orientation can be determined by relating the incidence angle (θ) of the (linearly polarized) synchrotron light to the intensity of the respective orbital resonance (see Figure 2.10).

The quantum mechanical description, relating the photoabsorption cross section σ_x to the initial and final state, Ψ_i and Ψ_f, respectively, for a single electron is as follows:

$$\sigma_x \propto | < \psi_f | e \cdot p | \psi_i > |^2 \rho_f(E) \qquad \textbf{(2.8)}$$

With the unit electric field vector ***e*** and dipole transition operator *p* and $\rho_f(E)$ as the density of final states.[130,131] For linearly polarized light, the expression $< \Psi_f \mid p \mid \Psi_i >$ is known as transition dipole moment (TDM).

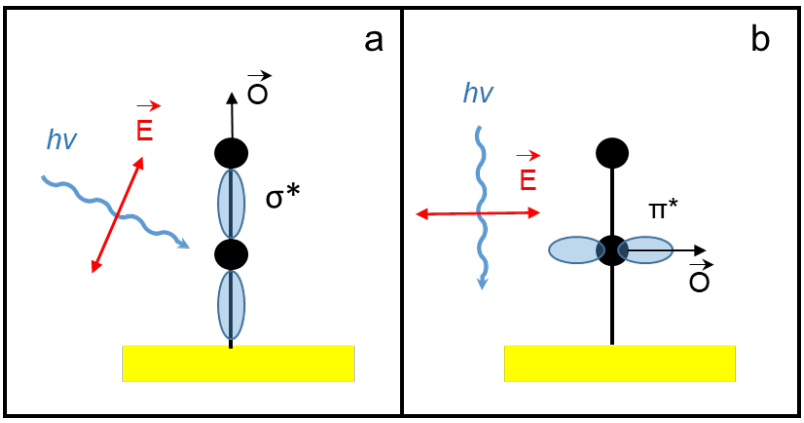

Figure 2.10: Overlapping of the electric field vector E and the direction of the final state orbital O overlap differently. (a) grazing incidence: σ* resonance it at maximum; (b) normal incidence: π* resonance is at maximum.[130]

The following equation describes the transition intensity for an initial state (1s) and a directional final state (matrix element $| e < \Psi_f | p | \Psi_{1s} >|^2$ points in the direction of the final state orbital O):

$$I \propto |e < \psi_f | p | \psi_{1s} > |^2 \propto |e \cdot O|^2 \propto cos^2 \delta \qquad \textbf{(2.9)}$$

with δ as the angle between the TDM direction and the electric field vector *E*. This relationship shows that the intensity is the largest, when the direction of the final state orbital O (or the direction of the TDM) and the direction of the electric field vector *E* are the same (see Figure 10). The π* resonance, as the most pronounced one, is suitable for the analysis of angular dependence. The simple equation to determine the molecular orientation relates the average intensities of the measurements of the resonance to the direction of the TDM (*α*), the incident angle (*θ*) and the polarization (*P*) of the synchrotron light:

$$I \propto P cos^2 \theta \left(cos^2 \alpha + \frac{1}{2p} tan^2 \theta \, sin^2 \alpha \right) \qquad \textbf{(2.10)}$$

From this relationship, the so-called *magic* angle of $\theta = arctan(\sqrt{2}P) = 55°$ with $P \approx 1$ can also be understood. At this incidence angle, the absorption intensity does not depend on the molecular orientation. This incidence angle is used to acquire orientation independent spectra or spectra of samples with unordered molecules. These NEXAFS spectra contain only information about the electronic structure of the surface film. For aromatic molecules, the TDM orientation (*α*) of the π* orbitals of the phenyl rings is directly related to the tilt angle (*β*) of the molecular backbone:[132]

$$cos(\alpha) = sin(\beta) \, cos(\gamma) \qquad \textbf{(2.11)}$$

For the twist angle *γ*, a typical value for aromatic systems would be 32°.[133] As mentioned above, at an incidence angle of 55° no orientational effects influence the spectrum. On the other hand, a difference of two spectra, acquired at 90° (normal incidence) and 20° (grazing incidence) results in a fingerprint spectrum of the molecular orientation, known as the linear dichroism. Taking into account that cos(90°) = 0 and cos(20°) ≈ 1:

$$I(90°) - I(20°) \propto \left(\frac{3}{2} sin^2(\alpha) - 1\right) \qquad \textbf{(2.12)}$$

When *α* is small (angle between the electric field vector *E* and the averaged TDM direction), it results in a negative spectrum and for $\alpha \geq 55°$ the spectrum is positive.[130] This difference spectrum shows the orientational order at first sight. For molecules with a π* resonance

(double or triple bonds in the molecular plane) a negative spectrum signifies a planar orientation and a positive spectrum an upright orientation. For the σ* resonances it is the other way round, as the two orbitals are perpendicular to each other.

2.5 Work Function Measurements

The Kelvin Probe (KP) is a non-contact, non-destructive device which can be used to measure the WF difference, or for non-metals, the surface potential, between a conducting sample and the vibrating tip.[134]

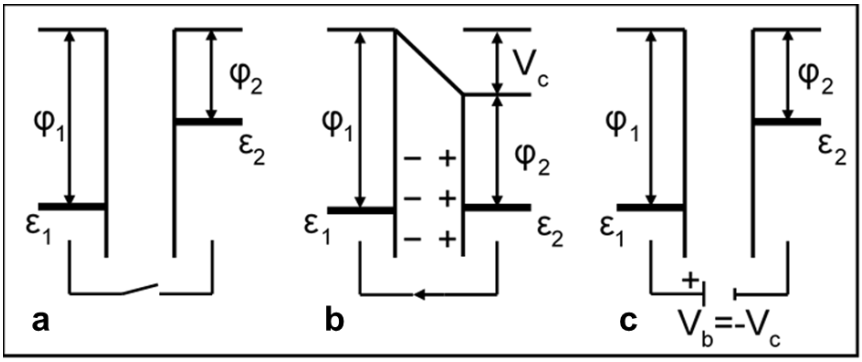

Figure 2.11: (a) The electron energy level diagram for two conducting but isolated samples. φ_1 and φ_2 represent the work functions of the materials, with $\varphi_1 > \varphi_2$. (b) If an external electrical contact is made between the two electrodes their potentials equalize and the resulting flow of charge (in direction indicated) produces a potential gradient, termed the contact potential V_c, between the plates. The two surfaces become equally and oppositely charged. (c) Inclusion of a variable "backing potential" V_b in the external circuit permits biasing of one electrode with respect to the other. At the unique point where $V_b = - V_c$ the (average) electric field between the plates vanishes, resulting in a null output signal.

The WF is the least amount of energy needed to remove an electron from the surface of a conducting material, to a point just outside the metal with zero kinetic energy. As the electron has to move through the surface region, it´s energy is highly influenced by the chemical, optical, electric and mechanical characteristics of this region. Hence, the WF is an extremely sensitive indicator of surface condition and is affected by adsorbed or evaporated layers, surface reconstruction, surface charging, oxide layer imperfections, surface and bulk contamination. The Kelvin Method is an indirect technique, i.e., electrons are not extracted directly from the surface, instead using a reference surface (vibrating tip) as the counter electrode the surface under study forms one plate of a parallel plate capacitator. Electrons flow back and forth in the external circuit as the tip vibrates. The WF difference is determined by the addition of an external voltage, termed the backing potential (V_b). The traditional Kelvin Probe method consists of a flat circular electrode (termed the reference electrode) suspended above and parallel to a stationary electrode (the studied sample), thus forming a simple capacitator, having the respective WF (φ_1, φ_2) and Fermi-levels (ε_1, ε_2).

Traditionally, the WF difference between two surfaces was determined by vibrating the reference surface above the sample adjusting V_b until a zero null output resulted. However,

this mode of detection is extremely sensitive to noise since the Kelvin Probe signal is diminishing with respect to the noise background. The noise background spectrum consists of several components: (i) overtalk from the power signal used to drive the tip vibration mechanism, termed the driver; background mains (or net) noise, and (ii) a contribution from other surfaces that are capacitively coupled with either the tip or the sample. To overcome this noise firstly off-null detection where the signal is measured at high signal levels far from balance is made, which greatly suppressed driver talk-over and lastly a special developed tracking system (Baikie Method) is used for substantially reducing the effects of the other surfaces that are in capacitive coupling with the tip/sample.[135]

2.6 Electrical Conductance Measurements

The measurement of the current-voltage (I-V) response for SAMs helps directly to understand their charge transfer properties. It is also the most direct and easiest way to measure the conductivity in SAMs.[87] The I-V characteristics of SAMs are measured by connecting a suitable non-destructive top electrode on top of the SAMs, where the metal substrate on which the SAM is formed then serves as the bottom electrode.

Table 2.1: Conduction mechanisms.[91]

Conduction mechanism	Characteristic behavior	Voltage dependence
Direct tunneling	$J \sim V exp(-\frac{2d}{\hbar}\sqrt{2m\Phi})$	$J \sim V$
Fowler-Nordheim Tunneling	$J \sim V^2 exp(-\frac{4d\sqrt{2m\Phi^3}}{3q\hbar V})$	$\ln(\frac{J}{V^2}) \sim \frac{1}{V}$
Thermioinic emission	$J \sim T^2 exp(-\frac{\Phi - q\sqrt{qV/4\pi\varepsilon d}}{kT})$	$ln(\frac{J}{T^2}) \sim \frac{1}{T}$
Hopping conduction	$J \sim V exp(-\frac{\Phi}{kT})$	$ln(\frac{J}{V}) \sim \frac{1}{T}$

I-V response of SAMs have been studied by different experimental tools such as molecular junctions based on scanning probe methods,[137-139] mercury drop,[28,140-142] and eutectic gallium-indium (EGaIn) tip.[143,144] With scanning probe methods, very small areas are analyzed, whereas with mercury drop and EGaIn tip bigger areas can be analyzed due to larger contact areas between the top electrode and the SAM.

It has been shown that there are two main conduction mechanisms dominating the electron transfer rates of SAM films: non-resonant (direct) tunneling[137,138,143,145] and hopping[136,146,147] Non-resonant tunneling is the most common transport mechanism observed in saturated alkyl SAMs,[148] with a high energy difference between the highest occupied molecular orbital (HOMO) and the lowest unoccupied molecular orbital (LUMO) around 8 eV[137] and an

exponential decrease in the tunneling rates with increasing molecular length. This exponential dependence is given by the equation 2.13:

$$J = J_0 \exp(-\beta d) \quad \textbf{(2.13)}$$

where β is tunneling decay parameter and d is the molecular length. This parameter is in particular useful to get information about the transport efficiency of SAM films.

However, in the case of conjugated film, HOMO-LUMO gaps are smaller; therefore, different transport mechanisms have to be considered. Resonant tunneling or hopping conduction could take place,[137] as well. Besides, upon increasing bias voltage a transition from direct tunneling to field emission (Fowler-Nordheim tunneling) can be observed.[137,138] The transition point, where the conduction mechanism changes, is believed to be fingerprint for the positions of frontier orbitals.[149,150] While the transition voltage appears at higher voltage range in saturated alkyl SAMs, it appears to be at smaller voltage range in aromatic SAMs.[138]

2.7 Contact Angle Goniometry

In contact angle goniometry, the angle between a drop of liquid and a surface at equilibrium (θ) is measured.[151] The shape of the drop is defined by the specific properties of the liquid (L), the surface (S) and the vapor (V) around the drop, as described in Figure 2.12. This can be described by the Young equation:

$$\gamma_{SL} + \gamma \cos\theta = \gamma_{SV} \quad \textbf{(2.14)}$$

Where γ_{SL} is the interfacial tension between the liquid and the solid, γ is the interfacial tension between the liquid and the vapour, γ_{SV} is the interfacial tension between the solid and the vapour and θ is the equilibrium contact angle the drop makes with the surface.[152]

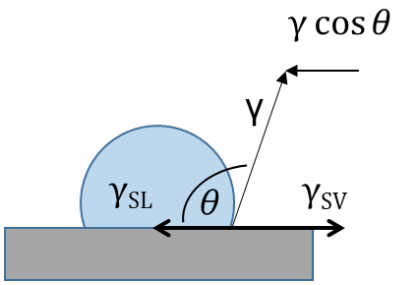

Figure 2.12: Schematic representation of a drop on a surface.

As shown in Figure 2.13, by either advancing or receding the drop on/from a surface, one can measure the advancing and receding contact angles, θ_{adv} and θ_{rec} respectively. The difference between these two values gives a measure of the surface homogeneity. In practice, θ_{adv} and θ_{rec} rarely have the same value and a small hysteresis is always observed.[153] The difference between these two angles is influenced by a variety of factors, e.g. surface roughness, molecular (re)orientation and interaction between the liquid and the solid.[151,152]

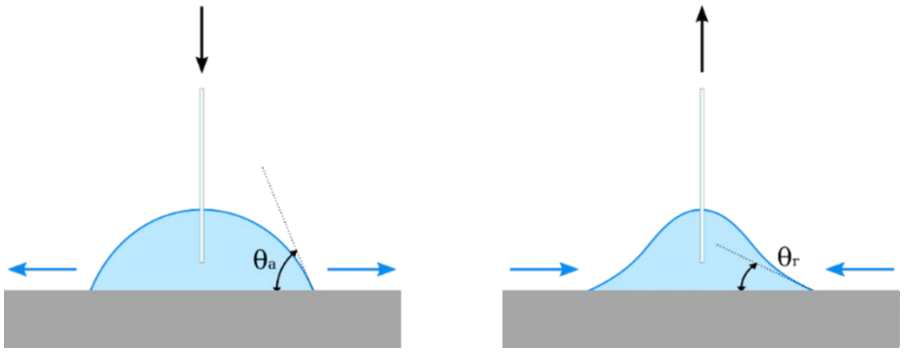

Figure 2.13: Schematic representation of the advancing and receding contact angles of a drop on a surface. (adapted from http://en.wikipedia.org)

2.8 AFM Measurements

Atomic force microscopy (AFM) is one of the most widely used scanning probe microscopy, which is able to measures several surface properties of the scanned area including topography, friction, magnetic and electric.[154-156] They can be operated at ambient atmosphere, in liquid or under vacuum,[154-156] and they are much easier to use compared to electron microscopes.

The schematic representation of an AFM is found in Figure 2.14. The sample is mounted on a stage, which can be moved by several piezo elements in x- and y- directions. The maximum scan area of AFM is roughly 100x100 μm^2 with a horizontal resolution of ~1 nm.[157,158] The tip can move only in z-direction. Traditionally, x and y piezo materials are used to move the sample stage and the AFM tip is moved by a separate z piezo material, however, there are also some companies, which mount all three piezomaterials (for x,y and z-direction) to the sample stage. The position of the tip is tracked with a laser, which is reflected at the backside of the tip. The reflected laser is collected by a photodiode, generating a current, and the current values over the scan area is then converted to an image of the respective area.

When the AFM tip approaches to the surface of interest, it behaves as in the force-distance curve given in Figure 2.15. At short distances, because of the overlapping orbitals of the electrons from surface and tip, repulsive forces occur, while at larger distances attractive forces occur because of the van der Waals interaction. The exerted force on the tip can be described by the Lennard-Jones potential (Figure 2.15), thus, leads to cantilever deflection. If the distance is beyond the interaction range, no force acts on the tip and the cantilever is not deflected.

AFM measurements can be operated in static (contact and force spectroscopy) or dynamic (semi-contact and non-contact) mode. In contact mode, the cantilever is swept over the surface of the sample and is deflected because of repulsive forces. In the contact mode, the topography of the sample can be obtained by two ways: constant height mode or constant force mode. While in the constant force mode movement of the z-piezo gives the topography of the surface under investigation, in the constant height mode deflection of the cantilever is converted to the topography of the surface. This mode is preferably used for hard surfaces and can also be used in liquid environment.

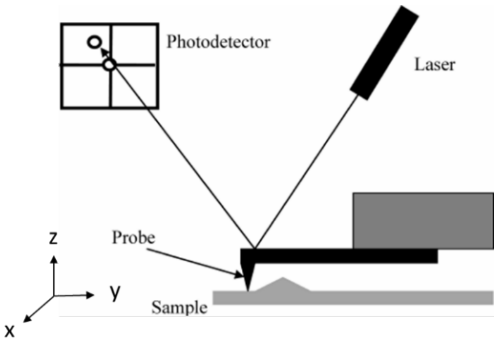

Figure 2.14: Schematic diagram of a general AFM setup: A laser beam is focused on the backside of a cantilever and reflected from it into a four-quadrant photodetector. A sample is mounted on a piezo tube that can move the sample in x, y and z directions.[159]

Nevertheless, the contact mode on soft samples like polymers or biomolecules could give damage to the sample. Therefore, a "softer" contact mode was developed, known as semi-contact (tapping mode or intermittent contact), in which the tip is kept at a distance from an attractive regime and the changes in frequency and amplitude are used to measure the force interaction. In tapping mode, the cantilever oscillates up and down near its resonant frequency using a small piezo element in the cantilever holder. Then the tip is approached to the sample until the amplitude has decreased to a predefined value because of the forces (van der Waals forces, dipole-dipole interactions, electrostatic forces) acting on the cantilever. This amplitude value is sent to the z-piezo element which controls the height of the cantilever above the sample.

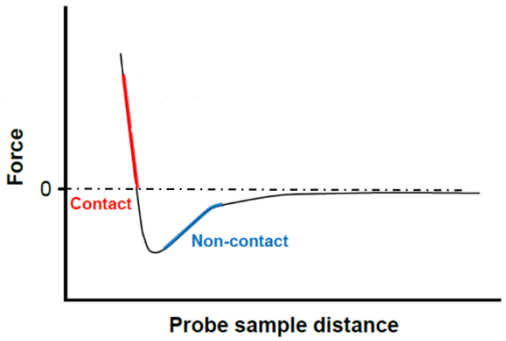

Figure 2.15: Sketch for a force-distance curve of AFM tip and sample. Different operation modes can be used under the effect of described regimes: contact, intermittent contact or non-contact.

The non-contact mode is similar to the tapping-mode, however, the tip is not affected by the sample during oscillation. Instead, the attractive forces of the sample exert a very weak force on the cantilever, resulting in a shift of the resonance frequency and thus amplitude.

3 Experimental

3.1 Materials & Preparation Procedures

In this chapter, the preparation methods of the monomolecular films are presented along with the experimental methods used to characterize their physical and chemical properties.

3.1.1 Substrates

Au and Ag substrates were purchased from Georg Albert PVD-Beschichtungen (Silz, Germany). They were prepared by thermal evaporation of 30 nm of the respective metal (gold and silver, 99.99% purity) onto polished single-crystal silicon (100) wafers (Silicon Sense) that had been pre-coated with a 9 nm Ti adhesion layer. Both films were polycrystalline, exposing preferably (111) orientated surfaces of individual crystallites.

For the DTC films, atomically flat template stripped gold (TSG) was employed and prepared according to reported procedures[80,81] and used as substrate. The Au films exhibited a root mean square (RMS) roughness of 0.3 nm, exposing preferably (111) oriented surfaces.

3.1.2 SAM-Precursors and Preparation

The SAM precursors were custom-synthesized by one of our partner groups, according to the literature recipes.[12,19,22,23,26] All other chemicals and solvents were purchased from Sigma Aldrich and used as received.

The single-component C10EC10-up/down as well as the reference alkanethiol (C16/C20) SAMs were formed by immersion of the substrates into 1 mM solutions of the SAM precursors in ethanol (EtOH) under nitrogen at ambient temperature for 24 h.

The single-component aromatic SAMs were prepared by immersion of the substrates into 0.5 mM solutions of the SAM precursors in tetrahydrofuran (THF) under nitrogen at ambient temperature for 24 h.

The mixed SAMs were prepared by co-adsorption of both precursors, “up”/”down”; with their relative portions in solution, either in EtOH or THF, being varied. After immersion, the samples were ultrasonicated and carefully rinsed with pure solvent and blown dry with a stream of Ar.

The DTC films were prepared under nitrogen by immersing the freshly stripped TSG substrates into DTC solutions for ~20 h at room temperature. After immersion, the films were copiously rinsed with EtOH, immediately blown dry with N_2 and placed in nitrogen filled glass containers for transport. All vials and tweezers were cleaned with piranha acid and isopropyl alcohol before usage.

The respective precursors can be found in Figure 3.1-3.3 for each type of monolayer.

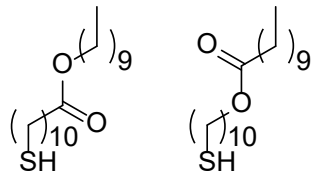

C10EC10-up C10EC10-down

Figure 3.1: Molecular structures of the C10EC10-up and C10EC10-down molecules with embedded ester group, along with their acronyms. The molecules were custom-synthesized by our partner group from the Université Laval, Quebec, Canada (Prof. J.-F. Morin and G. Charles-Olivier).

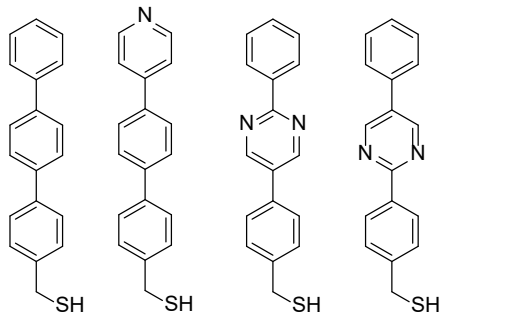

PPP1 PyPP1 PPmP1-down PPmP1-up

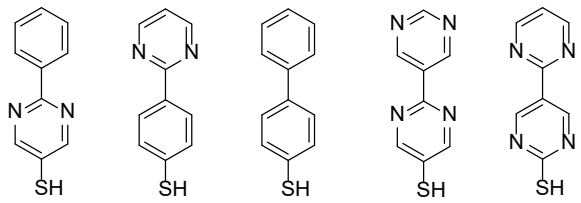

PPm-down PmP-up PP PmPm-down PmPm-up

Figure 3.2: Molecular structures of the PPP1, PyPP1, PPmP1-up/down, PP, PmP-up/PPm-down and PmPm-up/down molecules with embedded/distributed pyrimidine group/groups, along with their assigned acronyms. The molecules were custom-synthesized by our partner group from the Frankfurt University (Prof. A. Terfort and M. Gärtner).

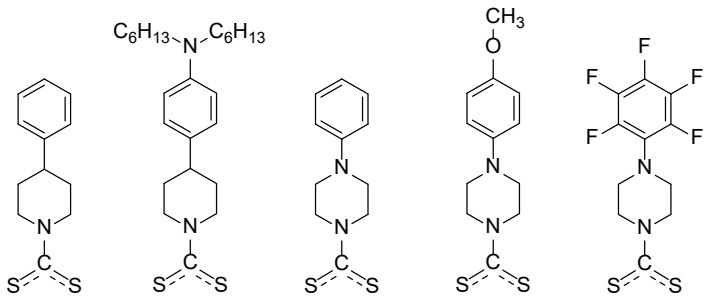

PPd C12N-PPd PPz OMe-PPz FP-Pz

Figure 3.3: Molecular structures of the DTC-based molecules, along with their assigned acronyms. The molecules were custom-synthesized by our partner groups from the Stuttgart University (Prof. S. Ludwigs and D. Treftz) and Sony Deutschland GmBH, Stuttgart (Dr. F. von Wrochem).

3.2 Electron Irradiation and Lithography

All irradiation experiments were performed at room temperature. The electron irradiation was carried out homogeneously over the entire sample area. A flood gun (FG20, Specs, Germany) was used. The energy of electrons was set to 50 eV. The flux was calibrated by a Faraday cup. A base pressure during the irradiation was lower than 1×10^{-8} mbar. Along with the homogeneous electron irradiation, WF patterns were fabricated by proximity printing lithography. These patterns were written by homogeneous electron irradiation through a mask (Quantifoil, R 1/4, Plano, representing holey (1 µm) carbon film over Cu 400 mesh) placed on the SAM surface. The same setup as for the homogeneous irradiation was used. The fabricated WF patterns as well as respective morphology patterns were imaged by a Solver Next microscope (NTMDT). The AFM measurements were carried out under ambient conditions, either in the surface potential or tapping mode, respectively.

3.3 Characterization & Analysis

In this section, all used experimental setups and techniques along with the selected parameters are introduced. The analysis, processing of the data and the used calculation methods are also described.

3.3.1 XPS & HRXPS

XPS measurements were performed at two different locations. The laboratory XPS measurements were carried out with a MAX200 (Leybold-Heraeus) spectrometer equipped with a MgK_α X-ray source (200 W) and a hemispherical analyzer. Normal emission geometry was used. The recorded spectra were corrected for the spectrometer transmission.

The synchrotron-based High Resolution X-Ray Photoelectron Spectroscopy (HRXPS) measurements were performed at the HE-SGM beamline (bending magnet) of the synchrotron storage ring BESSY II in Berlin, Germany, using a custom-made experimental station equipped with a Scienta R3000 electron energy analyzer.[130] The synchrotron light served as the primary X-ray source. The spectra acquisition was carried out in normal emission geometry with an energy resolution of ~0.3 eV at an excitation energy of 350 eV and somewhat lower resolution at higher excitation energies.

Spectra were recorded in the Au 4f, C 1s, S 2p, N 1s, O 1s and F 1s regions, depending on the sampled substrates. The photon energy ranged from 350 eV over 580 eV to 750 eV. For all recorded spectra, the binding energy (BE) was referred to the Au $4f_{7/2}$ emission at 84 eV, measured at the same pass energy (PE).[160] To process the data, the software XPS Peak 4.1[161] was used. A Shirley-type background[101] was subtracted and the spectra were fitted by symmetric Voigt functions. To fit the S $2p_{3/2;1/2}$ doublets, a pair of such peaks with the same full width at half-maximum (FWHM) values, branching ratios of 2 (S $2p_{3/2;1/2}$), and spin-orbit splitting of ~1.2 eV (S $2p_{3/2;1/2,}$ verified by fit), were used.[160] The fits were performed self-consistently: the same fit parameters were used for identical spectral regions.

Using the data from this evaluation, the effective thickness and packing density of the sample monolayers were calculated. Well-defined monolayer on Au (111) with known thickness, namely hexadecanethiol (C16), eicosanethiol (C20), terphenyl-4-methanethiol (PPP1) and biphenylthiole (PP) served as references for the calculations. The thickness was determined on the basis of the intensities of the ratio of the Au 4f/C 1s, assuming a standard, exponential attenuation by the monomolecular film.[99] For the attenuation lengths,[103] a series of well-defined hydrocarbon films were used. For the reference-thickness of a hecadecanethiol SAM, a value of 1.89 nm was used, which was estimated on the basis of the alkyl chain length (0.126 nm per CH_2 moiety),[90] molecular inclination (30°-33.5°),[104] and Au-S distance (0.24 nm).[162] All other references like C20 or PPP1 were calculated in a similar fashion. The packing densities were estimated from the intensity ratios of the Au 4f/S 2p emissions according to the approach already reported in the literature.[163,164] These thiolate SAMs on Au(111) served as a reference system with a well-known packing density of 4.63×10^{14} molecules/cm^2 and 0.216 nm^2/molecule.[104]

3.3.2 NEXAFS Spectroscopy

The NEXAFS spectra were collected at the same beamline as the HRXPS ones. They were measured at the carbon, nitrogen, and oxygen K-edges in the partial electron yield (PEY) mode with retarding voltages of −150 V, −300 V and −350 V, respectively. Linearly polarized synchrotron light with a polarization factor of ~88% was used as the primary X-ray source. The incidence angle of the X-rays was varied between the normal (90°) and grazing (20°) incidence geometry, to monitor the linear dichroism effects reflecting molecular orientation in the SAMs.[131] The energy resolution was ~0.3 eV at the C K-edge as well as ~0.45 eV at the N and O K-edge. The PE scale was referenced to the pronounced π* resonance of highly oriented pyrolytic graphite at 285.38 eV.[165] The spectra were corrected for the PE dependence of the incident photon flux and reduced to the standard form with zero intensity in the pre-edge region and the unity jump in the far post-edge region.

Generally two kinds of spectra are depicted: First, spectra, acquired at the so-called magic angle of X-ray incidence (55°). At his particular geometry the spectra are free of orientational effects and are representative of only the electronic structure of the studied systems.[184] Second, the difference between the spectra acquired at normal (90°) and grazing (20°) incidence of X-rays. This difference is representative of the so-called linear dichroism in X-ray absorption. Generally, the cross section of the resonant photoexcitation process depends on the orientation of the electric field vector of the linearly polarized synchrotron light with respect to the molecular orbital of interest.[131] Therefore, the intensity of characteristic absorption resonances exhibits a distinct dependence on the angle of X-ray incidence, if there is a preferable molecular orientation or an orientational order in the studied system. This can particularly be seen in the difference spectra. In addition, numerical information about the molecular orientation, averaged over the whole sample, can be derived from the entire NEXAFS data set within the standard theoretical framework.[131]

3.3.3 Kelvin Probe Measurements

Work function measurements were carried out using a UHV Kelvin Probe 2001 system (KP technology Ltd., UK). The pressure in the UHV chamber was ~10^{-10} mbar. Freshly sputtered gold was used as reference with the work function values set to 5.2 eV.[12] Work function measurements were performed both in situ, immediately after the irradiation treatment, and, for selected samples, ex situ, after the intentional exposure of the irradiated samples to ambient and their storage under these conditions (in dark) for 24 h. The measurements were carried out at room temperature.

3.3.4 Electrical Conductance Measurements

The measurements were performed with a custom-made two-terminal tunneling junction setup, based on the Keithley 2635A source meter.[142] The gold substrate and a sharp tip of EGaIn[166] served as the bottom and top electrodes, respectively.[166] Tunneling junctions were formed by contacting grounded SAM/Au samples with the EGaIn tips and applying a potential. The voltage was varied between −0.6 eV and +0.6 V range in 0.05 V steps. At least 10 I-V curved measured at several different places were recorded for each sample; average values were calculated.

3.3.5 Contact Angle Goniometry

Advancing and receding contact angles of Millipore water were measured on freshly prepared samples with custom-made, computer-controlled goniometer. The measurements were performed under ambient conditions with the needle tip in contact with the drop. At least three measurements at different locations on each sample were made. The averaged values are reported. Deviations from the average were less than ±2°.

4 Results & Discussion

4.1 Mixed Aliphatic Self-Assembled Monolayers with Embedded Polar Group

Relying on the previous work of our group regarding the single-component alkanethiolate SAMs with embedded dipoles (ester group),[22,23] I studied in detail the respective mixed monolayers taking the C10EC10-up and C10EC10-down precursors (Figure 4.1) with the opposite directions of the embedded dipole group with respect to the molecular backbone as components of these mixed SAMs.

The C10EC10-up/down molecules were custom-synthesized by our partner group from the Université Laval, Quebec, Canada (Prof. J.-F. Morin, C.-O. Gilbert, and J. Boismenu-Lavoie; Université Laval, Quebec, Canada). The substances were used as delivered.

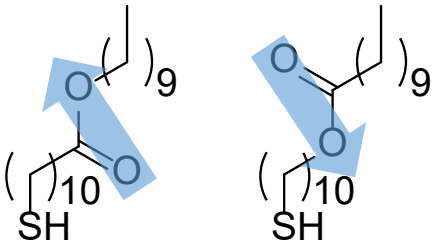

C10EC10-up C10EC10-down

Figure 4.1: Molecular structures of the C10EC10-up and C10EC10-down ester molecules with their assigned acronyms. The directions of the dipole moments of the embedded ester groups with respect to the molecular backbone are marked by blue arrows.

4.1.1 Basic Characterization

The XPS spectra of the single-component and mixed C10EC10-up − C10EC10-down films are presented in Figure 4.2. All films, single-component and mixed monolayers suggest the formation of well-defined and contamination-free SAMs.

The S 2p spectra of these monolayers are presented in Figure 4.2a; they are somewhat noisy because of the strong attenuation of the respective signal by the quite thick hydrocarbon overlayer. Nevertheless, it can be clearly distinguished that these spectra exhibit a single doublet at ~162.0 eV (S $2p_{3/2}$), representative for the thiolate species bound to noble metal surfaces,[167,170] underlying the SAM-like character of both single-component and mixed films. The intensity of this doublet does not change noticeably over the series, which suggests that the packing density of the mixed SAMs is similar to the single-component ones. This tentative

conclusion was supported by numerical evaluation of the XPS data, which gave an analogous result: a packing density of (4.5±0.3)×10^{14} cm^{-2} and a similar thickness of (2.28±0.05) nm in all monolayers studied.

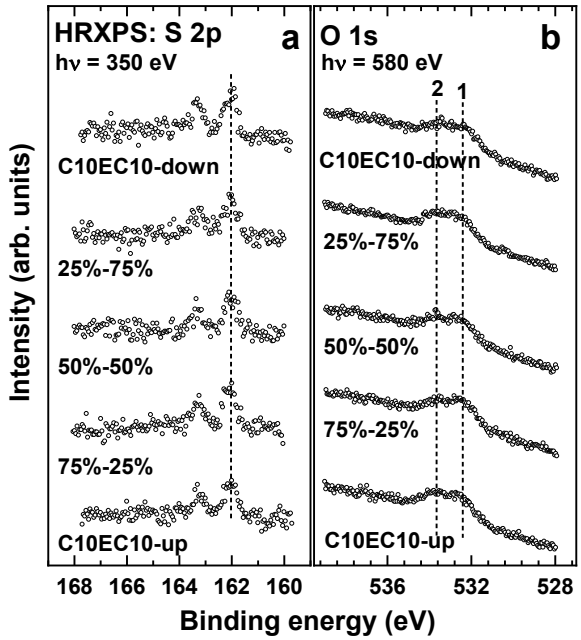

Figure 4.2: (a) S 2p and (b) O 1s XPS spectra of the single-component and mixed C10EC10-up and C10EC10-down SAMs (open circles). The compositions of the mixed SAMs reflect the relative portions of C10EC10-up (first number) and C10EC10-down (second number) in the solutions, from which the SAMs were grown. The spectra are shifted vertically for comparison. The vertical dashed lines track the positions of the S 2p doublet (S $2p_{3/2}$) and the component O 1s peaks. The numbers mark component peaks in the O 1s spectra.

The O 1s spectra are presented in Figure 4.2b. The spectra, which look similar for the entire series, exhibit two emissions at 532.4 eV (**1**) and 533.7 eV (**2**), characteristic for the ether and carbonyl oxygen, respectively. The positions and intensities of these emissions do not change noticeably over the series, which suggests (i) small electrostatic effects on these atoms and (ii) similar packing densities of all SAMs studied.

C K-edge and O K-edge NEXAFS data for the single-component and mixed C10EC10-up - C10EC10-down SAMs (and also the reference C20 monolayer) are presented in Figures 4.3 and 4.4, respectively. The data combine the 55° spectra, which are exclusively characteristic for the electronic structure of the films,[131] and the difference (90° - 20°) spectra, which are representative for the orientational order and molecular orientation in the films.[131] The spectra of the single-component and mixed C10EC10-up - C10EC10-down SAMs look very similarly, suggesting, in accordance with the XPS data, similar structure of these films.

The 55° C K-edge spectra of the single-component and mixed C10EC10-up - C10EC10-down SAMs in Figure 4.3a are dominated by a double-peak feature comprised by a resonance at 287.7 eV (**1**) frequently associated with predominantly Rydberg states of the alkyl segments[29] and the π(C*=O) resonance at 288.5 eV (**4**) related to the ester group.[22,23] The former resonance is also well visible in the spectrum of the reference C20 SAM, along with the characteristic resonances at 293.4 eV (**2**) and ~301.6 eV (**3**) related to valence, antibonding C−C σ* and C−C´ σ* orbitals of the alkyl chain, respectively.[167,168] The latter resonances are

also present in the spectra of the single-component and mixed C10EC10-up - C10EC10-down SAMs, as can be expected since they also contain alkyl segments.

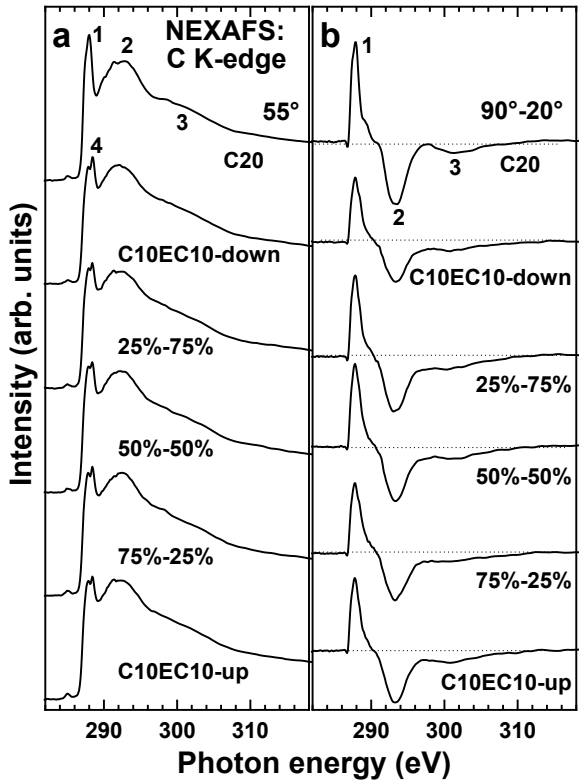

Figure 4.3: C K-edge NEXAFS data for the single-component and mixed C10EC10-up and C10EC10-down SAMs, including (a) the spectra acquired at an X-ray incidence angle of 55° and (b) the difference between the spectra acquired at X-ray incidence angles of 90° and 20°. The compositions of the mixed SAMs reflect the relative portions of C10EC10-up (first number) and C10EC10-down (second number) in the solutions, from which the SAMs were grown. The spectra are shifted vertically for comparison; the same intensity scale is applied in both panels. Numbers marks characteristic absorption resonances. Dotted lines in panel b correspond to zero.

The 55° O K-edge spectra of the single-component and mixed C10EC10-up - C10EC10-down SAMs in Figure 4.3a are dominated by a π(C=O*) resonance at 531.9 eV (**1**) related to the embedded ester group,[23,169] accompanied by several weaker resonances with π* (**2**) and σ* (**3**) character at higher photon energy.[23]

These resonances in both C and O K-edge spectra exhibit pronounced linear dichroism, that is, intensity dependence on the X-ray incidence angle, as evidenced by the appearance of the intense peaks at the positions of these resonances in the difference spectra in Figures 4.3b and 4.4b. This suggests a high orientational order, both in the single-component C10EC10-up and C10EC10-down SAMs (in agreement with the previous work)[22,23] and in the respective mixed SAMs, with an upright orientation of the molecular chains, as follows from the specific signs of the difference peaks in the 90°-20° spectra.[23]

Quantitative evaluation of the NEXAFS data in context of molecular orientation was performed with the difference method for the C K-edge and the standard intensity-versus-angle approach for the O K-edge.[131] The difference method allowed the avoidance of the spectra decomposition, nontrivial for the C K-edge spectra in the given case. The most prominent R*

and π(C=O*) resonances with the transition dipole moments perpendicular to the alkyl chain and the COO plane of the embedded ester group, respectively, were considered.

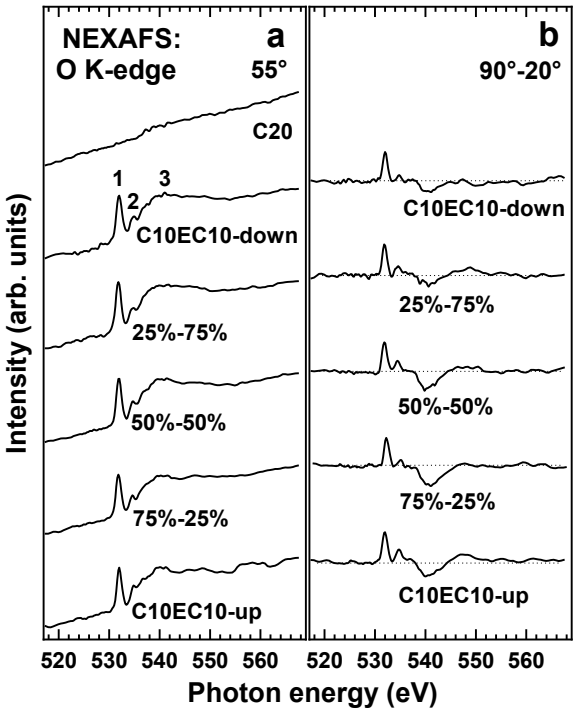

Figure 4.4: O K-edge NEXAFS data for the single-component and mixed C10EC10-up and C10EC10-down SAMs, including (a) the spectra acquired at an X-ray incidence angle of 55° and (b) the difference between the spectra acquired at X-ray incidence angle of 90° and 20°. The compositions of the mixed SAMs reflect the relative portions of C10EC10-up (first number) and C10EC10-down (second number) in the solutions, from which the SAMs were grown. The spectra are shifted vertically for comparison; the same intensity scale is applied in both panels. Characteristic absorption resonances are marked by numbers. Dotted lines in panel b correspond to zero.

Within the difference methods,[30,39] upon subtracting two NEXAFS spectra recorded at different X-ray incidence angles θ and θ_1, one gets for a plane orbital, such as R* one,

$$I_p(\theta) - I_p(\theta_1) = C(1 - 3\ \cos^2\gamma)(\cos^2\theta - \cos^2\theta_1) \qquad (\mathbf{4.1})$$

where θ is the incidence angle of X-rays, γ is the angle between the sample normal and the normal to the R* plane (i.e., the molecular tilt angle), $I_p(\theta)$ and $I_p(\theta_1)$ are the resonance intensities, and C is a normalization constant which depends on the excitation probability from the C 1s core level into a given molecular orbital. Even though the latter parameter is unknown, eq 4.1 can be used for a comparison of similar molecular orbitals in different systems or even for the quantitative evaluation of the molecular inclination, if one has a reference sample with the same molecular orbitals and a known molecular structure.

Regretfully, such a reference sample is not available in the given case since the intensity of the R* resonance depends on the alkyl chain length because of delocalization of the respective molecular orbital over the entire chain,[34,36] but the orbitals of both segments in the mid-ester molecules can be somehow coupled resulting in an intensity value somewhere between those for the C10 and C20. At the same time, we can compare the single-component and mixed films and calculate the tilt angles of the mixed SAMs using the known values of the tilt angles for the single-component films as a reference. Accordingly, $I_p(\theta) - I_p(\theta_1)$ for all these films are plotted

in Figure 4.5 as a function of $cos^2(\theta) - cos^2(\theta_1)$, with the slopes of the respective straight lines representative of the values of γ (see eq 4.1). As seen in this plot, the lines of the single-component C10EC10-up and C10EC10-down SAMs have similar slopes, suggesting, in accordance with the literature data,[19,20] similar molecular inclination (31°±4°, averaged over both segments). The lines for the mixed SAMs exhibit a similar slope as well, which is even slightly steeper as compared to that for the single-component films and which is composition independent. Thus, the molecular inclination and the orientational order in the mixed SAMs are similar to those in the single-component. The average molecular tilt angle in the mixed SAMS was estimated at 27°±4°, the same for all compositions.

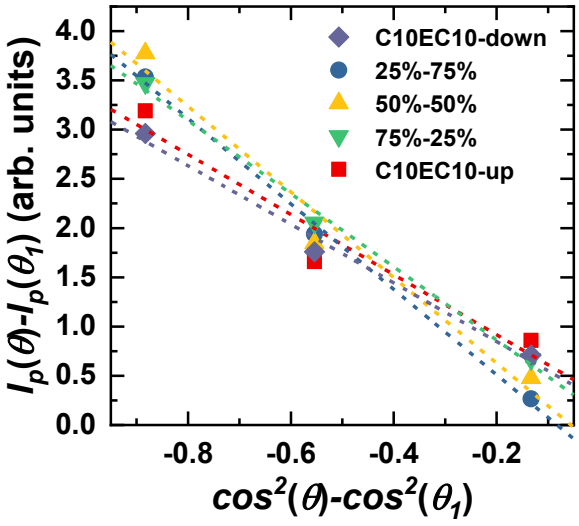

Figure 4.5: Intensity differences for the R* resonance in the C K-edge NEXAFS spectra of the single-component and mixed C10EC10-up and C10EC10-down SAMs versus $\cos^2(\theta) - \cos^2(\theta_1)$. The legend is given in the plot. The color-coded dashed lines represent the best linear fits to the experimental data. The compositions of the mixed SAMs reflect the relative ratios of C10EC10-up (first number) and C10EC10-down (second number) in the solutions, from which the SAMs were grown.

Within the evaluation of the O K-edge data, the intensity of the π(C=O*) resonance was plotted as a function of θ and was compared to a theoretical dependence for a vector-type orbital following the standard approach.[30] This procedure resulted in similar average tilt angles of the π(C=O*) orbital in the single-component and mixed mid-ester SAMs, namely, 27°±4°, in good agreement with the previous data for this evaluation, along with that for the C K-edge NEXAFS data. This suggests that the mixed mid-ester films have similar orientational order and molecular inclination as the single-component ones.

4.1.2 Morphology and Electrostatic Properties

As shown recently,[20,25] XPS can be used as a sensitive tool to study polar SAMs, including mixed ones. The approach is based on electrostatic effects in photoemission, exhibited in the C 1s spectra.[25] These spectra for the single-component mid-ester SAMs and reference C20 monolayer are presented in Figure 4.6a. The spectrum of the latter film is typical of non-substituted AT SAMs, exhibiting a single peak stemming from the alkyl backbone at a BE of ~285.0 eV.

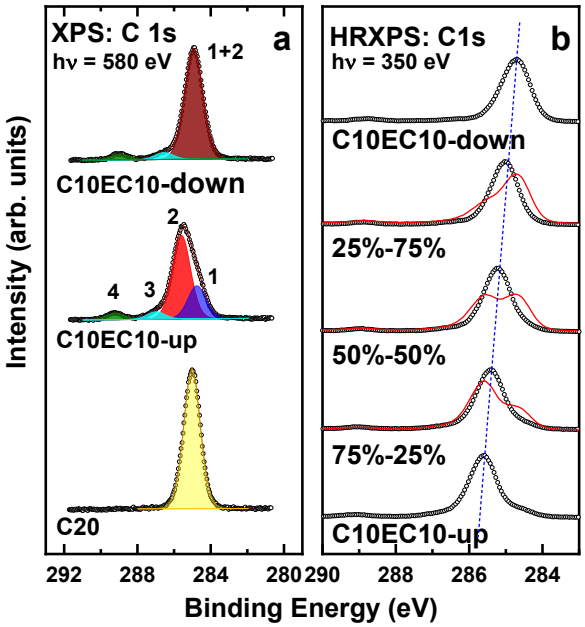

Figure 4.6: (a) C 1s XPS spectra (580 eV) of the single-component C10EC10-up and C10EC10-down SAMs in addition with the C 1s spectrum of the C20 reference SAM. The C 1s spectra are decomposed in the individual component peaks, highlighted in different colors and marked by numbers. (b) Single-component and the mixed monolayers (350 eV) of different compositions (open circles), along with simulations of the latter spectra for the case of the phase separation (solid red lines). The compositions of the mixed SAMs reflect the relative portions of C10EC10-up (first number) and C10EC10-down (second number) in the solutions, from which the SAMs were grown. The positions of the dominant component peak, representative for the top segment of the assembled C10EC10-up and C10EC10-down molecules, are tracked by a vertical dashed line.

This peak has a certain “fine structure”, but it is hardly perceptible and can only be recognized within a very detailed analysis.[170,171] In contrast to C20, the C 1s spectrum of the C10EC10 SAM exhibits not one but two major peaks at ~284.6 eV (**1**) and ~285.6 eV (**2**), related to the bottom and top alkyl segments, respectively, and also the comparably weak peaks at 286.8 eV (**3**) and 289.2 eV (**4**) associated with the ether and carbonyl carbon, respectively. The “splitting” of the single peak into two upon the midchain ester substitution stems from the potential discontinuity (step) inside the monolayer associated with the embedded dipolar ester group.[22,23,25] This step occurs in the opposite direction in the case of the C10EC10-down SAM, leading to the shift of the top segment peak toward that of the bottom segment. As a result, both these peaks overlap in the single one (**1 + 2**), shifted to a lower BE (~284.65 eV) as compared to the reference C20 case. The minor peaks related to the ether (**3**) and carbonyl (**4**) carbon are visible as well, with only slightly different BEs as compared to the spectrum of the C10EC10-up monolayer.

The spectra presented in Figure 4.6a were acquired at a photon energy of 580 eV allowing to see more clearly the peak stemming from the bottom segment of the C10EC10-up and C10EC10-down SAMs−due to a moderate attenuation of the respective signal at the resulting kinetic energy of the photoelectrons. The electrostatic effects in the mixed SAMs can, however, be better monitored using the spectra acquired at a lower photon energy since, due to the strong attenuation of the photoelectron signal, they are almost exclusively representative of the top alkyl segment of the SAMs, reflecting the electrostatic effect of the embedded ester

groups most clearly. Such spectra, collected at a photon energy of 350 eV for the single-component and mixed C10EC10-up and C10EC10-down SAMs, are presented in Figure 4.6b. The spectra of the single-component films are indeed dominated by the peak associated with the top alkyl segment (with similar widths for the C10EC10-up and C10EC10-down films), and all other features are comparably weak. The spectra of the mixed monolayers should represent a superposition of those of the single-component films, with a proper impact of the electrostatic effects. The character of the superposition depends, however, on the film morphology, namely, the kind of intermolecular mixing.[20] A homogeneous mixing will result in a homogeneous potential step within the monolayer, with the amplitude defined by the weighted sum of the individual dipoles, depending on the mixing ratio. Accordingly, the BE shift and, consequently, the BE position of the peak related to the top alkyl segment should change continuously with the mixing ratio between the ultimate values for the C10EC10-up and C10EC10-down SAMs. In contrast, in the case of the phase separation and sufficiently large C10EC10-up and C10EC10-down domains, they will contribute individually into the spectra, which then will represent a linear combination of the single-component spectra, with the weights corresponding to the composition of the mixed films. In the case of the phase separation but small domains, down to the molecular level, the spectra will generally behave similarly to the case of the homogeneous intermolecular mixture but will be broadened as compared to the single component case.[20]

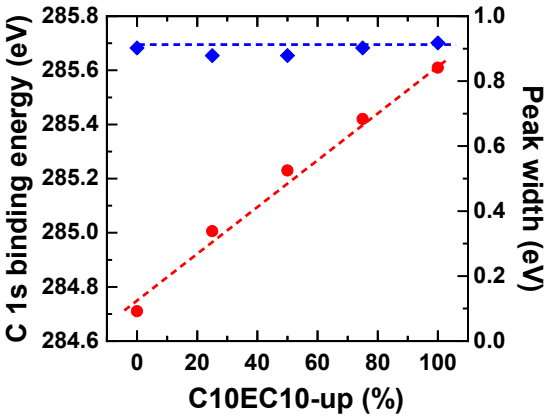

Figure 4.7: Dependence of the BE position (red circles, left axis) and FWHM (blue diamonds, right axis) of the dominant component peak in the C 1s XPS spectra of the single-component and mixed C10EC10-up and C10EC10-down SAMs on the ratio of C10EC10-up in the solutions, from which the SAMs were grown. The linear dependence of the BE position and the constancy of the FWHM are highlighted by the color-coded dashed lines.

The continuous change in the mid-SAM potential step, traced indirectly by the C 1s spectra, could be directly monitored by the measurement of the work function of the single-component and mixed C10EC10-up and C10EC10-down SAMs. The respective results are presented in Figure 4.8, along with the analogous data for the pyrimidine-substituted monolayers[18] given for comparison.

The experimental spectra of the mixed SAMs in Figure 4.6b are clearly dominated by a single peak (accompanied by minor features) with a continuous shift in the peak position with the varied mixing ratio. These spectra differ distinctly from the simulated spectra for the phase separation in large domains, shown as well in Figure 4.6b. Moreover, as demonstrated in Figure 4.7, the FWHM's of the dominant peak in the spectra of the mixed films are, within the

experimental error, identical to those for the single-component films. This suggests that the scenario of the phase separation can be excluded and that the mixed SAMs represent homogeneous mixtures of the molecules. In this situation, the BE shift of the dominant peak in the C 1s spectra should represent a fingerprint of the mixing ratio in the monolayer, which can be different from that in solution. To monitor this effect, the BE position is plotted as a function of the SAM composition in Figure 4.7. The observed dependence has a linear character (within the error of the experiment), which suggests that the composition in solution is mimicked in the SAMs. Interestingly, this situation is distinctly different from the aromatic SAMs with the embedded dipolar pyrimidine group, where a 50−50% composition is preferable for the mixed SAMs, because of the stabilizing head to tail arrangement of the neighboring dipoles.[20] Obviously, for the C10EC10-up and C10EC10-down mixtures, the impact of the dipole-dipole interaction on the SAM composition is much lower, presumably, in view of much stronger contribution associated with the intermolecular interaction of the comparably long alkyl segments.

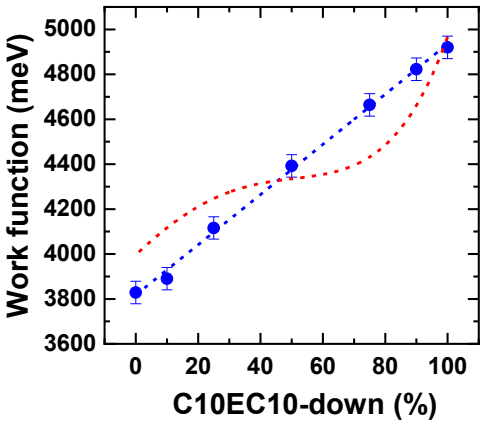

Figure 4.8: Dependence of the work function of the single-component and mixed C10EC10-up and C10EC10-down SAMs (blue circles) on the portion of C10EC10-down in the solutions, from which the SAMs were grown. The linear character of this dependence is highlighted by the blue dashed line. For comparison, an analogous curve for the aromatic SAMs with embedded pyrimidine group is given (red dashed line);[20] this curve is shifted by +0.15 eV.

In full agreement with the C 1s XPS data, the work function of the mixed SAMs varies continuously and in a linear fashion between the ultimate values for the C10EC10-up monolayer (3.83 eV) and the C10EC10-down film (4.92 eV). This behavior is in a striking contrast to the S-like curve for the pyrimidine-substituted monolayers, reflecting the predominance of the 50−50% composition. Thus, the work function data support and evidence the conclusion that the solution composition is fully mimicked in the SAMs at the co-adsorption of the C10EC10-up and C10EC10-down precursors. On the other hand, from a practical viewpoint, these data suggest that the work function of gold can be varied continuously and in controlled fashion in the ~1.1 eV range by mixed C10EC10-up - C10EC10-down monolayers.

4.2 Mixed Monomolecular Films with Embedded Dipolar Groups on Ag(111)

As the next task, I studied the applicability of the embedded dipole concept to different substrates, taking Ag(111) as a representative example. Along these lines, I studied both aliphatic and aromatic SAMs (Figure 4.9) with the suitable embedded polar groups (ester and pyrimidine, respectively) directed electrostatically either to or from the substrate as well as mixed monolayers comprising the molecules with the opposite orientations of the embedded dipoles.

The C10EC10-up/down precursors were custom-synthesized by our partner group (Prof. J.-F. Morin and G. Charles-Olivier; Université Laval, Quebec, Canada). The PPmP1-up/down precursors were custom-synthesized by another partner group (Prof. A. Terfort; Frankfurt University). The substances were used as delivered.

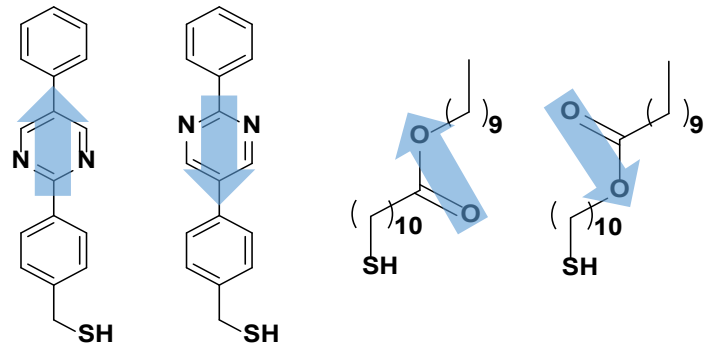

PPmP1-up **PPmP1-down** **C10EC10-up** **C10EC10-down**

Figure 4.9: The structures of the aromatic and aliphatic SAM precursors used in this study, along with their acronyms. For the aromatic SAMs, Pm, P, and "1" mean pyrimidine, phenyl, and number of the methylene groups in the aliphatic linker, respectively. For the aliphatic SAMs, C_n refers to the number of the methylene and methyl moieties in the segments above ("top") and below ("bottom") of the ester (E) group. The directions of the dipole moments of the embedded dipolar pyrimidine and ester groups with respect to the molecular backbone (upright molecular orientation with the thiolate anchor to the substrate) are marked by blue arrows. They are included as "up" and "down" in the acronyms.

4.2.1 XPS

The XPS data of both single-component and mixed C10EC10-up/down and PPmP1-up/down films imply the formation of well-defined and contamination-free SAMs. In particular, the S 2p spectra of all these monolayers (Figure 4.10) exhibit a single doublet at ~162.0 eV (S $2p_{3/2}$), representative for the thiolate species bound to noble metal substrates,[167,170] underlying the SAM character of both single-component and mixed films. The intensity of this doublet, as well as the intensities of the Ag 3d, O 1s and N 1s signals (not shown), are nearly persistent over

the entire C10EC10-up/down and PPmP1-up/down series, suggesting that the molecular packing density does not change noticeably upon the change in the orientation of the embedded dipole and mixing the molecules with the opposite dipole orientations. At the same time, the exact composition of the mixed SAMs could not be straightforwardly determined from the XPS data since the spectroscopic signatures of the differently oriented dipolar groups in the O 1s spectra of the C10EC10-up/down SAMs[26] and in the N 1s spectra of the PPmP1-up/down monolayers[19] are nearly identical.

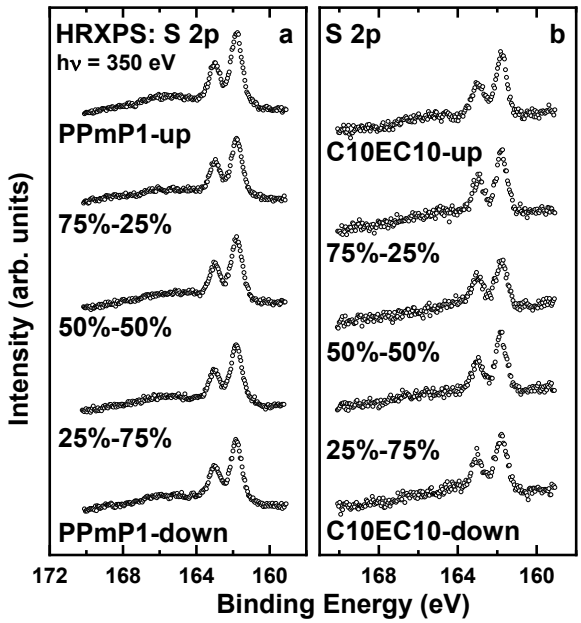

Figure 4.10: S 2p XPS spectra of the single-component and mixed (a) PPmP1-up/down and (b) C10EC10-up/down monolayers of different compositions. The spectra are shifted vertically for comparison. The compositions of the mixed SAMs reflect the relative portions of the "up" (first number) and "down" (second number) molecules in the solutions, from which the SAMs were grown.

This information can, however, be obtained from the C 1s data presented in Figure 4.11, relying on the electrostatic effects in photoemission. Accordingly, the introduction of the embedded dipole into the molecular backbone in a SAM results in the electrostatic shift of the C 1s peak associated with the backbone segment located above the group (top segment) as compared to that located below (bottom segment) even if both segments are chemically identical.[19,22,25] The value of this shift is proportional to the electrostatic field provided by the embedded dipolar groups, which is determined by their density, dipole moment and orientation.[20,26]

The spectra in Figure 4.12 were intentionally acquired at a photon energy of 350 eV corresponding to especially strong attenuation of the C 1s signal.[99] Consequently, the dominant component peak in these spectra is mostly representative for the top segment of the respective backbone, namely the terminal phenyl ring for the PPmP1-up/down SAMs and the top alkyl segment for the C10EC10-up/down monolayers.

The C 1s spectra of the single-component PPmP1-down and PPmP1-up SAMs in Figure 4.11a are similar to the analogous spectra of these monolayers on Au,[19,20] exhibiting characteristic peaks related to the top and bottom phenyl rings as well as to the carbon atoms in the pyrimidine ring (see ref 19 for the exact assignments). These spectra show distinctly different positions of the dominant peak (~284.1 eV and ~284.9 eV, respectively), reflecting the effect

of the embedding dipolar pyrimidine groups. The spectra of the mixed SAMs show a continuous shift of this peak between the ultimate values for the single-component monolayers, with the respective BE positions given in Figure 4.12a. Such a continuous shift, along with the nearly constant FWHM of the dominant peak, are in distinct contrast with a weighted superposition of the spectra of the single-component PPmP1-up and PPmP1-down SAMs as could be expected for the case of phase separation in the mixed monolayers.[20] Consequently, the spectra in Figure 4.11a suggest a homogeneous mixture of both components in the mixed SAMs.

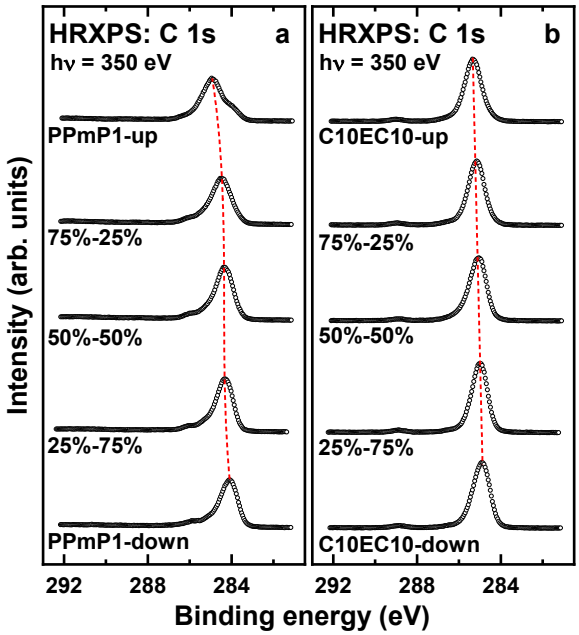

Figure 4.11: C 1s XPS spectra of the single-component and mixed PPmP1-up/down (a) and C10EC10-up/down (b) monolayers of different compositions. The spectra are shifted vertically for comparison. The compositions of the mixed SAMs reflect the relative portions of the "up" (first number) and "down" (second number) molecules in the solutions, from which the SAMs were grown. The positions of the dominant component peak, representative for either the terminal phenyl ring (a) or top alkyl segment (b) of the assembled molecules, are tracked by the red dashed lines.

The C 1s spectra of the single-component C10EC10-down and C10EC10-up SAMs in Figure 4.12b are similar to the analogous spectra of these monolayers on Au,[22,26] exhibiting characteristic peaks related to the top and bottom alkyl segment as well as to the carbonyl and ether carbon atoms associated with the embedded ester group (see ref 22 for the exact assignments). These spectra show somewhat different positions of the dominant peak (284.9 eV and 285.2 eV, respectively), reflecting the effect of the embedding dipolar ester groups. The spectra of the mixed SAMs reveal a continuous shift of this peak between the ultimate values for the single-component monolayers, with the respective BE positions given in Figure 4.12b. Similar to the PPmP1-up/down case and according to the literature,[20] such a continuous shift, along with the persistent FWHM of the dominant peak suggest a homogeneous mixture of both components in the mixed SAMs.

The difference between the ultimate values of the C 1s binding energy in Figures 4.12a and 4.12b reflect the electrostatic effect of the embedded dipole in the case of the Ag(111) substrate, whereas the exact shape of the respective curves, which are distinctly different for the PPmP1-up/down and C10EC10-up/down systems, reflects the difference between the

compositions of the parent solutions and resulting mixed SAMs. As to the difference between the ultimate values, this parameter for the PPmP1-up/down SAMs on Ag (~0.8 eV) is comparable with that for Au (~1.05 eV)[19,20], whereas the difference for the C10EC10-up/down monolayers on Ag (~0.3 eV) is much smaller than that for Au (~1.1 eV)[22,26]. Since the density of the SAMs on Ag is comparable with that on Au (and, most likely, even somewhat higher, at least for the C10EC10-up/down films),[104] the above behavior can only be explained by orientation effects.

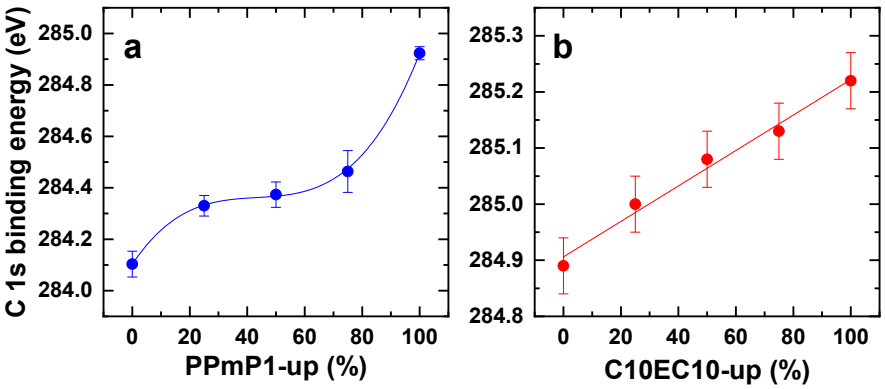

Figure 4.12: Dependence of the BE position (blue and red circles) of the dominant component peak in the C 1s XPS spectra of the single-component and mixed PPmP1-up/down (a) and C10EC10-up/down (b) SAMs on the portion of PPmP1-up (a) or C10EC10-up (b) in the solutions, from which the SAMs were grown. The character of the dependence is highlighted by the red and blue lines.

As to the exact shape of the curves in Figure 4.12, they reflect the variation of the "internal" electrostatic shift associated with the embedded dipolar groups and, in this sense, are representative for the composition of the mixed SAMs - since the value of the electrostatic shift is determined by the portions of the molecules with the oppositely directed dipoles. In accordance with such an interpretation, the curves in Figure 4.12 show significant deviation of the composition of the mixed SAM from that in the solution for the PPmP1-up/down system (Figure 4.12a; a S-like curve) and an almost linear relation between the solution/SAM compositions for the C10EC10-up/down system (Figure 4.12b). Interestingly, this behavior mimics that for the Au substrate[20,26] and can be tentatively explained with the same line of arguments. Accordingly,[20] for the aromatic SAMs with the embedded dipolar pyrimidine group, building a considerable part of the molecular backbone, a 50%−50% composition is preferable for the mixed SAMs, because of the stabilizing head to tail arrangement of the neighboring dipoles (in the sense of their interaction), giving the observed S-like deviation. In contrast, the impact of the dipole-dipole interaction on the SAM composition is much lower in the C10EC10-up/down case, most likely, in view of much stronger contribution associated with the intermolecular interaction of the comparably long alkyl segments.[26]

4.2.2 Work Function

An alternative way to monitor the electrostatic effects of the embedded dipolar groups is the work function which also has a practical importance in context of SAM-mediated energy level alignment at the electrode-organic semiconductor and electrode-buffer layer interfaces in

organic electronics and photovoltaics. The work function of the single-component and mixed PPmP1-up/down and C10EC10-up/down SAMs is presented in Figure 4.13. Apart from the fact, that the shift of the C 1s XPS peak of the top segment and the work function variation occur in the opposite directions, the curves in Figure 4.13 mimic those in Figure 4.12, which is understandable in view of the same underlying factor (electrostatic effect of the embedded dipolar groups). For the PPmP1-up/down SAMs, the work function is varied between 5.0 eV and 4.15 eV (~0.85 eV range), exhibiting the preference of the 50%-50% composition for the mixed SAMs as follows from the observed shape of the curve in Figure 4.13a. This is comparable with the case of Au, where the work function of these SAMs is varied between 4.8 eV and 3.8 eV (~1 eV range)[20,26] exhibiting the preference for the 50%-50% composition as well.[15] Note that the work functions of the clean Ag(111) and Au(111) substrates are 4.53 eV and 5.33 eV, respectively,[172] but the work function of the respective evaporated films can be slightly different. Nevertheless, taking 4.53 eV as the reference, it could be seen hat the deposition of the C10EC10-up/down SAMs results mostly in the lowering of the work function, whereas the assembly of the PPmP1-up/down monolayers allows both, decrease and increase of the work function of Ag in a quite broad range. This situation is even more favorable as compared to the Au substrate, where, in spite of the broader range, only decrease of the work function is possible with the PPmP1-up/down SAMs.[19,20,]

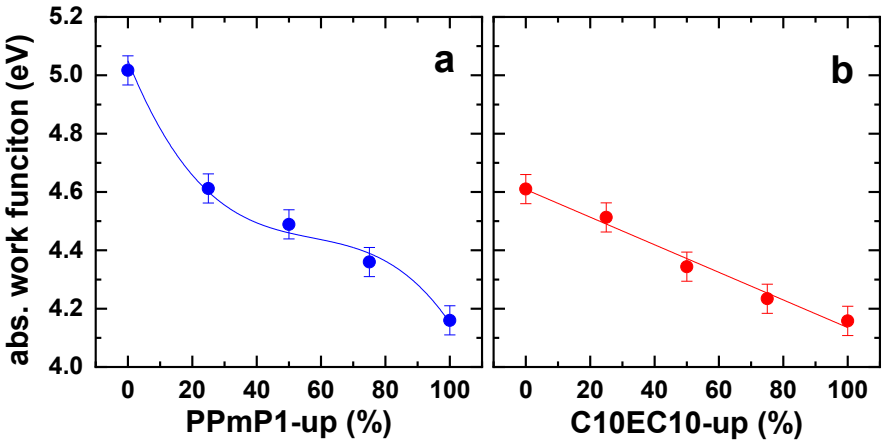

Figure 4.13: Dependence of the work function (blue and red circles) of the single-component and mixed PPmP1-up/down (a) and C10EC10-up/down (b) SAMs on the portion of PPmP1-up (a) or C10EC10-up (b) in the solutions, from which these monolayers were grown. The character of the dependence is highlighted by the red and blue lines.

For the C10EC10-up/down SAMs (Figure 4.13b), the work function is varied between 4.6 eV and 4.15 eV (~0.45 eV range), exhibiting a nearly linear behavior as a function of the solution composition suggesting negligible deviations in the composition of the mixed SAMs. Whereas the same linear behavior was observed for the Au substrate as well,[26] the range of the work function variation was noticeably larger, viz. from 4.8 eV to 3.8 eV (~1 eV interval).[26]

4.2.3 NEXAFS Spectroscopy

As mentioned above, the difference in the electrostatic effect of the embedded dipolar groups for the SAMs on Ag and Au substrates is most likely related to specific molecular orientation on these two supports. A suitable approach to monitor this parameter is NEXAFS spectroscopy which also provides information about the chemical composition of the samples studied. As an example of such an information, the N K-edge and O K-edge NEXAFS spectra of the single-component and mixed PPmP1-up/down and C10EC10-up/down SAMs were measured and presented in Figure 4.14.

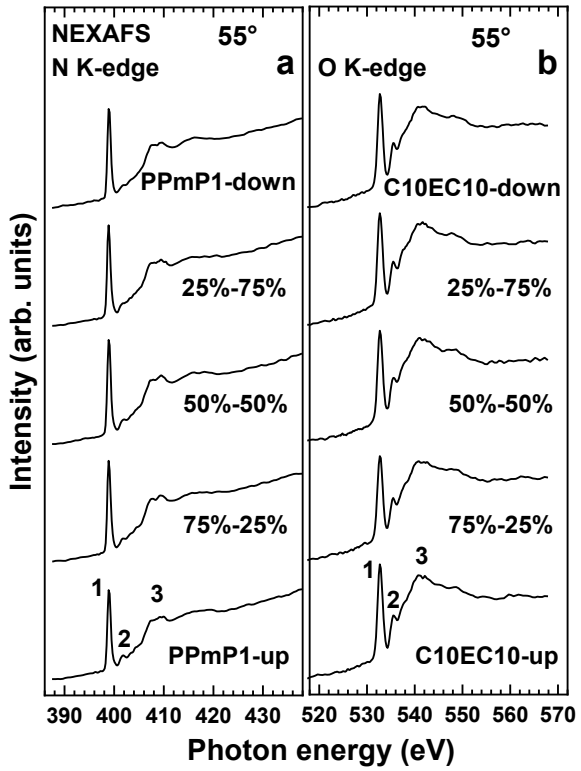

Figure 4.14: N K-edge (a) and O K-edge (b) NEXAFS spectra of the single-component and mixed PPmP1-up/down (a) and C10EC10-up/down (b) SAMs on Ag. The spectra were acquired at an X-ray incidence angle of 55° (magic angle); at this particular orientation the spectra are not affected by molecular orientation effects and are entirely representative of the electronic structure.[131] The compositions of the mixed SAMs reflect the relative portions of the "up" (first number) and "down" (second number) molecules in the solutions, from which the SAMs were grown. The spectra are shifted vertically for comparison. Characteristic absorption resonances are marked by numbers.

The 55° N K-edge NEXAFS spectra of the single-component and mixed PPmP1-up/down SAMs in Figure 4.14a exhibit characteristic features of pyrimidine,[176,177] viz. a strong π* resonance at ~398.5 eV (**1**), a mixed π*-Rydberg feature at 402.7 eV (**2**), and further Rydberg and σ*-like resonances at higher excitation energies. The spectra of the PPmP1-up and PPmP1-down SAMs look almost identical, which is understandable in context of the identical chemical composition of the precursors (Figure 4.9). Of primary importance is, however, nearly the same intensity of the absorption resonances for the single-component and

mixed monolayers, suggesting a persistent packing density over the series. Similar situation occurs for the single-component and mixed C10EC10-up/down SAMs, the spectra of which in Figure 4.14b exhibit characteristic features of the ester group,[169,173] namely a π(C=O*) resonance at 531.9 eV (**1**) as well as several weaker resonances with the π* (**2**) and σ* (**3**) character at higher photon energies (see ref 179 for the exact assignments).

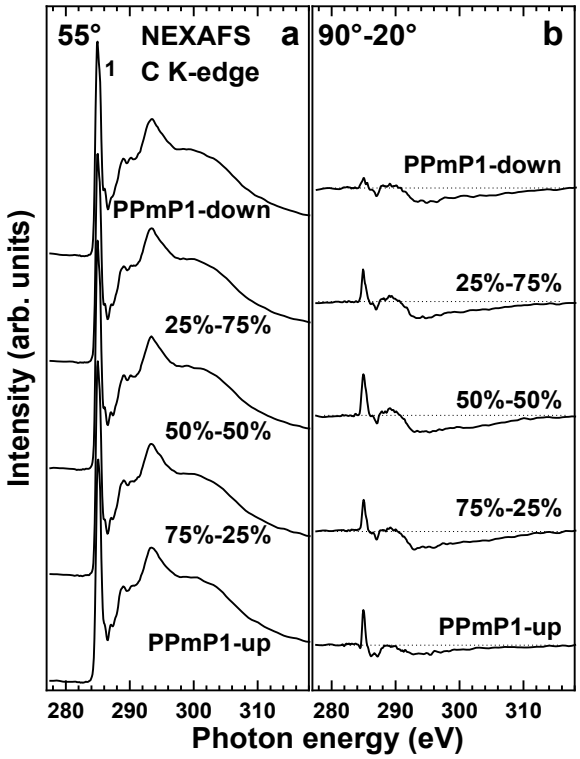

Figure 4.15: C K-edge NEXAFS data for the single-component and mixed PPmP1-up and PPmP1-down SAMs, including the spectra acquired at an X-ray incidence angle of 55° (a) and the difference between the spectra acquired at X-ray incidence angles of 90° and 20° (b). The compositions of the mixed SAMs reflect the relative portions of PPmP1-up (first number) and PPmP1-down (second number) in the solutions, from which the SAMs were grown. The spectra are shifted vertically for comparison; the same intensity scale is applied in both panels. The dominant absorption resonance is marked (see text for details). Dotted lines in panel (b) correspond to zero.

The above data were complemented by the C K-edge spectra which were measured in the angle-variation fashion providing information on both chemical composition and molecular orientation. Representative NEXAFS data for the single-component and mixed PPmP1-up and PPmP1-down SAMs are shown in Figure 4.15. Both magic angle (Figure 4.15a) and difference (Figure 4.15b) spectra are presented, with the latter ones reflecting the linear dichroism effects. Apart from few minor differences, the 55° spectra of the PPmP1-up and PPmP1-down SAMs as well as these of the mixed SAMs are very similar to each other and agree well with the literature data for the single-component films on Au(111).[19] They are dominated by the characteristic π_1^* resonance (**1**), consisting of three features at 284.85/285.0 eV, 285.3 eV and 286.0 eV (shoulder-like), and accompanied by a variety of π^*- and σ^*-like resonances at higher excitation energies (see refs 19 and 176 for the exact assignments).

The difference spectra of the single-component and mixed PPmP1-up and PPmP1-down SAMs in Figure 4.15 exhibit distinct peaks at the positions of the characteristic absorption resonances, suggesting a certain orientational order in these monolayers. The amplitudes of

these difference peaks do not vary much over the series, except for the spectrum of the single-component PPmP1-down SAM where the amplitude is somewhat smaller.

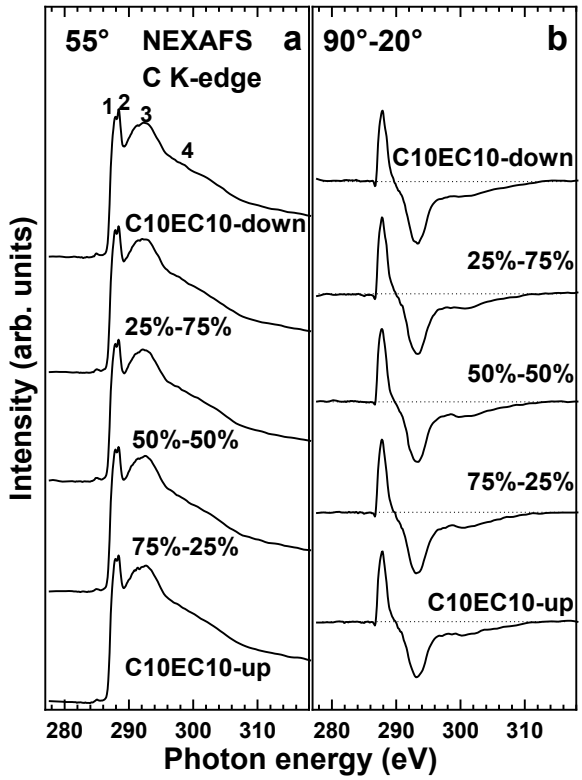

Figure 4.16: C K-edge NEXAFS data for the single-component and mixed C10EC10-up and C10EC10-down SAMs, including the spectra acquired at an X-ray incidence angle of 55° (a) and the difference between the spectra acquired at X-ray incidence angles of 90° and 20° (b). The compositions of the mixed SAMs reflect the relative portions of C10EC10-up (first number) and C10EC10-down (second number) in the solutions, from which the SAMs were grown. The spectra are shifted vertically for comparison; the same intensity scale is applied in both panels. Characteristic absorption resonances are marked by numbers. Dotted lines in panel (b) correspond to zero.

The signs of the difference peaks imply upright molecular orientation.[19] Numerical evaluation of the entire set of the NEXAFS data within the standard formalism for the vector-type orbital,[131] which was the π_1^* in the given case, gave the average tilt angles of 56-59° for the entire PPmP1-up/down series, corresponding to average molecular tilt angles of 31-34°(with ±3° error bar). The latter angles are larger as compared to those for the single component PPmP1-up and PPmP1-down SAMs on Au, viz. 18° and 17°, respectively.[19] The respective difference explains the difference between the work function ranges achieved with the PPmP1-up/down SAMs on Ag and Au (~0.8 eV vs. ~1.05 eV[19]) since a larger molecular inclination means a smaller projection of the embedded dipole, directed along the molecular backbone, onto the surface normal and, consequently, a smaller electrostatic effect of the entire SAM.

The C K-edge NEXAFS data for the single-component and mixed C10EC10-up/down SAMs are presented in Figure 4.16. Similar to the PPmP1-up/down case (Figure 4.15), the data combine the 55° spectra (Figure 4,16a) and the difference, 90°-20° curves (Figure 4.16b). The spectra of the single-component and mixed C10EC10-up - C10EC10-down SAMs look very

similarly to each other, suggesting, in accordance with the XPS data, similar structure of these films. The 55° spectra in Figure 4.16a are dominated by the merged Rydberg (R*) resonance of the alkyl segments at ~287.7 eV[129] (**1**; there are also alternative assignments)[167] and the π(C*=O) resonance of the ester group at 288.5 eV[23,174] (**2**). This double feature is accompanied by the characteristic resonances at ~293.4 eV (**3**) and ~301.6 eV (**4**) associated with the valence, antibonding C-C σ* and C-C' σ* orbitals of the alkyl chain, respectively.[167,168]

The difference spectra of the single-component and mixed C10EC10-up and C10EC10-down SAMs in Figure 4.16b are almost identical, exhibiting pronounced peaks at the positions of the characteristic absorption resonances of the alkyl chains. This suggest similar, quite high orientational order in all these SAMs, with the molecular chains having an upright orientation, as follows from the specific signs of the difference peaks taking into account the orientation of the respective molecular orbitals.[23] Since the evaluation of the NEXAFS data for the C10EC10-up/down SAMs within the standard approach relying on the intensity-vs-angle dependence for selected absorption resonances[131] is not that straightforward as in the PPmP1-up/down case, an alternative, "difference" method was applied.[131,175] Within this method, one monitors the difference in the intensity of a selected absorption resonance upon X-ray incidence angle variation and fits it to the theoretical expression (for a plane orbital)

$$I_p(\theta_1) - I_p(\theta_2) = C(1 - 3\cos^2\gamma)(\cos^2\theta_1 - \cos^2\theta_2) \qquad \textbf{(4.2)}$$

Where θ_1 and θ_2 are two different incidence angles of X-rays, γ is the angle between the sample normal and the normal to the orbital plane, $I_p(\theta_1)$ and $I_p(\theta_2)$ are the resonance intensities, and C is a normalization constant which depends on the excitation probability from the selected core level into a given molecular orbital.[131] The latter parameter is generally unknown but can be derived from the measurements on a reference sample which has the same molecular orbital and a known molecular structure.

As a suitable orbital, the R* one, with a plane-like character, was selected. The normal to the orbital plane is directed along the alkyl backbone, so that γ in eq 4.2 will be the molecular tilt angle, average over both individual molecules and their top/bottom segments. NEXAFS spectroscopy cannot distinguish between these segments since they are chemically identical and the electrostatic effects do not affect the NEXAFS spectra. As a suitable reference sample, the single-component C10EC10-up SAM on Au was chosen. The average tilt angle of the alkyl chains in this sample was estimated at ~30° by the dedicated infrared spectroscopy experiments.[22,23]

The R* resonance intensity data for the single-component and mixed C10EC10-up and C10EC10-down SAMs are presented in Figure 4.17 in the fashion corresponding to eq 1, particularly. $I_p(\theta_1) - I_p(\theta_2)$ versus $\cos^2\theta_1 - \cos^2\theta_2$. The observed dependences could be indeed adequately fitted by the straight lines. The slopes of these lines, which appear noticeably steeper in the case of Ag as compared to Au, give then the values of γ (see eq 1) which were estimated at 17.5-18.5° (with ±3° error bar) for both single-component and mixed C10EC10-up and C10EC10-down SAMs. This average molecular tilt angle is somewhat higher than the literature value for non-substituted alkanethiolate SAMs on Ag (~12°; but higher values are also frequently reported)[104] but distinctly smaller than that for the C10EC10-up/down monolayers on Au (~30°).[22,23] Such a smaller molecular inclination in the case of Ag means a noticeably larger angle between the imbedded dipole, strongly tilted with respect to the molecular chain, and the surface normal.

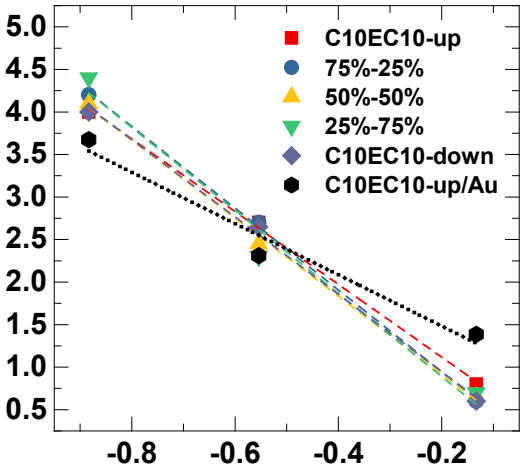

Figure 4.17: Intensity differences for the R* resonance in the C K-edge NEXAFS spectra of the single-component and mixed C10EC10-up and C10EC10-down SAMs on Ag(111) versus $\cos^2(\theta_1)$-$\cos^2(\theta_2)$. θ_2 was fixed at 55°; θ_1 was varied. The legend is given in the plot. The color-coded dashed lines represent the best linear fits to the experimental data. The compositions of the mixed SAMs reflect the relative portions of C10EC10-up (first number) and C10EC10-down (second number) in the solutions, from which the SAMs were grown. The data for the single-component C10EC10-up SAMs on Au(111) are used as a reference.

Consequently, the projection of the dipole moment on the substrate normal, determining the electrostatic effect of the embedded dipoles, should be significantly smaller on Ag than on Au, which explains the comparably small shifts of the dominant component peak in the C 1s XPS spectra and the comparably small range of the work function variation for the C10EC10-up/down SAMs on Ag. Generally, the specific orientation of the dipole moment of the embedded ester group with respect to the alkyl backbone makes the electrostatic effect of this group quite prone to the molecular orientation, which is presumably valid not only for the Ag substrate but for other potential supports as well. Of course, the twist of the alkyl segments, along the molecular axis, affects the orientation of the embedded dipole as well, but the tilt is of major importance.

4.2.4 Additional Aspects

In addition to the structural and electrostatic properties of the embedded dipole SAMs, there are several other aspects that are of importance in context of their technological applications, independent of the substrate. The first aspect is their electric transport properties, which, according to the general knowledge on this subject,[28-30] should be superior for the PPmP-up/down SAMs as compared to the C10EC10-up/down monolayers, making the former films better suitable for the interface engineering in organic electronics and photovoltaics, unless it is a gate engineering where one would rather like a higher resistance to decrease gate leakage current. Note that the major factor is not the molecular length, which is longer in the C10EC10-up/down case but the character of the molecular backbone,[28-30] which is mostly aromatic for PPmP1-up/down and aliphatic for C10EC10-up/down. Of course, the introduction of the methylene linker decouples to some extent the electronic subsystems of the metal

substrate and conjugated segment,[32-34] but this effect is small as compared to the low electric conductance of the long, pure aliphatic C10EC10-up/down chains. Further, according to the available experimental data, the introduction of the embedded dipolar group and its orientation does not change the electric transport properties significantly, apart from variation of the transition voltage and a slight asymmetry in conductance, which are special issues.[178,179] This was directly demonstrated for the PPmP1-up and PPmP1-down SAMs on Au(111)[178,179] and can be assumed for the C10EC10-up/down monolayers as well, based on the results of the experiments for a variety of alkanethiolate SAMs with terminal and embedded polar groups.[24] Finally, in view of the results for the PPmP1-up and PPmP1-down SAMs on Au(111),[178] there is also no noticeable variation in the electric transport properties between the single component and mixed SAMs for both PPmP1-up/down and C10EC10-up/down series expected. The second aspect is SAM stability, which can be considered as especially critical for substrates prone to oxidation, such as Ag(111). The major factors here are exposure to ambient oxygen and light,[16,17] which are of importance if one deals with a SAM as such but of no importance if a SAM becomes a part of an organic electronics device. Whereas we have not specifically addressed the stability of the PPmP1-up/down and C10EC10-up/down SAMs on Ag(111), we could monitor this property on a time-scale of a week during the experiments at the synchrotron, requiring a prolonged storage of the samples and their handling under ambient conditions. No traces of degradation, including oxidation of the substrate, oxidation of the docking group, or the breakage of S−C bonds at the SAM-substrate interface were observed. This corresponds to our experience with an even more reactive substrate, GaAs, which could be effectively protected from oxidation and degradation as far as a high quality SAM had been formed.[180-181] Such a high quality and dense molecular packing are also characteristic for the PPmP1-up/down and C10EC10-up/down SAMs, so that a reasonable stability can be expected.

4.3 Tailor-Made SAMs with Embedded Dipoles

The results of the experiments for Ag(111) suggested that aromatic SAMs with the embedded pyrimidine group are more robust in terms of electrostatic interface engineering as compared to the aliphatic ones. In view of these favorable properties, we decided to optimize the SAM precursors with the embedded pyrimidine group.

The respective optimal precursors (PmP-up and PPm-down; see Figure 4.18) were synthesized by our partner group (Prof. A. Terfort and M. Gärtner; Frankfurt University). The substances were used as delivered.

In addition to my own experiments in the framework of this subproject, the films and bulk crystals of these molecules were also investigated by our partner group (Prof. A. Terfort, M. Gärtner, A. Wiesner, M. Kind and T. Abu Husein; Frankfurt University) using a variety of complementary techniques (X-ray diffraction analysis, ellipsometry, scanning tunneling microscopy, and infrared-reflection absorption spectroscopy). Further, device applications of these SAMs were tested by another partner group (Dr. B. Stadlober, Dr. A. Petritz, A. Fian, Dr. H. Gold, A. Cojocaru and E. Karner-Petritz; Joanneum Research, Weiz, Austria). Supplementary X-ray diffraction experiments on the evaporated organic semiconductor films were performed by Dr. Roland Resel (TU Graz, Austria). Finally, the experiments were supported by the density functional theory (DFT) calculations (Prof. E. Zojer and G. Nascimbeni; TU Graz, Austria) and device simulations (Dr. K. Zojer and M. Krammer; TU Graz, Austria).

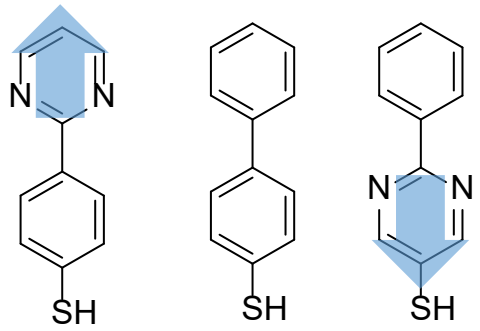

Figure 4.18: Structures of the SAM precursors used in the study of mixed monolayers, along with their abbreviations. The directions of the dipole moments of the dipolar groups with respect to the molecular backbone are marked by blue arrows. (the direction from the negative charge to the positive charge is considered as positive)

4.3.1 Wetting Properties

The wetting properties of the PmP-up, PPm-down, and PP SAMs are important in context of OSC growth on SAM-modified electrodes[183] and as a fingerprint of decoupling of the SAM-OSC (SAM/ambient) interface and the dipole engineering.

Advancing (θ_{adv}) and receding (θ_{rec}) water contact angles (WCA) for the PmP-up, PPm-down, and PP SAMs prepared are presented in Figure 4.19. Both θ_{adv} and θ_{rec} show similar values for the different monolayers, verifying the general assumption regarding the decoupling of the SAM-OSC (SAM/ambient) interface and the dipole engineering. There is, however, a weak, systematic dependence of WCA on the molecular dipole moment, which means the influence of the molecular dipole cannot be completely excluded within the given, two-ring molecular architecture.

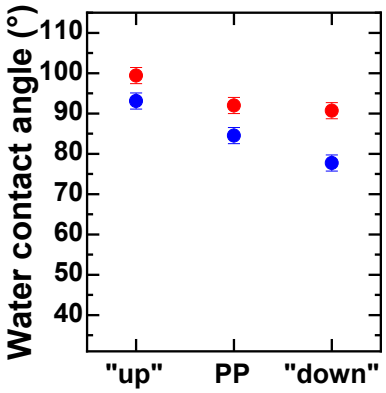

Figure 4.19: Advancing (red circles) and receding (blue circles) water contact angles for the PmP-up ("up"), PPm-down ("down"), and PP SAMs.

Note that the values for the WCA values for the reference PP SAMs are higher than the literature values of θ_{adv} and θ_{rec}, viz. 73° and 69°,[184] which implies its high quality. Note also that the WCA values for the reference PP SAMs prepared from THF are very close to those prepared from ethanol (not shown). On the one hand, this means, along with all other experimental data, that the properties of the PmP-up, PPm-down, and PP SAMs are not affected noticeably by the selection of the solvent, either THF or EtOH. On the other hands, it means indirectly that the values of the surface energy for the monolayers prepared from ethanol, including its dispersive and polar components,[183] are well applicable to the SAMs prepared from THF.

4.3.2 XPS and HRXPS

The S 2p, N 1s, and C 1s XPS spectra of the PmP-up, PPm-down, as well as the reference PP SAMs are presented in Figure 4.20.

The S 2p XPS spectra of all three films in Figure 4.20a exhibit a single S $2p_{3/2,1/2}$ doublet at ~162.0 eV (S $2p_{3/2}$). This BE is representative for the thiolate species bound to noble metal substrates,[170] indicative of the distinct SAM character of all films studied. The intensity of the doublet is similar over the series, being only slightly weaker for PmP-up, suggesting a similar packing density of all three SAMs. This tentative conclusion is also supported by the similar intensities of the Au 4f signal, relying on the attenuation by the SAM overlayer (not shown).

The N 1s XPS spectra of PmP-up and PPm-down are presented in Figure 4.20b. These spectra exhibit a single N 1s peak assigned to the nitrogen atoms in the pyrimidine ring of the SAM precursors, in contrast to the spectrum of PP which does not exhibit any signal, in accordance with the chemical composition. The BEs of the N 1s peak have, however, distinctly different BE position for the PPm-down and PmP-up SAMs, being 398.05 eV and 398.65 eV,

respectively. This difference cannot stem exclusively from the different screening of the photoemission hole by the substrate, resulting in a slightly lower N 1s BE value for PPm-down, since the respective effect is not particularly strong, and can be estimated as 0.05-0.1 eV in the given case.[171] Rather, it is a consequence of electrostatically induced XPS shifts.[22,23,25,185,186]

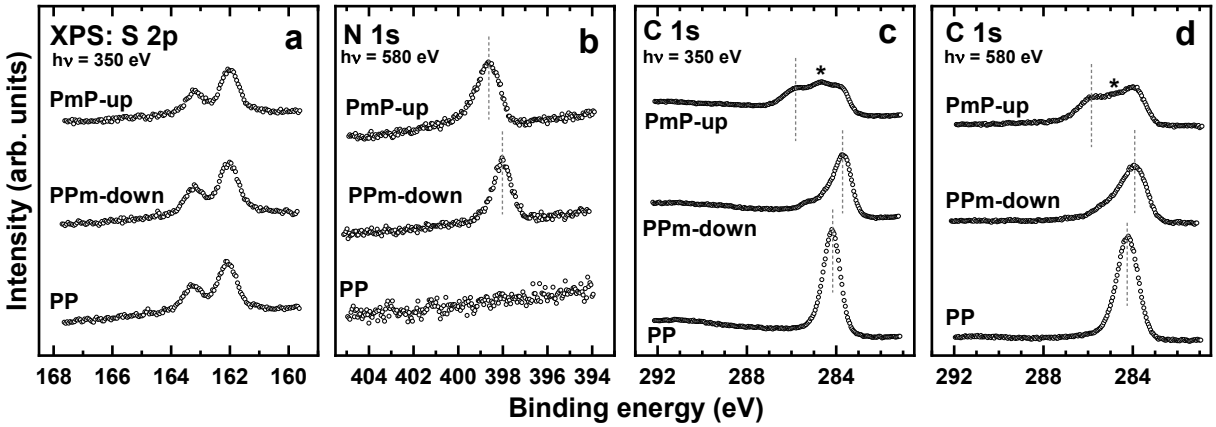

Figure 4.20: S 2p (a), N 1s (b), and C 1s (c, d) XPS spectra of the PmP-up, PPm-down, and PP reference SAMs. The spectra were acquired at photon energies of 350 eV (a, c) and 580 eV (b, d). The vertical dashed lines are to guide the eyes. A photon energy dependent feature appearing between the two major peaks in the spectrum of PmP-up is marked by *.

The C 1s XPS spectra of PmP-up and PPm-down are presented in Figures 4.20c and 4.20d. They are distinctly different and cannot be explained by a mere superposition of a pyrimidine and a phenylene spectra, relying on the chemical composition, which is identical for both systems. Rather, these spectra again are strongly influenced by the electrostatic effects in photoemission, associated with the dipole moment of the embedded pyrimidine moiety.[22,23,25,186] These effects will be discussed in detail later, when analyzing the electronic structure of the SAMs, relying on a comparison between our DFT simulations and literature data on related compounds.

Along with the qualitative analysis of the XPS data, their quantitative evaluation was performed, resulting in effective thicknesses of 9.3±0.04 nm and 10.0±0.04 nm for the PPm-down and PmP-up SAMs, respectively, and the same packing density of ~4.5×10^{14} molecules/cm^2 for both these monolayers. Significantly, the values for the PPm-down and PmP-up SAMs are close to those of PP (10.9 nm and 4.6×10^{14} molecules/cm^2, corresponding to the ($\sqrt{3}$x$\sqrt{3}$)R30° structure), which suggests a similar molecular packing. At the same time, they are slightly lower, indicating that the molecular packing is disturbed to some extent by the presence of the dipolar pyrimidine groups.

4.3.3 NEXAFS Spectroscopy

C and N K-edge NEXAFS data for the PmP-up and PPm-down SAMs are presented in Figures 4.21 and 4.22, respectively; the reference C K-edge data for PP are found in Figure A.1 (Appendix A). In Figures 4.21 and 4.22, two kinds of spectra are depicted. First, there are spectra acquired at an X-ray incidence angle of 55° (magical angle), which are representative

of the electronic structure of the films (unoccupied molecular orbitals) and are not affected by orientational effects.[131] Second, there are curves corresponding to the difference between the spectra collected under the normal (90°) and grazing (20°) incidence geometry. These curves are useful fingerprints of orientational order and molecular orientation,[131] showing the extent of the resonance intensity change upon variation of the angle between the electric field vector of the primary X-ray beam and the TDMs of the relevant molecular orbitals.

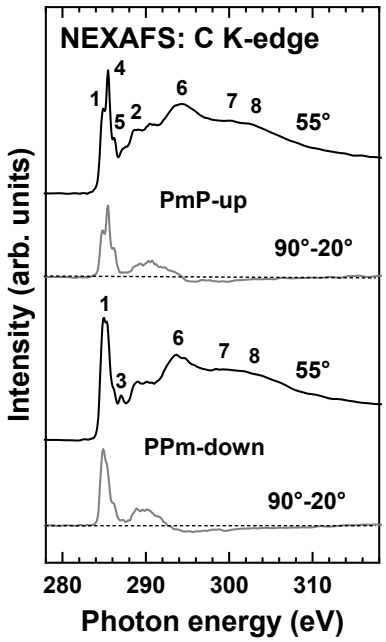

Figure 4.21: C K-edge NEXAFS spectra of the PmP-up and PPm-down SAMs acquired at an X-ray incidence angle of 55° (black lines), along with the respective difference between the spectra collected under the normal (90°) and grazing (20°) incidence geometry (gray lines). Individual absorption resonances are marked by numbers (see text for the assignments). The horizontal dashed lines correspond to zero.

Considering the 55° spectra, starting with the C K-edge ones, within the generally acceptable building block scheme in X-ray absorption spectroscopy,[131] the spectra of PmP-up and PPm-down can be understood as superpositions of the component spectra of phenyl and pyridine rings. Generally, the spectrum of phenyl and oligophenyl SAMs is dominated by the strong π_1* resonance at ~285.0 eV (**1**), accompanied by the respective π_2* peak (**2**) at ~288.8 eV and several broader σ* resonances (**6-8**) at higher excitation energies.[131,187,188,189] In addition, in oligophenyl SAMs a R*/C-S* resonance (**3**) at ~287.0 eV is frequently observed.[189] The spectrum of pyrimidine is dominated by a complex feature, with maxima at 284.7-285.1 eV (close to **1**; low intensity), 285.4 eV (**4**; high intensity), and 285.86 eV (**5**; high intensity), containing contributions from several π* resonances.[176,177] The spectrum exhibits also a variety of comparably weak π* and Rydberg resonances as well as broader σ* resonances at higher excitation energies.[176,177]

The above features are indeed observed in the 55° C K-edge NEXAFS spectra of PmP-up and PPm-down in Figure 4.21, with the weights modulated by the attenuation effects for the PEY signal[190] and a certain decrease in intensity of absorption resonances for the moieties located close to metal substrate.[189] Accordingly, the spectrum of PPm-down, having the phenyl ring in the top position and pyrimidine ring in the bottom position, is dominated by the features of phenyl, with just a "broadening" of the most intense π_1* resonance (**1**) due to the admixture of the pyrimidine resonances (**4**) and (**5**). In contrast, the spectrum of PmP-up, having the pyrimidine ring in the top position and phenyl ring in the bottom position, is dominated by the

pyrimidine resonances (**4**) and (**5**) forming a complex adsorption structure in the pre-edge region, with a contribution of the π_1* resonance (**1**) of the phenyl ring. At the same time, both for PPm-down and PmP-up, the post-edge region is dominated by the σ* resonances of phenyl (compare with the data for PP in Appendix A) which are generally more distinct than those of pyrimidine.

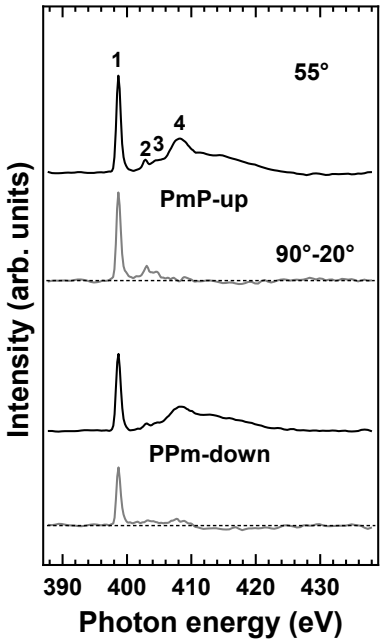

Figure 4.22: N K-edge NEXAFS spectra of the PmP-up and PPm-down SAMs acquired at an X-ray incidence angle of 55° (black lines), along with the respective difference between the spectra collected under the normal (90°) and grazing (20°) incidence geometry (gray lines). Individual absorption resonances are marked by numbers (see text for the assignments). The horizontal dashed lines correspond to zero.

The 55° N K-edge NEXAFS spectra of PPm-down and PmP-up in Figure 4.22 exhibit the characteristic features of pyrimidine.[176,177] The spectra are dominated by a strong π* resonance at ~398.5 eV (**1**) accompanied by a mixed π*-Rydberg feature at 402.7 eV (**2**) and Rydberg features at higher excitation energies (**3** and **4**). The intensity of the resonances is somewhat lower for PPm-down, which is related to the stronger attenuation of the PEY signal for the pyrimidine ring in the bottom position as well as to the slightly lower coverage as compared to PmP-up.

While the 55° NEXAFS spectra allow to verify the chemical identity of the PPm-down and PmP-up SAMs, the difference 90°-20° spectra in Figures 4.21 and 4.22 give insight into the molecular orientation in these films. In these spectra, pronounced difference peaks at the positions of the absorption resonances are observed, indicative of a high orientational order. Further, the peaks associated with the π* resonances are positive, whereas those related to the σ* resonances are negative. Considering that the TDMs of the π* and σ* orbitals are directed perpendicular and parallel to the ring planes, respectively, the signs of the difference peaks mean an upright molecular orientation in the SAMs, in qualitative agreement with the ellipsometry, IR spectroscopy, and XPS results.

In addition to the above-described qualitative analysis, a quantitative evaluation of the entire set of the NEXAFS data for PPm-down and PmP-up was performed, relying on the most prominent π* resonances at the C and N K-edge and using the standard theoretical framework for the vector-like orbitals, suitable in the given case.[131] Within the respective evaluation

procedure, the intensity of a particular π* resonance was derived from the spectra, plotted as a function of the X-ray incidence angle, and fitted by the theoretical curves for a vector-like orbital, with the average tilt angle of the π* orbital with respect to the surface normal, α, being the only parameter.[189,191] The derived values of this parameter for the C and N K-edge resonances are compiled in Table 4.1. The very similar values obtained evaluating the C and N K-edge resonances suggest that the molecular conformations are coplanar or close-to-coplanar in the SAMs, since the derived angles are predominantly (C K-edge) or exclusively (N K-edge) representative of the orientation of the phenyl and pyrimidine rings, respectively. Furthermore, it is consistent with the simulations discussed in the following section and with the very small, respectively, vanishing inter-ring torsions seen in the single crystal data.

Table 4.1: Average tilt angles of the π* orbitals in the PmP-up and PPm-down SAMs, calculated on the basis of the C K-edge and N K-edge NEXAFS data. The accuracy of the values is ±3°.

Monolayer	Tilt angle (α) from the C K-edge data	Tilt angle (α) from the N K-edge data	Average value
PmP-up	65.5°	69°	67.25°
PPm-down	66°	66°	66°

Based on the average tilt angles of the π* orbitals, average molecular tilt angles with respect to the surface normal, β, could be calculated using the equation, $\cos \alpha = \sin \beta \times \cos \gamma$ with γ being the molecular twist angle. The latter angle cannot be determined from the NEXAFS data (apart from a special derivatization of the molecules),[132] but can be taken, as a reasonable assumption, from bulk, IR or molecular simulation data. In the given case, relying on the latter data (see next section), taking agreement or disagreement of the experimental and theoretical values of α as a criterion for the reliability of the theoretical simulations. In the case of agreement, the β values from the molecular simulation data can be considered as characteristic of the SAMs studied.

4.3.4 Electronic Properties of the SAMs

The parallel alignment of the pyrimidine dipoles also causes a shift in the sample work function. This is shown for the PmP-up, PPm-down, and PP SAMs in Figure 4.23. Note that these values are very close to those obtained upon the preparation of these SAMs in ethanol,[183] being only slightly smaller. The comparable values suggests that the ability of the PmP-up and PPm-down films to manipulate charge carrier injection barriers in organic electronic devices does not depend significantly on the solvent applied for their preparation.

The work functions of PPm-down and PmP-up are higher (by +0.52 eV), respectively lower (by −0.37 eV) than for PP, in line with the orientation of the dipole moment of the embedded pyrimidine group. The observed WF shifts are very close to those observed for the previously reported, terphenylmethanethiol-based SAMs also containing a single pyrimidine unit per molecule, viz. +0.56 eV and −0.42 eV.[19] This can be tentatively explained by a somewhat

smaller molecular inclination in the latter SAMs, which results in a larger projection of the dipole moment onto the surface normal, defining the work function of the entire monolayer.

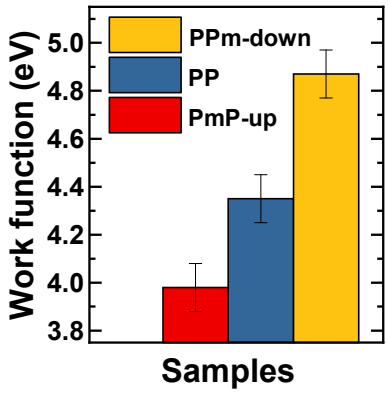

Figure 4.23: Work function values for the PmP-up, PPm-down, and PP SAMs prepared from THF measured with a Kelvin Probe.

The work function difference between PPm-down and PmP-up is ~0.9 eV, where we expect that the work function can be adjusted continuously within this range by mixing PPm-down and PmP-up molecules in a single SAM, as it has been demonstrated for a variety of different mixed SAMs[18,21,192-194] including those with embedded dipole.[20,26,195]

The experimental trend is confirmed by the simulations (see Appendix B) with a decrease of the work function for PmP-up and an increase for PPm-down (compared to the reference PP SAM). The absolute magnitude of the effect (±0.65) is, however, overestimated, which is in line with what we have observed for a variety of other systems, especially other pyrimidine containing compounds.[19] This is in part a consequence of assuming a densely packed, periodic structure in the simulations not accounting, for example, for disordered regions like grain boundaries, etc..[19]

4.3.5 Electrical Conductance

Besides the changes of the electrode work function, also the electrical conductance of the monolayer is a crucial parameter for the application of the SAMs as interfacial layers between the electrode and the active layer in organic electronics devices. Semi logarithmic current-density versus voltage plots for Au/SAM//EGaIn junctions with the PmP-up and PPm-down SAMs are presented in Figure 4.24. These values are lower by almost two orders of magnitude than those observed for the analogous terphenylmethanethiol-based molecules with embedded pyrimidine group.[178,183] This indicates a superior electric transport properties of the PmP-up and PPm-down monolayers, making these SAMs particularly promising for applications in organic electronics and photovoltaics devices. An interesting side aspect are quite close current values for the SAMs with the opposite directions of the dipole moment, in full agreement with the literature data for the analogous systems.[24,178] Note, however, that beyond this general behavior, some specific effects, such as dipole induced-dependence of the transition voltage and asymmetric conduction have been reported.[178,179]

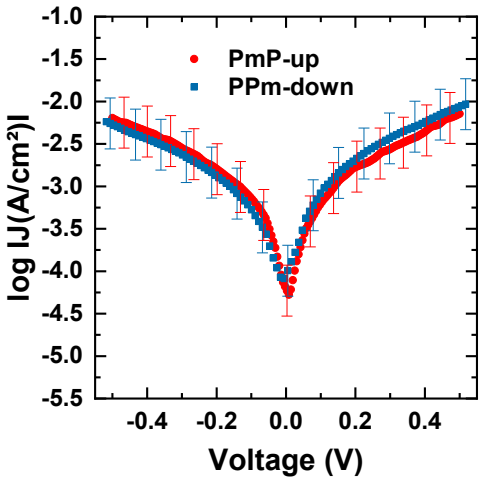

Figure 4.24: Semilogarithmic current-density versus voltage plots for Au/SAM//EGaIn junctions with the PmP-up (red circles) and PPm-down (blue squares) SAMs.[183]

4.3.6 Complementary Discussion

The results of the ellipsometry, XPS, Scanning Tunneling Microscope (STM), Infrared (IR) spectroscopy, and NEXAFS spectroscopy experiments and of the quantum mechanical simulations suggest that PPm-down and PmP-up form well-defined and densely packed SAMs on Au(111). The basic structural parameters of the PP, PPm-down, and PmP-up monolayers derived by these techniques are compiled in Table 4.2. The values obtained by the different techniques correlate well with each other, even though there is a certain scattering for individual parameters. The effective thicknesses and packing densities of the PP, PPm-down, and PmP-up SAMs are similar, suggesting similar molecular packing. The packing density values correlate well with the packing density of the $(\sqrt{3}\times\sqrt{3})R30°$ structure, which was indeed directly observed by STM (Figure B.1, Appendix B), even though the imaging was not easy and a certain polymorphism was recorded.

Table 4.2: Basic parameters of the PP, PmP-up, and PPm-down SAMs derived from the experimental data and theoretical simulations. The NEXAFS-derived tilt angles were calculated from the average values given in Table 4.2, assuming the twist angles from Table B.2 and the same tilt angles of both non-equivalent molecules in the unit cell. In the case of calculation, the tilt and twist angles for both non-equivalent molecules in the unit cell are given.

Monolayer	**Effective thickness [nm]**		**Packing density [molecules cm^{-2}]**	**Tilt angle [°]**				**Twist angle [°]**
Method	XPS	ellipsometry	XPS	ellipsometry	NEXAFS	IR	theory	theory
PP	1.09 ± 0.1	1.11 ± 0.02	4.6×10^{14}	26±10	19±3	n.d.	n.d.	n.d.
PmP-up	1.0 ± 0.1	1.10 ± 0.03	4.5×10^{14}	26±10	29.5±3	24 ± 11	29.6/25.6	60.2/7.7
PPm-down	0.93 ± 0.1	0.93 ± 0.02	4.5×10^{14}	41±10	31.5±3	14 ± 10	31.5/30.8	61.8/7.2

The molecular conformation in the PPm-down and PmP-up monolayers is essentially planar, as suggested by the bulk crystallography (Figures B.3 and B.4, Appendix B) and by the NEXAFS spectroscopy data and confirmed by DFT simulations (Figure B.5, Appendix B). These simulations favor a herringbone molecular arrangement (Figure B.5, Appendix B), which

requires a (3×√3)R30° unit cell, which however has the same packing density and is compatible with the (√3×√3)R30° structure. The simulations also shed light on the molecular orientation in the PPm-down, and PmP-up SAMs (Table B.2, Appendix B), with a very good agreement with the results of the NEXAFS spectroscopy (Table 4.2). The derived tilt angles appear to be more realistic than the noticeably lower values obtained from the IR data (Figure B.6 an Table B.7, Appendix B), which is presumably related to a low intensity of specific vibration modes used for the evaluation. Insights into the electronic structure of the SAMs could be gained from comparing calculated and measured XPS data (Figures 4.20 and B.8) and a good correlation between the KP data (Figure 4.23) and calculated electrostatic properties of the PPm-down and PmP-up SAMs could be achieved. The electric conductance of these monolayers was found to be comparably high (Figure 4.24) which is of a great advantage for their applications in organic electronics and photovoltaics. The potential of the PmP-up and PPm-down SAMs in organic electronics was illustrated by representative experimental data for the bottom gate, bottom contact organic field-effect transistors (OFETs) featuring SAM-modified source and drain gold electrodes (Figure B.9, Appendix B).

4.3.7 Mixed Monolayers

These spectra for the single-component PmP-up and PPm-down SAMs and reference PP monolayer are presented in Figure 4.25. All films, single-component and mixed monolayers suggest the formation of well-defined and contamination-free SAMs.

The spectrum of the latter film is typical for non-substituted aromatic thiolate SAMs, exhibiting a single peak stemming from the alkyl backbone at a BE of ~284.2 eV, as expected from the unsubstituted aromatic thiolate monolayer.

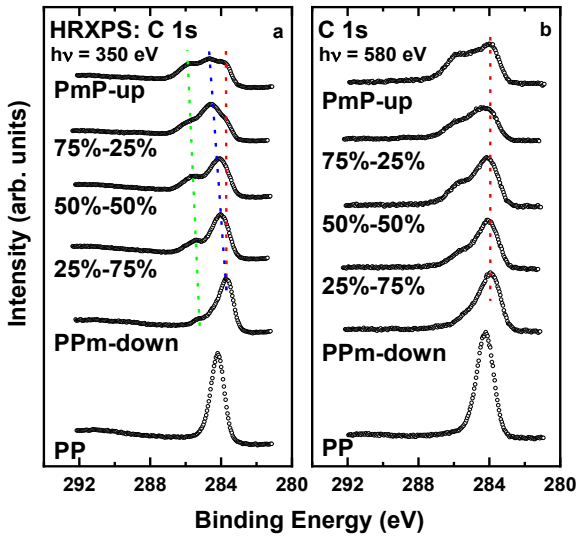

Figure 4.25: C 1s HRXPS spectra of the single-component and mixed PPm-down and PmP-up SAMs and PP (reference) SAMs acquired at a photon energy of 350 eV and 580 eV. The colored dashed lines are to guide the eyes.

The spectra presented in Figure 4.25b were acquired at a photon energy of 580 eV allowing to see more clearly the peak stemming from the bottom segment of the PPm-down and PmP-up SAMs – due to a moderate attenuation of the respective signal at the resulting kinetic energy at the photoelectrons. The electrostatic effects in the mixed SAMs can, however, be

better monitored using the spectra acquired at a lower photon energy since, due to strong attenuation of the photoelectron signal, they are almost exclusively representative of the top segment of the SAMs, reflecting the electrostatic effect of the embedded ester groups most clearly. Such spectra, collected at a photon energy of 350 eV of the single-component and mixed PPm-down and PmP-up SAMs, are presented in Figure 4.25.

The mixed PPm-down and PmP-up SAMs portray a fully consistent picture with the previous published PPmP-up and PPmP-down samples: (i) they show a continuous shift of the peak maximum with the mixing ratio; (ii) there are no traces of double-peak structure or spectra for the coexistence of large domains; (iii) additionally no peak broadening is observed in the mixed SAMs. Note that along with the dominant peak addressed above, the spectra in Figure 4.25 exhibit some further minor peaks. These are the features of the carbon atoms in the respective pyrimidine ring.[19] The contributions of these atoms should vary upon variation of the XPS sampling depth, as seen by the C 1s spectra of which show an intensity redistribution upon increase in the photon energy from 350 eV to 580 eV (larger sampling depth for the latter PE).

Similar to the aliphatic and terphenyl-4-methanethiol derived SAMs, the continuous change in the mid-SAM potential step, traced indirectly by the C 1s spectra, could be directly monitored by the measurement of the work function of the single-component and mixed PmP-up and PPm-down SAMs. The respective results are presented in Figure 4.26, measured in THF and EtOH as solvents.

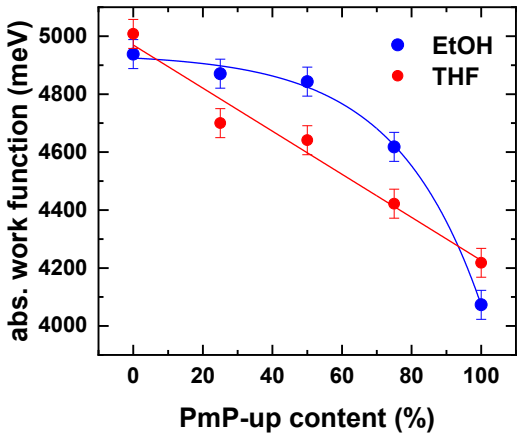

Figure 4.26: Dependence of the work function of the single-component and mixed PmP-up and PPm-down SAMs on the portion of PMP-up in the solutions, from which the SAMs were grown. The mixtures where prepared in tetrahydrofurane (THF, red circles) and ethanol (EtOH, blue circles) The character of this dependence is highlighted by colored lines.

In full agreement with the C 1s XPS data, the work function of the mixed SAMs in THF varies continuously and in a linear fashion between the ultimate values for the PmP-up monolayer (4.22 eV) and the PPm-down film (5.08 eV). Thus, the work function data support and evidence the conclusion that the solution composition is fully mimicked in the SAMs at the co-adsorption of the MP-up and MP-down precursors. On the other hand, from the mixtures adsorbed from ethanol a curved line is visible. This suggests a better solubility and adsorption of the PPm-down precursor in ethanol. In this case, the surface composition is heavily in favor of the PPm-down SAM, but still can be varied continuously and in controlled fashion in the ~0.9 eV range by mixed PmP-up and PPm-down monolayers, both in EtOH and THF.

4.4 Adjustment of the Work function by Electron irradiation

As an additional possibility for tuning the work function of SAMs, their modification by electron irradiation was chosen. Following the preliminary experiments, dealing with the response of the pyridine-substituted SAMs to electron irradiation, the most robust systems a non-substituted aromatic SAM (terphenylmethanethiol; TP1 (PPP1))[36,37,66-69,196] as well as TP1-derived monolayers (Figure 4.27) with the terminal pyridine group (PyPP1)[27] and embedded pyrimidine groups (PPmP1-up and PPmP1-down, Figure 1.1)[19,20] were investigated. Within further experiments, pyrimidine-substituted SAMs with a shorter pure heteroaromatic backbone, viz. PmPm-up and PmPm-down (Figure 4.27) were studied as well (the results are unpublished yet).

The SAM precursors were synthesized by our partner group (Prof. A. Terfort, and M. Gärtner; Frankfurt University). The substances were used as delivered.

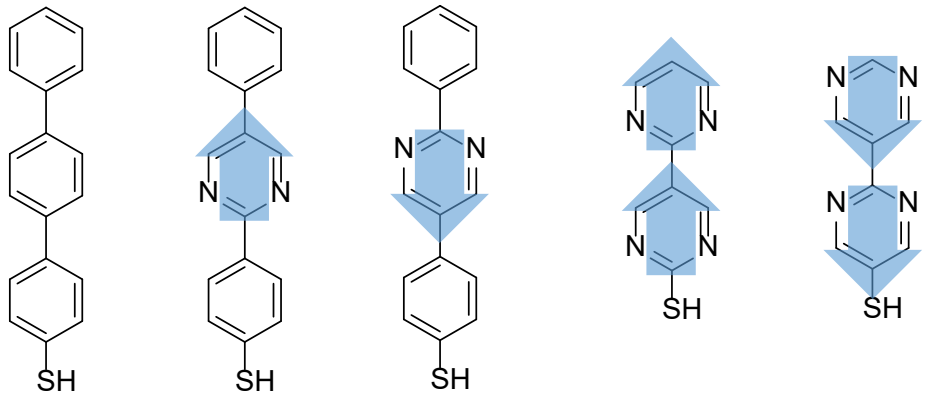

PPP1 **PPmP1-up** **PPmP1-down** **PmPm-up** **PmPm-down**

Figure 4.27: Structures of the SAM precursors used in the study of mixed monolayers, along with their abbreviations. The directions of the dipole moments of the dipolar groups with respect to the molecular backbone are marked by blue arrows. (the direction from the negative charge to the positive charge is considered as positive).

4.4.1 In Situ Measurements

Dependence of the WF of the PPP1, PyPP1, and PPmP1-up/down SAMs on irradiation dose is shown in Figure 4.28a. The measurements were performed in situ, immediately after the irradiation treatment. The WFs of the pristine PPP1, PPmP1-up/down SAMs was found to be 4.16 eV, 3.77 eV, and 4.86 eV, respectively, in good agreement with the experimental values from the previous work[19,20] and in reasonable correlation with the results of the DFT calculations for these molecular films.[19] The embedded pyrimidine groups shift the WF downward (PPmP1-up) or upward (PPmP1-down) as compared to the non-substituted film (PPP1), dependent on the direction of the respective dipole moment, which is in full agreement

with the results of the DFT calculations.[19] The terminal pyridine group with the dipole moment directed in the same way as for PPmP1-down provides an even larger shift as compared to the PPmP1-down case, resulting in a WF of ~5.20 eV for PyPP1, in a reasonable correlation with the literature data.[144] The dipole moments of the pyridine and pyrimidine moieties are similar (2.2 and 2.3 D, respectively)[197,198] but the electrostatic screening of the dipole imbedded into the molecular chain (PPmP1-down) within a densely packed SAM should be stronger than that at the SAM-ambient interface (PyPP1), which explains a larger WF shift in the latter case (with respect to the non-substituted film, PPP1).

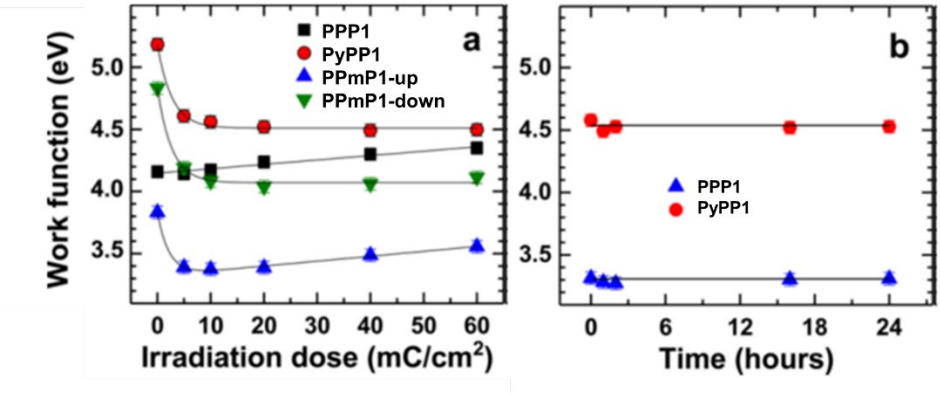

Figure 4.28: (a) Dependence of the WF of the PPP1, PyPP1, PPmP1-up, and PPmP1-down SAMs on irradiation dose. The measurements were performed in situ, directly after the irradiation treatment. (b) Dependence of the WF of the irradiated (10 mC/cm^2) PyPP1 and PPmP1-up SAMs on time. The samples were kept in vacuum without exposure to ambient. The legends are given in the panels.

Electron irradiation of the PPP1 SAM results in a slow and continuous increase of WF, which is in agreement with the literature data for analogous non-substituted aromatic monolayers.[199] The increase in WF, associated with combined effect of irradiation-induced cross-linking and a partial damage of the SAM-substrate interface,[199] is +0.03 eV at 10 mC/cm^2 and +0.19 eV at 60 mC/cm^2. In contrast, both pyridine and pyrimidine substituted SAMs exhibit not an increase but a drop in the WF, which occurs rapidly at low doses (up to 10 mC/cm^2) and is much more extensive, viz. -0.79 eV, -0.76 eV, and -0.41 eV for PyPP1, PPmP1-down, and PPmP1-up, respectively. Significantly, the irradiation-induced changes in WF are persistent as far as these samples are kept in vacuum, as demonstrated in Figure 4.28b where dependence of the WFs of the irradiated (10 mC/cm^2) PyPP1 and PPmP1-up SAMs on time is presented. The observed strong changes in the WF of the PyPP1, PPmP1-up, and PPmP1-down SAMs can only stem from irradiation-induced modification of pyridine and pyrimidine units. As shown in a previous publication dealing with several pyridine-terminated SAMs,[70] the pyridine moieties participate in the formation of the cross-linking network, exhibiting a simultaneous chemical modification and partial protonation. The analogous situation occurs for PPmP1-down and PPmP1-up as well. The laboratory C 1s, N 1s, and S 2p XPS spectra of the pristine and irradiated PPmP1-up SAMs are presented in Figure 4.29, representative of PPmP1-down as well. The C 1s and N 1s spectra of the pristine PPmP1-up film exhibit peaks characteristic of the molecular backbone,[19] whereas the S 2p spectrum shows a characteristic S 2$p_{3/2,1/2}$ doublet (**1**) at a BE position of ~162.0 eV (S 2$p_{3/2}$) corresponding to the thiolate species bound to noble metal substrates.[170] Specifically, the C 1s spectrum exhibits the characteristic component peaks associated with the bottom (**1**) and top (**2**) phenyl rings of the PPmP1-down backbone as well as an additional peak (**3**) assigned to the carbon atoms in the pyrimidine rings.[19] The difference in the binding energies of the peaks (**1**) and (**2**) stems from

the electrostatic shift provided by the embedded pyrimidine group.[19] The intensity of the C 1s signal in Figure 4.29a did not change noticeably upon irradiation, suggesting an extensive cross-linking in the SAM matrix,[70,200] but its character changes significantly already at low irradiation doses. The splitting of the peaks (**1**) and (**2**) becomes less pronounced at already 5 mC/cm^2 and is hardly perceptible at 10 mC/cm^2, suggesting a decrease or even elimination of the electrostatic shift associated with the embedded pyrimidine group (analogous effect for the inverse electrostatic shift was observed for PPmP1-down). The positions of the peaks (**1**) and (**2**) shift first to higher BE in the course of irradiation and then, after the merging of both peaks, the joint feature progressively shifts to lower BE.

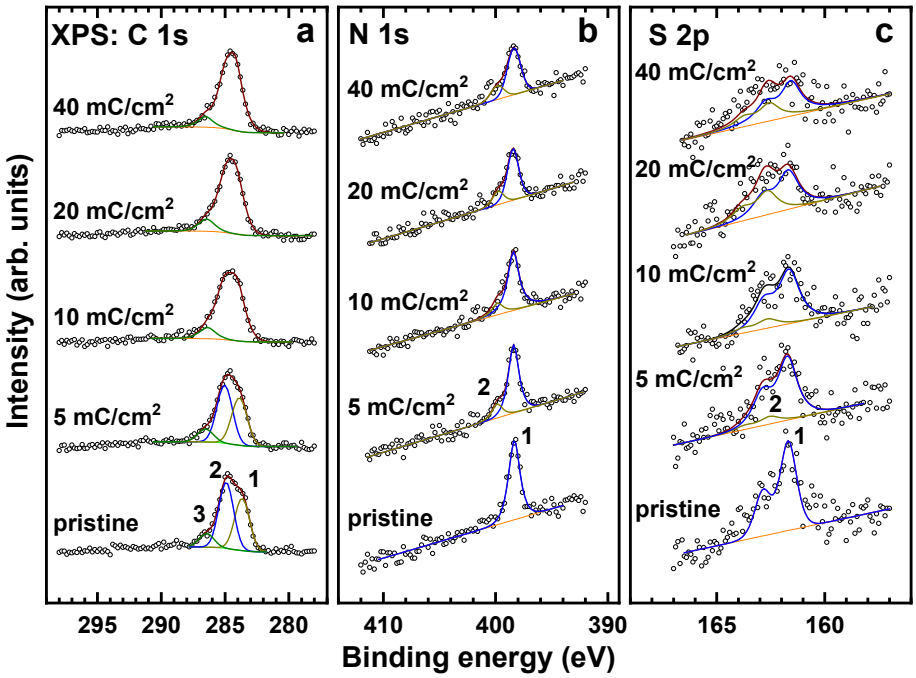

Figure 4.29: Laboratory C 1s (a), N 1s (b), and S 2p (c) XPS spectra of the pristine and irradiated PPmP1-up SAMs. The doses are marked at the respective spectra. The spectra are decomposed into the component peaks (a,b) or doublets (c) shown in different colors and marked by numbers. The sums of the individual components are drawn by the wine solid lines.

The N 1s spectra of PPmP1-up in Figure 4.29b exhibit several changes upon the irradiation. First, the intensity of the N 1s signal decreases to some extent suggesting a partial release of nitrogen-containing species. Second, the N 1s peak shifts and broadens, suggesting a modification and progressive heterogeneity of the pyrimidine-derived moieties in the monolayer. Third, a weak additional “shoulder” appears at the high BE side of the main peak; it can be assigned to a partial protonation of the pyrimidine-derived moieties, similar to the pyridine case.[70,201]

The S 2p spectra of PPmP1-up in Figure 4.29c exhibit the behavior typical of the homogeneous and heterogeneous aromatic SAMs,[70,200] viz. appearance and progressive increase in intensity of a new S 2p$_{3/2,1/2}$ doublet (**2**) at ~163.4 eV (S 2p$_{3/2}$) upon the irradiation, on the expense of the doublet stemming from the thiolate group. This suggests a partial damage of the SAM/substrate interface, which is a typical irradiation-induced process.[70,200] This damage occurs however much slower (with respect to the dose) and to a lesser extent as compared to alkanethiolate SAMs on the same substrate (see ref 61), suggesting an efficient cross-linking in the aromatic matrix.

The most important processes discussed above are additionally highlighted by the data presented in Figures 4.30 and 4.31. Figure 4.30a shows the thickness of the PPmP1-up SAM, which, similar to the intensity of the C 1s signal, did not change noticeably in the course of irradiation, apart from a very small decrease (~5%) at low irradiation doses. Figure 4.30b presents the total intensity of the N 1s signal, which decreased slowly in the course of irradiation, achieving a loss of 20-23% at high doses. Figure 4.30c presents the total intensity of the S 2p signal as well as intensities of both component doublets as functions of irradiation dose. The total intensity did not change noticeably in the course of irradiation, whereas the intensities of both component doublets show the opposite behavior, with progressive increase in the intensity of the irradiation-induced doublet on the expense of the thiolate one. Significantly, all changes highlighted in Figure 4.30 occur rather slow in the course of irradiation, exhibiting no correlation with the change in the WF (Figure 4.28).

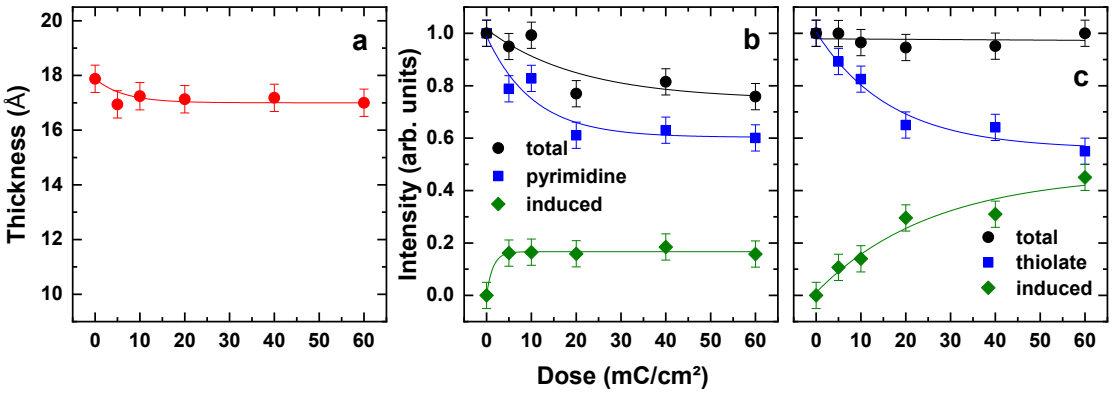

Figure 4.30: Dependence of the effective thickness (a) and XPS intensities (b,c) for the PPmP1-up SAM on irradiation dose. (b) Total intensity of the N 1s signal. (c) The total intensity of the S 2p signal as well as intensities of the S 2p component doublets corresponding to the pristine thiolate and irradiation-induced species. The experimental dependences are tentatively traced by solid curves shown in different colors, as guides for the eyes. The legends are given in the panels.

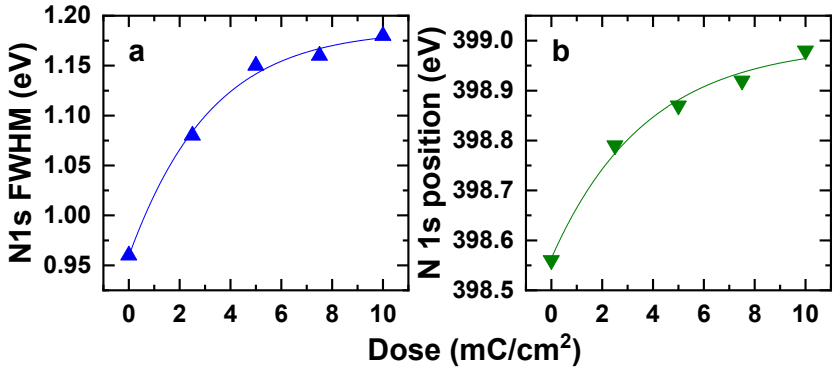

Figure 4.31: Dependence of the FWHM (a) and the BE position (b) of the N 1s peak for the PPmP1-up SAM on irradiation dose. The experimental dependences are tentatively tracked by exponential functions (solid curves).

The changes of the N 1s spectra were additionally monitored by the synchrotron-based XPS, taken the PPmP1-up SAM as a representative test system. The derived dependences of the BE position and FWHM of the N 1s peak for the PPmP1-up SAM on irradiation dose are presented in Figure 4.31. Both parameters exhibit progressive increase with the dose,

occurring in an exponential-like fashion, with a similar rate (with respect to the dose) as the WF change.

4.4.2 Ex Situ Measurements

The changes in the WF observed under the in situ conditions (Figure 4.28a) did not persist upon exposure of the irradiated SAMs to ambient. This effect is illustrated by Figure 4.32 where the WFs of the pristine SAMs of this study are compared with those of the irradiated (10 mC/cm^2) films for both in situ case and after the exposure of the irradiated SAMs to ambient.

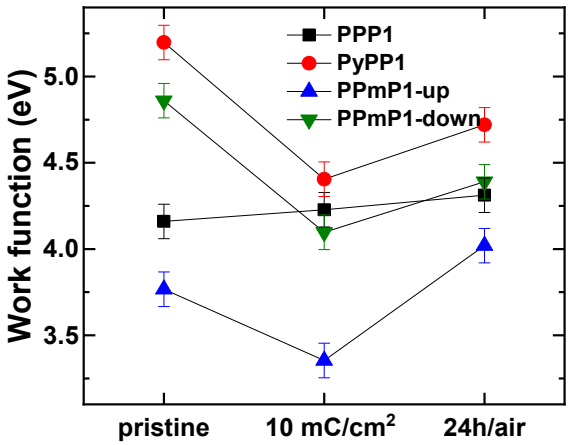

Figure 4.32: WF of the pristine and irradiated (10 mC/cm^2) PPP1, PyPP1, PPmP1-up, and PPmP1-down SAMs. The WF was either measured in situ, immediately after the irradiation treatment, or after exposure to ambient. The legend is given in the figure.

Whereas the WF of the reference, non-substituted SAM (PPmP1) exhibited only a slight increase (~0.09 eV) upon the exposure to ambient, those of the pyridine-terminated (PyPP1) and pyrimidine-substituted (PPmP1-up/down) monolayers showed a much more noticeable increase, partly compensating (PyPP1 and PPmP1-down) or even overcompensating (PPmP1-up) the effect of irradiation. The resulting changes in the WF as compared to the pristine SAMs were estimated at +0.17 eV, −0.48 eV, −0.47 eV, and +0.25 eV for the PPP1, PyPP1, PPmP1-down, and PPmP1-up films, respectively.

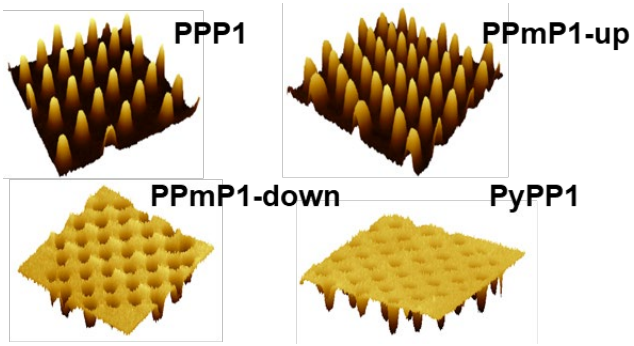

Figure 4.33: Surface potential images (3D representation) of e-beam patterned PPP1, PyPP1, PPmP1-up and PPmP1-down SAMs. The dose was set to 10 mC/cm^2. The imaging was performed ex situ, after exposure to ambient.

These changes could be directly visualized by the WF patterns prepared in proximity printing geometry. Surface potential images of such patterns are presented in Figure 4.33. In accordance with the WF measurements on the homogeneously irradiated samples, the PPP1 and PPmP1-up patterns exhibit a higher WF within the irradiated areas, whereas the inverse situation occurs for the PyPP1 and PPmP1-down patterns.

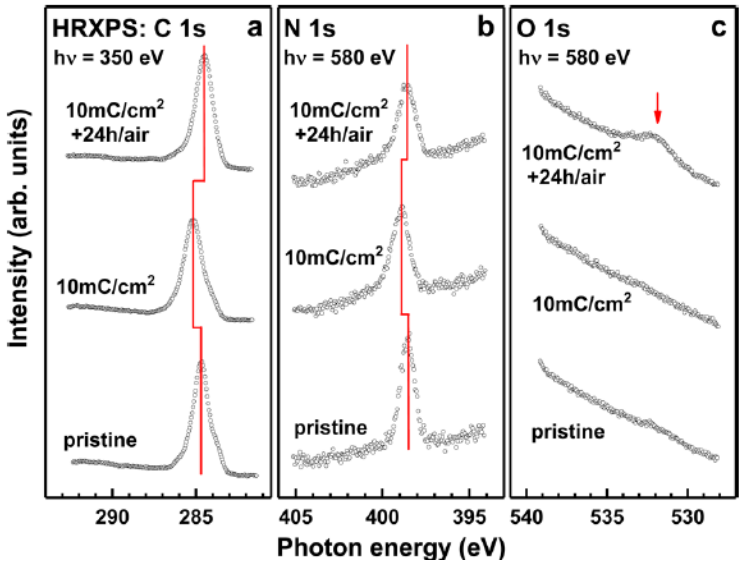

Figure 4.34: Synchrotron-based C 1s (a), N 1s (b), and O 1s (c) XPS spectra of the pristine and irradiated (10 mC/cm^2) PPmP1-up SAMs before and after exposure to ambient. The legends are marked at the respective spectra. The positions of the main peaks are highlighted by vertical red lines (a,b); the O 1s peak (c), appearing after the exposure to ambient, is highlighted by the red arrow.

Possible chemical changes of the irradiated SAMs upon their exposure to ambient were monitored by XPS and AFM. As a representative example, synchrotron based C 1s, N 1s, and O 1s spectra of the pristine and irradiated (10 mC/cm^2) PPmP1-up SAMs before and after exposure to ambient are shown in Figure 4.34. The C 1s and N 1s peaks, shifted to the higher BEs upon irradiation with the given dose, exhibited pronounced downward shifts upon exposure to ambient (Figure 4.34a,b, respectively), suggesting certain chemical changes or/and electrostatic “recharging” induced by this exposure. In addition, the intensity of the C 1s

signal increased slightly upon the exposure, accompanied by the appearance of a pronounced O 1s signal (Figure 4.34c), which was completely absent in the spectra of the pristine and irradiated films, as far as they were kept in vacuum. This behaviour suggests adsorption of carbon and oxygen-containing airborne species, which is in accordance with previous observation.[61,199] This effect is illustrated by Figure 4.35 where a representative morphology image of a PPmP1-up SAM pattern along with the height profile across the “written” dotlike features are presented. The reason for this effect is presumably chemical activation of the SAM-ambient interface, which is a side effect in the given case but can be useful as well, for example, for in situ electron-beam induced deposition of a predefined material.[202,203]

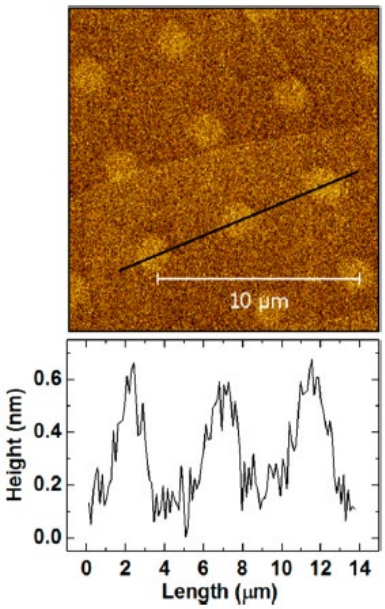

Figure 4.35: A representative morphology image of a PPmP1-up SAM pattern (a) along with the height profile across the “written” dot-like features (b). The patterning was performed in proximity printing geometry. The dose was set to 10 mC/cm^2.

4.4.3 Possible Reasons for the Observed Behavior

Upon electron irradiation, the PyPP1, PPmP1-up, and PPmP1-down SAMs exhibit behavior similar to that of oligophenyl-based films, such as the PPP1 monolayer, viz. a progressive and extensive cross-linking, involving also the pyridine and pyrimidine moieties; this process prevents release of individual molecules and their fragments and slows down the damage of the SAM/substrate interface. At the same time, the PyPP1, PPmP1-up, and PPmP1-down SAMs exhibit distinctly different changes in the WF upon electron irradiation as compared to the reference PPP1 film. These changes can only be related to the specific behavior of the pyridine and pyrimidine moieties, superimposing onto the change in WF associated with the oligophenyl backbone, which is represented by the example of the reference PPP1 film.

The WF changes associated with the pyridine and pyrimidine moieties can be related to an interplay of several different effects. First, as shown by the XPS data, the electrostatic shifts associated with the terminal pyridine and midchain pyrimidine groups are partly eliminated due to their modification and intermolecular cross-linking. Theoretically, complete elimination of the electrostatic shifts should result in the WF values similar to that of the non-substituted SAM

and be persistent upon the exposure to ambient, which both are not the case (see Figures 4.28 and 4.32). In particular, the WF of PPmP1-up did not increase toward the PPP1 values but decrease upon electron irradiation. This suggests that there is another contribution, general for the PyPP1, PPmP1-up, and PPmP1-down SAMs and lowering the WF of these systems upon electron irradiation. This contribution works in the same direction as the elimination of the electrostatic shift (see above) for PyPP1 and PPmP1-down but in the opposite direction for PPmP1-up. Consequently, the ultimate change in the WF for the latter system is noticeably smaller than that for the former films, viz. −0.41 eV versus −(0.76−0.79) eV; see Figure 4.28a.

Significantly, the WF-lowering contribution is mostly eliminated upon the exposure of the PyPP1, PPmP1-up, and PPmP1-down SAMs to ambient, manifested by the similar increase in the WF for all these films (Figure 4.32). This effect cannot be solely related to the adsorption of the airborne species since the increase in the WF is much smaller for PPP1, which has the same chemical composition of the SAM/ambient interface as the PPP1-up and PPmP1-down monolayers. Regretfully, the XPS data do not give any other hint except for clear signatures of air exposure-induced chemical changes, electrostatic "recharging", and adsorption of airborne species (Figures 4.34 and 4.35), so that the only possibility is a reasonable assumption. One possible mechanism, which might be responsible for the observed WF behavior, is illustrated in Figure 4.36a.

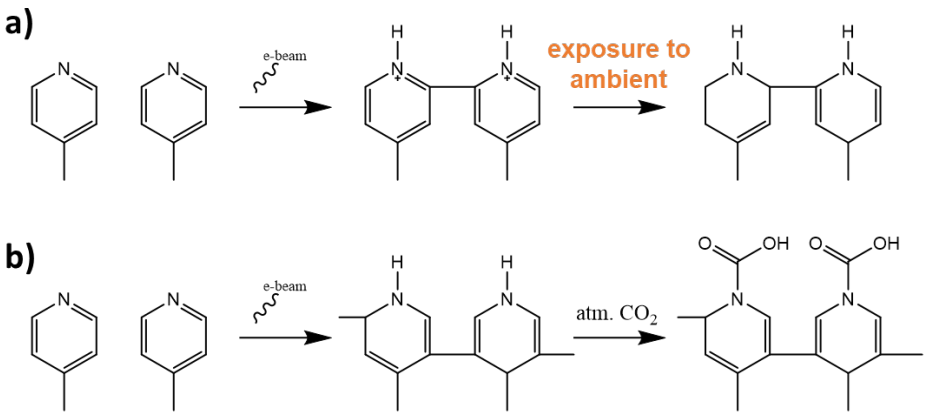

Figure 4.36: Proposed models of irradiation-induced modification of the pyridine group in the PyPP1 SAM, representative of the embedded pyrimidine groups of the PPmP1-up and PPmP1-down monolayers as well: (a) formation of positively charged pyridinium or pyrimidinium moieties (in situ) and their subsequent "recharging" (ex situ); (b) formation of amine (in situ) and carbamate (ex situ) groups.

The "driving force" of this mechanism are hydrogen atoms released upon irradiation-induced cleavage of C−H bonds in the heteroaromatic backbones, which is the primary process triggering the cross-linking.[43,61,63,64,66,200] The released hydrogen atoms are chemically active, in particular, with respect to nitrogen, inducing, for example, nitro-to-amino and nitrile-to amino transformations in the nitro- and nitrile-terminated aromatic SAMs.[44,58,204] Consequently, they can also trigger specific chemical reactions involving the pyridine and pyrimidine groups in the PyPP1, PPmP1-up, and PPmP1-down SAMs, resulting, in particular, in formation of positively charged pyridinium or pyrimidinium moieties capable to decrease the WF of these films. These moieties remain stable as long as the film is kept in vacuum but undergone further chemical reactions, resulting in disappearance of the positive charge, upon the exposure of the irradiated films to ambient.

An alternative mechanism, involving the released hydrogen atoms as well, is presented in Figure 4.36b. Accordingly, the reactive hydrogen atoms reduce (some of) the heterocycles to the respective amines, with the nitrogen atoms becoming less electron-withdrawing, so that the WF is lowered. Further, upon the exposure to ambient these amines react with airborne CO_2 and form carbamates, which results in the WF increase due to the electron-withdrawing character of the carbonyl groups.

Regretfully, the available spectroscopic data do not provide a clear evidence in favor of one of the above mechanisms, letting other possibilities open as well. At the same time, these data suggest chemical transformation of the pyridine and pyrimidine moieties upon electron irradiation with certain heterogeneity of the resulting chemical structures. A pronounced positive BE shift of both C 1s and N 1s XPS peaks occurring at low irradiation doses (Figure 4.34) correlates with our assumption about the appearance of positively charged (Figure 4.36a) or WF lowering (Figure 4.36b) species in the irradiated SAMs. Significantly, this shift is reversed upon the exposure of the films to ambient, manifesting elimination of the positive charge (Figure 4.36a) or a transformation of the WF lowering moieties (Figure 4.36b), which is in full agreement with the WF behavior (Figure 4.32).

Apart from the pure scientific issues discussed above, practical implications of the results should be considered. The major advantages of the presented electron irradiation approach are (i) the possibility of precise tuning of the WF within the given dynamical range by selection of a proper dose and, as already mentioned, (ii) the possibility to apply e-beam lithography for WF patterning. The latter is demonstrated in Figure 4.33 where representative examples of such patterns are presented. Consequently, e-beam lithography, which also has the advantages of a flexible form of the written features as well as dose variation across the pattern,[205] can be a valuable alternative to other approaches to WF patterning such as microcontact printing.[72,206,207] Significantly, the dynamic range of the in situ variation of the WF covered by the PyPP1, PPmP1- up, and PPmP1-down SAMs is exceptionally large, viz. from +5.2 to +3.4 eV, with a small gap around +4.0 eV, between the minimal value for PPmP1-up and the maximal value for PPmP1-down (Figure 4.28a), which, however, can be covered by a proper mixed SAM of both these constituents.[200] Consequently, a suitable SAM can be easily selected for a specific application and its WF subsequently fine-tuned or patterned within its specific dynamical range (Figure 4.28a). Regretfully, the SAM specific dynamical ranges as well as the joint dynamical range of the entire SAM series decrease noticeably upon the exposure of the monolayers to ambient (Figure 4.32), necessary, in most cases, for their integration into the devices. One cannot exclude, however, that the in situ WF values of the pyridine- and pyrimidine-substituted SAMs remain persistent and valid if the subsequent fabrication steps, such as deposition of an organic semiconductor, are performed without the exposure to ambient, for example, in the same vacuum chamber or under inert atmosphere, as it, for example, occurred for UV/ozone treated Au.[208] This can be a subject of further research in context of the results presented in the given work.

4.4.4 Electron Irradiation of Bipyrimidine SAMs

The laboratory C 1s, N 1s, and S 2p XPS spectra of the pristine and irradiated PmPm-down SAMs are presented in Figure 4.37, representative for PmPm-up as well. The C 1s and N 1s spectra of the pristine PmPm-down film exhibit peaks characteristics for the molecular backbone,[43] whereas the S 2p spectrum shows a characteristic S $2p_{3/2,1/2}$ doublet (1) at a BE

position of 162.0 eV (S $2p_{3/2}$), corresponding to the thiolate species bound to noble metal substrates.[103] The intensity of the C 1s signal, shown in Figure 4.37a, did not change much upon irradiation. Due to this fact, there is only a small loss in effective thickness of ~20%, suggesting an extensive cross-linking in the SAM matrix, similar to the previous case.

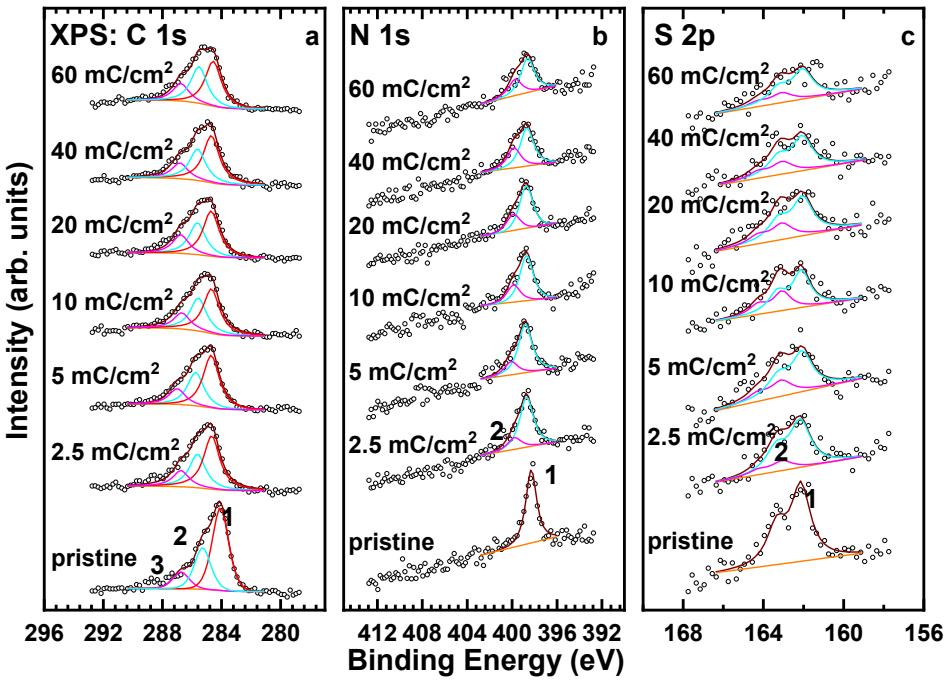

Figure 4.37: Laboratory C 1s (a), N 1s (b), and S 2p (c) XPS spectra of the pristine and irradiated PmPm-down SAMs. The doses are marked at the respective spectra. The spectra are decomposed into the component peaks (a,b) or doublets (c) shown in different colors and marked by numbers. The sums of the individual components are drawn by the wine solid lines.

The dependence of the WF of the PmPm-up, and PmPm-down SAMs on irradiation dose is shown in Figure 4.38a. The measurements were performed in situ immediately after the irradiation treatment. The values were found to be 4.18 eV, and 5.04 eV respectively. The embedded pyrimidine groups shift the WF downward (PmPm-up) or upward (PmPm-down) as compared to the non-substituted film (BPT, 4.42 eV), dependent on the direction of the respective dipole moment, which is in full agreement with previous work.[209]

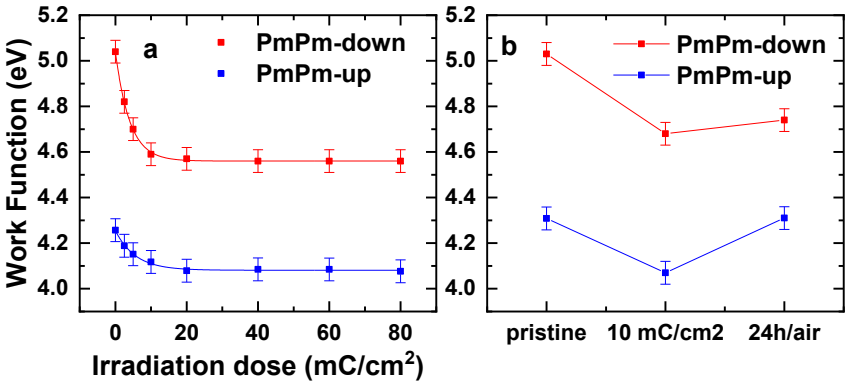

Figure 4.38: (a) Dependence of the WF of the PmPm-up and PmPm-down SAMs on irradiation dose. The measurements were performed in situ, directly after the irradiation treatment. (b) WF of the pristine and irradiated (10 mC/cm^2) PmPm-up, and PmPm-down SAMs. The WF was either measured in situ, immediately after the irradiation treatment, or after exposure to ambient. The legend is given in the Figure.

Both double pyrimidine substituted SAMs exhibit not an increase but a drop in the WF, which occurs already at low doses (up to 10 mC/cm^2), –0.45 eV, and –0.51 eV for PmPm-down, and PmPm-up, respectively. Note that these changes are less pronounced compared to the already mentioned PPmP-up and PPmP-down system, but also in agreement with the previously results for irradiation-induced changes in WF.

The changes in WF observed under the in situ conditions (Figure 4.38a) did not persist upon exposure of the irradiated SAMs to ambient. This effect is illustrated by Figure 4.39b where the WFs of the pristine SAMs of this study are compared with those of the irradiated (10 mC/cm^2) films for both in situ case and after the exposure of the irradiated SAMs to ambient. The work functions of the pyrimidine-substituted (PmPm-up and PmPm-down) monolayers showed a slight increase, partly compensating (PmPm-down) or even reversing (PmPm-up) the effect of the irradiation. The resulting changes in the WF as compared to the pristine SAMs were estimated at +0.06 eV, and +0.24 eV for the PmPm-down, and PmPm-up films, respectively.

4.5 DTC-based SAMs

Alternatively to the embedding of a dipolar group into the molecular backbone, selection of a specific anchoring motif was tried in context of interfacial dipole engineering, taking dithiocarbamate-based SAMs as a representative example. To get a deeper understanding of the electronic properties of the DTC SAMs, the primary focus in this part of my work was put on the two most basic systems, namely, phenyl-piperidine-DTC (PPd) and phenyl-piperazine-DTC (PPz) SAMs on Au(111). These monolayers represent highly suitable model systems, which were specifically designed to address the specific properties of the piperidine-DTC and piperazine-DTC docking platforms. The terminal phenyl ring of both molecules is a non-polar and well-defined structural unit, supporting the formation of ordered SAMs. Several other representative DTC derivatives were studied as well; they were derived from the PPd and PPz basic systems by simple substitution of the phenyl ring in the para position or by its fluorination.

The DTC-based precursors (Figure 4.39) were synthesized by our partner groups (Prof. Dr. S. Ludwigs and D. Treftz; Stuttgart University and Dr. F. von Wrochem, Sony Deutschland GmbH, Stuttgart). The substances were used as delivered. Dr. F. von Wrochem has also performed complementary XPS and UPS experiments.

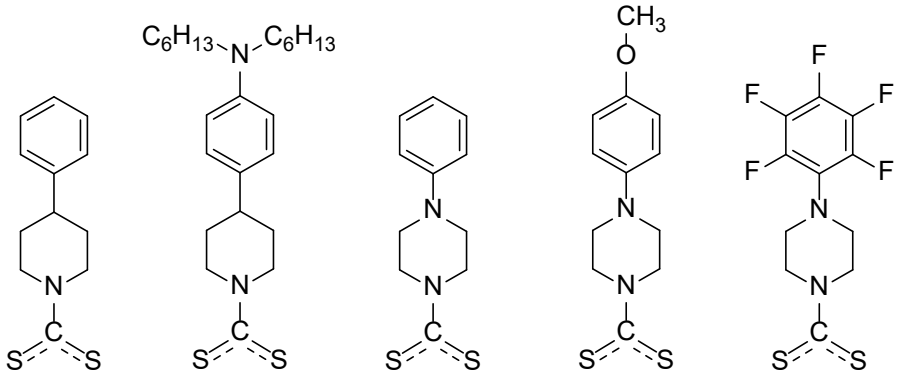

Figure 4.39: Schematic structures of the DTC-based SAM constituents used for in this study along with the respective abbreviations.

4.5.1 XPS and HRXPS

The S 2p, C 1s, and N 1s XPS spectra of the DTC-based SAMs are presented in Figure 4.40. The S 2p spectra of all films exhibit a single S $2p_{3/2,1/2}$ doublet at a BE position of 161.82-161.85 eV (S $2p_{3/2}$), as previously shown for dithiocarbamates in general[210] and for the C12N-PPd, OMe-PPz, and FP-Pz monolayers in particular.[12] Significantly, the BE of this doublet is by ~0.15 eV lower than the characteristic value for thiolate species bound to noble metal surfaces (162.0±0.05 eV),[170] in agreement with earlier observations.[210] This suggests a higher negative partial charge on the S atoms compared to the thiolate sulfur, indeed validated by basic considerations based on DTC resonance hybrid structures (stronger

donating character of the amine group coordinated to the CS_2 unit). In this sense, the lower BE of the S 2p doublet as compared to thiolate does not necessarily mean that each of the sulfur atoms in the DTC moiety is bound stronger to the substrate than in the thiolate. This is, however, the case for the entire DTC moiety, as demonstrated by thermal stability experiments in which the desorption peak of *n*-butanethiol assembled on Au(111) was observed at noticeably lower temperature (380±10 K) than that of a test DTC compound (470±10 K).[210] Also, the occurrence of just a single doublet at a BE of ~161.85 eV is significant, as it serves as a direct evidence for the formation of SAMs with chemically homogeneous bonding to the substrate. This contrasts positively the situation encountered usually for thiol- and thioether-based ligands with multiple attachment points, where the formation of a variety of different chemical species such as thiolates, atomic sulfur, unbound sulfur, etc. is commonly observed (based on core level shifts in their S $2p_{3/2}$ signal).[211-214] The bonding of the DTC-based SAMs to the substrate in a "thiolate-like fashion" also provides a good chemical link. This is an advantage for efficient charge transport, which is important in the context of organic and molecular electronics applications. Since the spacing between both S atoms in the DTC group (~2.96 Å) does not fit the periodicity of the Au(111) template, multiple adsorption sites can be expected. This is indeed implied by the rather high value for the FWHM of the S $2p_{3/2,1/2}$ components for the DTC-based SAMs, viz. 0.73-0.93 eV compared to dodecanthiolate monolayers measured at analogous conditions, viz. 0.54-0.59 eV.[170]

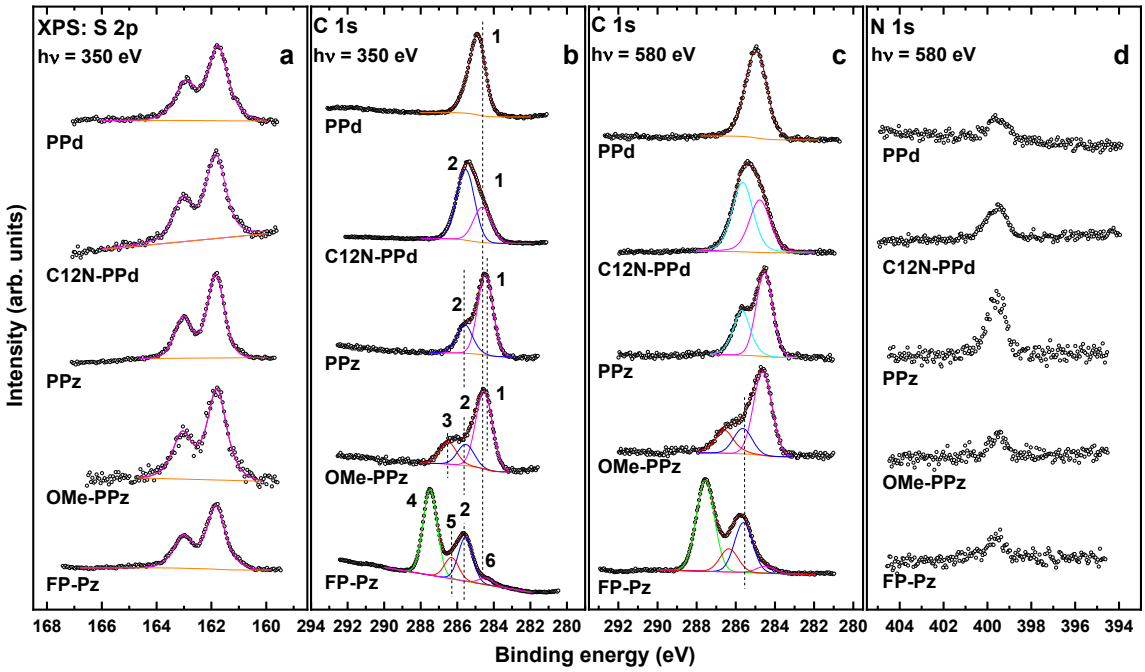

Figure 4.40: S 2p (a), C 1s (b, c), and N 1s (d) XPS spectra of the DTC-based SAMs. The spectra were acquired at photon energies of 350 eV (S 2p and C 1s in panel b) and 580 eV (C 1s in panel c and N 1s). The S 2p spectra are fitted by a single S $2p_{3/2,1/2}$ doublet. The C 1s spectra, normalized to the peak height, are decomposed into individual component peaks shown in different colors and marked by numbers, separately for the PPd and PPz related films; see text for details. The vertical dashed lines are guides to the eyes.

Interestingly, the FWHM value for the PPz SAMs (0.73 eV) is somewhat smaller than that for its derivatives, OMe-PPz, and FP-Pz (0.84 eV and 0.80 eV, respectively). This suggests an even larger heterogeneity of the adsorption sites (configurations) in the latter cases. The same

applies to the PPd and C12N-PPd monolayers, although here the difference (0.89 eV vs. 0.93 eV) is somewhat smaller.

The C 1s spectra of the DTC-based SAMs in Figures 4.40b and 4.40c can be decomposed into several component peaks denoted by numbers in the plot. The assignment of these peaks to specific functional groups and specific C atoms is based on electronegativity considerations,[12] the comparison to spectra of systems containing similar building blocks, and the analysis of the spectra acquired at different photon energies. The latter is particularly useful considering the stronger contribution of the buried species at higher excitation energy (580 eV vs. 350 eV).

The C 1s spectrum of the PPd SAM exhibits only one, almost symmetric peak at ~284.9 eV (**1**) originating from a superposition of core-level excitations of the terminal phenyl ring and the piperidine moiety. A signal associated with the DTC carbon, expected at a significantly higher BE is not perceptible because of its strong attenuation. Similarly, the signal of the two C atoms in the bottom ring bonded to N, which should also appear at higher BE, is not clearly resolved and is presumably hidden in the high BE tail of the main peak. The joint contribution of the phenyl ring and piperidine can also be identified upon decomposition of the asymmetric peak observed in the C 1s spectra of the C12N-PPd SAM into two component peaks. The low BE component peak at ~284.7 eV (**1**) is then assigned to the same C atoms as the sole peak in PPd, while the high BE component at 285.4 eV (**2**) is ascribed to the terminal aliphatic chains. The intensity of this peak is comparably higher since the signal from the phenyl ring and piperidine is more strongly attenuated. This is also the case for the signal stemming from the C atoms bound to the uppermost N atom.

The spectra of the PPz SAM exhibit two peaks at 285.5 eV (**2**) and 284.5 eV (**1**), according to the fits. They are assigned to the C atoms bonded to N atoms (all atoms in the piperazine ring and the lowest atom in the phenyl ring) (**2**) and to all other C atoms in the terminal phenyl ring (**1**), respectively. The above two components can also be identified in the spectra of the OMe-PPz film, where they are accompanied by an additional peak at 286.5 eV (**3**), which originates from the carbon atom in the terminal OCH_3 group. Finally, the piperazine component peak (**2**) is clearly resolved also in the spectra of the FP-Pz monolayer. The dominant component in these spectra is, however, the peak at 287.5 eV (**4**), which is related to the fluorine-bonded carbon atoms in the terminal ring. In addition, a low intensity component peak at 286.3 eV (**5**) can be identified upon spectral decomposition. This peak can be tentatively associated with the carbon atom of the upper ring, which is directly bonded to the piperazine but is also somewhat affected by the F atoms in the vicinity. Finally, there is a low BE shoulder at 284.3 eV (**6**) which cannot be assigned to any functional group of FP-Pz and, most likely, stems from contaminations.

The N 1s spectra of all DTC-based SAMs in Figure 4.40d exhibit a single peak at ~399.5 eV assigned to the nitrogen atoms in the piperazine and piperidine rings as well as to the nitrogen atom in the terminal dihexylamine group of the C12N-PPD film. The relative intensities of N 1s peaks correlate coarsely with the amount of the nitrogen atoms and their locations within the molecular backbone (affecting the attenuation of the respective signal). The F 1s spectrum of the FP-Pz monolayer (not shown) acquired at a photon energy of 720 eV exhibits a single peak at ~687.9 eV, assigned to the fluorine atoms in the terminal ring.

The quantitative evaluation of the XPS spectra results in the values for the effective thicknesses and packing densities of the DTC-based SAMs compiled in Table 4.3. The effective thicknesses of the monolayers are close to the sum of the respective molecular lengths and the length of the S−Au bond, suggesting an upright molecular orientation. The

packing densities of the parent PPd and PPz films are very close to the value characteristic of the densely packed (2√3×√3)R30° structure typical of non-substituted alkanethiolate SAMs on Au(111), viz. 4.63×10^{14} mol/cm^2.[104,215] In view of the almost double density of the sulfur atoms in the DTC case, the similarity of the packing densities is a direct indication that the packing is mostly determined by the interaction between the molecular backbones. It also implies that the docking groups in conventional thiolate SAMs, with only one S atom per molecular chain, are comparably loosely packed. An important implication of this finding is that the presence of atomic sulfur, which is frequently observed in thiolate SAMs as a minor contamination,[170] does not necessarily indicate a poor or limited quality of the monolayers, since, apparently, the respective species can very likely coexist with the intact thiolate anchors, packed in the standard fashion, without much interference.

Table 4.3: Effective thickness (Å), packing density (molecules/cm^2), and relative density of the DTC-based SAMs. The experimental errors are ±1−1.5 Å for the thickness and ±10% for the packing density. The reference packing density for a dodecanethiol SAM (√3×√3 structure) is 4.63×10^{14} molecules/cm^2.table

Monolayer	PPd	C12N-PPd	PPz	OMe-PPz	FP-Pz
Thickness (Å)	9.9	13.3	10.8	11.9	13.1
Packing density (molecules/cm^2)	4.25×10^{14}	3.5×10^{14}	4.65×10^{14}	3.4×10^{14}	2.75×10^{14}
Relative density	0.92	0.76	1.0	0.74	0.59

The packing densities of the C12N-PPd and OMe-PPz SAMs are somewhat lower and that of the FP-Pz SAM and considerably lower than those of the parent PPd and PPz monolayers (Table 4.3). For the FP-Pz film this can be associated with the much larger van-der-Waals radius of the fluorine atoms compared to hydrogens and the resulting larger van-der-Waals dimension of the fluorinated phenyl.[163,216] For the C12N-PPd and OMe-PPz SAMs, the lower packing densities are associated with the substituents, which, especially for C12N-PPd (two aliphatic chains per molecule), are comparably bulky. Moreover, substitution has a strong impact on intermolecular interactions, thus an effective packing in these monolayers might be affected by some degree of disorder.

4.5.2 NEXAFS Spectroscopy

C K-edge NEXAFS spectra of the DTC-based SAMs acquired at an X-ray incident angle of 55° (magic angle) are presented in Figure 4.41a; the differences between the spectra collected under normal (90°) and grazing (20°) incidence are contained in Figure 4.41b. The 55° spectra are not affected by molecular orientation effects and are, thus, directly representative of the electronic structure of the studied films.[131] In contrast, the difference spectra provide a useful tool to monitor the dependence of the magnitude of the absorption resonances on the incidence angle of the primary X-ray beam, termed as linear dichroism and delivering information on molecular orientation.[131]

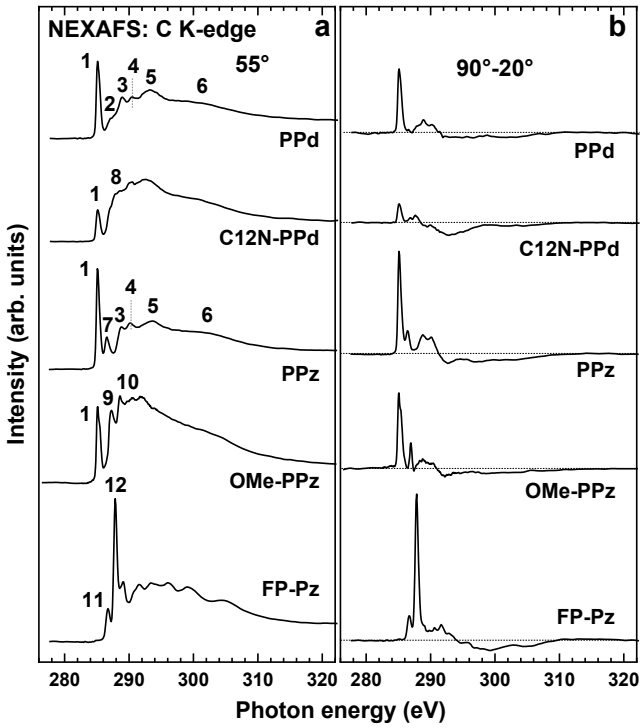

Figure 4.41: C K-edge NEXAFS spectra of the DTC-based SAMs acquired at an X-ray incident angle of 55° (a), along with the respective difference between the spectra collected under the normal (90°) and grazing (20°) incidence geometry (b). Individual absorption resonances are marked by numbers. The horizontal dashed lines in panel b correspond to zero.

The 55° spectra of the basic PPd and PPz SAMs are dominated by the characteristic absorption resonances of the terminal phenyl ring,[131,188,189,220] viz. the most intense π_1* resonance at ~285.1 eV (**1**), the respective π_2* peak at 288.8-288.9 eV (**3**), a further π* resonance at 290.2 eV (**4**), and several σ* resonances (**5**-**6**) at higher excitation energies. In addition, there are the R*/C-S* resonances[131,189] at ~287.3 eV (**2**) and the comparably strong π* resonance at ~286.5 eV (**7**) in the case of the PPz SAM, which stems presumably from the splitting of the π* feature of the phenyl ring (**1**) due to the effect of the adjacent pyperazine moiety.[131] Such a splitting also affects the π_2* resonance (**3**) in this spectrum,[213] resulting in a stronger intensity of the 290.2 eV feature (**4**) as compared to the PPd case. The absorption structure associated with the piperidine (PPd) and piperazine (PPz) moieties could not be unequivocally identified, since the spectra of these species do not exhibit intense, discrete features in the pre-edge and at-edge regions (see refs. 217 and 218) and the related σ* resonances overlap with those of the phenyl ring.

The 55° spectra of the C12N-PPd and OMe-PPz SAMs exhibit a significant relative weakening of the π_1* resonance (**1**), which is associated with the substitution. This effect is especially pronounced for the C12N-PPd film, the spectrum of which shows also an additional resonance at ~287.7 eV (**8**) associated with the alkyl chains (most likely excitations into Rydberg states,[129] but there are also alternative assignments). Additionally, there is a pattern of σ* resonances at higher photon energies. The latter resonances stem predominantly from the alkyl chains and are presumably the reason for the comparably low intensity of the π_1* resonance, since the spectrum is normalized to the height of the absorption edge proportional to the entire number of the carbon atoms but with a stronger contribution from the alkyl chains due to the more pronounced attenuation of the signal originating from the PPd moiety. The

spectrum of the OMe-PPz SAM exhibits a π* resonance at 287.3 eV (**9**) stemming from the splitting of the π_1* feature of the phenyl ring (**1**) due to its substitution,[131] and an additional π* resonance at ~288.6 eV (**10**), which most likely has π_2* (**3**) character.

The 55° spectrum of the FP-Pz SAM is dominated by the absorption resonances of the fluorinated phenyl ring, with the most prominent, characteristic features at ~286.65 eV (**11**) and ~287.8 eV (**12**) assigned to the $C_{1s} \rightarrow \pi^*$ transitions at the carbon atoms which are not bonded, respectively, directly bonded to fluorine atoms.[219,220] Interestingly, the position of the former feature is distinctly higher than that for pentafluorobenzene (~285.5 eV)[220] and pentafluorobenzene terminated SAMs (285.7 eV)[163], which is presumably related to the bonding of the respective carbon atom to the adjacent piperazine ring. There are several additional less intense π*- and π*-like resonances, for which the positions and assignments can be found in literature.[219,220]

In addition to the magic angle spectra analyzed above, the linear dichroism effects in the DTC-based SAMs were monitored. The 90°-20° curves for all monolayers in Figure 4.41b exhibit intense difference peaks at the positions of the absorption resonances. They reflect a pronounced linear dichroism suggesting high orientational order in the monolayers. In addition, the signs of the observed difference peaks, viz. the positive signs for the resonances with π*-character and the negative signs for those with σ*-character, indicate, in view of the orientation of the respective orbitals, an upright molecular orientation in all studied SAMs.

Along with these qualitative considerations, a quantitative analysis of the entire set of the NEXAFS data acquired at different X-ray incidence angles was performed to get information about molecular orientation in the DTC SAMs. The analysis was carried out within a standard theoretical framework,[131] comparing the angular dependence of the intensities of selected absorption resonances, *I*, with the appropriate theoretical expression. The average angle describing the orientation of the respective molecular orbital in terms of its transition dipole moment (TDM) is used as fitting parameter[163,189] For this analysis we chose either the most prominent resonance associated with the phenyl ring (**1**) or the most prominent π* resonance of the fluorinated phenyl ring ($C_{1s}^{C\text{-}F} \rightarrow \pi^*$; **12**), using these moieties as markers for the orientation determination.

The average tilt angle, α ,of the corresponding orbitals (with their “direction” defined perpendicular to the plane of the ring) relative to the surface normal can be derived from a standard expression for a vector-type orbital[131]

$$I(\alpha,\theta) = A\left\{P \times \frac{1}{3}\left[1 + \frac{1}{2}\cdot(3\cdot\cos^2\theta - 1)\cdot(3\cdot\cos^2\alpha - 1)\right] + (1-P)\frac{1}{2}\sin^2\alpha\right\} \qquad \textbf{(4.3)}$$

where *A* is a constant, *P* is the polarization degree of the X-rays, and θ is the X-ray incidence angle. The derived α values are compiled in Table 4.4. They can be used to calculate the average tilt angle of the molecular backbone, β, according to the relation:

$$\cos\alpha = \sin\beta\cdot\cos\gamma \qquad \textbf{(4.4)}$$

where γ is the twist angle of the molecular backbone with respect to plane spanned by the surface normal and the molecular axis; it is defined as 0, if the tilt occurs perpendicular to the plane of the ring.[132] Under the latter condition, β = 90°-α, representing the minimum possible molecular inclination consistent with the NEXAFS data. The respective values are given in Table 4.4.

All other values of the twist angle will result in larger values of the molecular tilt angles at the given α values. Regretfully, the twist angle cannot be determined experimentally, which is a general constraint of NEXAFS experiments on aromatic SAMs. Consequently, in the given

case, for the most basic PPd and PPz SAMs, we rely on theoretical simulations, deriving β and γ from the optimized molecular structures, calculating the respective α, and comparing them with the experimental values.

Table 4.4. Average tilt angle of the π* orbitals of the phenyl ring and the minimal possible average molecular tilt angle for the DTC-based SAMs on gold. The experimental error is estimated at ±3°.

Monolayer	PPd	C12N-PPd	PPz	OMe-PPz	FP-Pz
Tilt angle of the π orbitals, α	72.5°	70°	81.5°	72°	79°
Minimal molecular tilt angle, β'	17.5°	20.0°	8.5°	18.0°	11.0°

Interestingly, the inclination of the π-system expressed by α in PPz is smaller than that in PPd, in full agreement with the packing density values (Table 4.3). The substitution of the terminal phenyl ring in both PPz and PPd, given by the examples of C12-PPd and OMe-PPz, results in an increase of the inclination, which is a common behavior observed in different types of SAMs. Finally, the fluorination of the terminal phenyl ring in FP-Pz does not result in a noticeable disturbance of the molecular inclination, which again appears to be a general trend for SAMs containing perfluorinated aromatic moieties.[163,222] As mentioned, the comparably low packing density in FP-Pz (Table 4.3) is associated with the large van der Waals dimensions of the fluorinated ring compared to the phenyl one.

4.5.3 Work Function

The work function values of Au surfaces modified with the PPz and PPd SAMs were determined to be 3.9 eV and 3.7 eV (±0.05), respectively; accordingly, compared to a work function of a reference Au substrate of 5.2 eV, the shifts amount to −1.3 eV and −1.5 eV. The work function values of the C12N-PPd, OMe-PPz, and FP-Pz SAMs are 3.2 eV, 3.5 eV, and 4.3 eV according to the literature.[12] They show the expected trends when compared to the work function values of the parent PPz and PPd derivatives, viz. a decrease in the work function upon substitution with the C12N and OMe groups and an increase in the work function upon perfluorination of the terminal phenyl ring.

5 Conclusions

The major goal of this work was interfacial dipole engineering by specially designed monomolecular films. A variety of new concepts was utilized, with a particular emphasis on the extension and optimization of the embedded dipole approach. As experimental tools, a combination of X-ray Photoelectron Spectroscopy (XPS), Near-Edge X-Ray Absorption Fine Structure (NEXAFS) Spectroscopy, two-terminal junction approach with top EGaIn electrode, and Kelvin-Probe (KP) measurements was used.

The starting point of my work was characterization of the structure, molecular orientation, morphology, and electrostatic properties of the mixed C10EC10-up/C10EC10-down SAMs on gold. According to the XPS and NEXAFS spectroscopy data, the mixed SAMs are well-defined and contamination-free. The packing density and molecular orientation in these SAMs are similar to those of the “parent”, single-component monolayers. Applying XPS as a morphology tool, it was possible to estimate that the mixed C10EC10-up/C10EC10-down SAMs represent homogeneous intermolecular mixtures of both components, down to the molecular level. The analysis of the C 1s XPS spectra and the work function data suggests that the compositions of the mixed SAMs fully mimics the mixing ratio of both components in the solutions from which these SAMs were prepared. This behavior is associated with a comparably small contribution of the dipole−dipole interaction between the embedded ester groups into the entire balance of the structure-building forces in the C10EC10-up/C10EC10-down SAMs comprised of the quite long molecules. From a practical viewpoint, the data presented in this study suggest that the mixed C10EC10-up/C10EC10-down monolayers allow the tuning of the work function of the gold substrate in a controlled fashion within a ~1.1 eV range, between the ultimate values for the single-component C10EC10-up and C10EC10-down monolayers, namely, 3.83 eV and 4.92 eV, respectively, and with persistent chemical composition at the SAM-ambient interface. Because of the intermolecular mixing, the SAM-induced work function change is nearly homogeneous, down to the molecular level, excluding formation of hot or cold spots for injection of the charge carriers as far as these SAMs are used for the energy level alignment at the interfaces between electrodes, buffer layers, and organic semiconductor in organic solar cells, organic light emission diodes, and organic transistors. Of course, aliphatic SAMs have certain limitations in terms of inferior electric transport properties as compared to aromatic ones, but they probably can be used in certain cases, when these properties are not of primary importance or when a methyl termination and persistent interfacial chemistry are of particular significance. From the scientific viewpoint, this work demonstrates that not only aromatic but also aliphatic mixed SAMs with mid-chain substituted dipolar groups can be successively used for the work function control and tuning at surfaces and interfaces.

The next step was to test to what extent the concept of embedded dipole is applicable to an alternative substrate, taking Ag(111) as a representative example and using two different types of SAMs, viz. PPmP1-up/down and C10EC10-up/down, as test systems. Apart from either aromatic or aliphatic character of these films, the major differences between them were (i) the contribution of the embedded dipolar group in context of the structure-building interactions and (ii) the orientation of the dipole moment associated with the embedded group with respect to the molecular backbone.

For both types of the SAMs, the orientation of the embedded dipolar group was varied and the molecules with the oppositely oriented dipoles were combined together as mixed monolayers, which, according to the XPS data, represented homogeneous mixtures of both components.

In all cases, pronounced electrostatic effects of the embedded dipolar group were observed, reflected, in a fully consistent fashion, by the electrostatic shift in photoemission and by the work function variation. The character and extent of these effects were however distinctly different for both types of SAMs. In the PPmP1-up/down case, the composition of the mixed monolayers was affected by the dipole-dipole interaction between the embedded groups, with a preference of the 50%-50% ratio. In contrast, for the C10EC10-up/down system, the composition of the mixed SAMs, similar to the case of Au substrate, mimicked that of the parent solution, because of comparably weak contribution of the embedded dipolar group to the entire balance of the structure-building interactions. Important in context of the energy level alignment, the work function of the PPmP1-up/down SAMs on Ag could be varied gradually in the 0.85 eV range, making possible both its increase and decrease with respect to the value for clean Ag. In contrast, the work function range accessible with the C10EC10-up/down monolayers was much smaller (~0.45 eV), which was explained by the strong inclination of the dipole moment of the embedded ester group with respect to the molecular backbone. The projection of this moment on the surface normal, determining the strength of the electrostatic effects, is then especially sensitive to molecular orientation, in contrast to the PPmP1-up/down SAMs where the dipole moment of the embedded ester group is directed along the molecular chain. Consequently, these films as well as other aromatic SAMs with embedded pyrimidine groups are better suitable for electrostatic engineering of different interfaces in organic electronics and photovoltaics, as far as the docking group is adapted to the respective materials.

Apart from the above conclusions related to possible applications of the embedded dipole SAMs, the observation of distinct electrostatic effects in photoemission and their good correlation with the work function behavior, suggest the general character of these effects. Their understanding is an important prerequisite for correct interpretation of the XPS spectra of monomolecular films. At the same time, they represent a valuable tool for characterization of such systems.

The results of the above-mentioned experiments showed that aromatic SAMs with the embedded pyrimidine group are more robust in terms of electrostatic interface engineering as compared to the aliphatic ones. In view of this conclusion, an optimization of the aromatic pyrimidine-substituted SAM precursors was pursued. The resulting molecules, PmP-up and PPm-down, feature the thiol docking group and a short heteroaromatic backbone, consisting of non-polar phenyl ring and polar pyrimidine group, "embedded" in two opposite orientations but in such a way that the corresponding nitrogen atoms are buried with respect to the SAM-substrate and SAM-ambient interfaces, decoupling them from the dipole engineering. Consequently, the chemical and physical identity of these interfaces, having the affinity to gold (thiol groups) and being chemically neutral (C−H) in the present work, can be flexibly adjusted, dependent on the adjacent materials and specific applications.

The experimental data suggest formation of densely packed and well-defined SAMs, with all molecules having upright geometry and bonded to the substrate by the thiolate docking group. The packing density, molecular orientation, structure and wetting properties (with only one exception) of these SAMs were found to be nearly independent of their electrostatic properties, with the latter correlating precisely with the molecular architecture and the orientation of the embedded dipolar group in particular. Such a behavior places the PmP-up, PPm-down, and PP SAMs as ideal systems for model studies in context of interfacial dipole engineering but also as highly suitable functional blocks for device applications. Both these options were illustrated by the example of OFETs with the SAM-modified electrodes (this part was performed by our cooperation partners), where, on the one hand, a clear correlation between the output

current and the height of the injection barrier for charge carriers was demonstrated and, on the other hand, optimal performance, competitive with other analogous devices, was achieved. Significantly, both p-type and n-type OFETs could be fabricated on the same electrode material (gold) using the same technological procedure and only selecting either PPm-down or PmP-up SAM in accordance with the organic semiconductor type. These transistors could also be fabricated on flexible substrates and integrated in complex device structures, which open good perspectives for mass production.

Along with the optimization of the pyrimidine-substituted SAMs, their modification by electron irradiation, in context of interfacial dipole engineering, was tried. It was shown that the WF of SAMs can be adjusted by electron irradiation in a quite broad energy range and in controlled fashion as far as these films contain a pyridine or pyrimidine group. This effect was demonstrated by the example of several representative heteroaromatic monolayers with either terminal pyridine group or embedded pyrimidine group having either upward or downward orientation with respect to the substrate and compared to the behavior of the reference, non-substituted oligophenyl-based SAM. The observed behavior of the pyridine and pyrimidine substituted films is presumably related to specific chemical transformations involving the nitrogen atoms in these moieties. The extent of the irradiation-induced WF changes is exceptionally large, varying from 0.4 eV to 0.8 eV depending on the specific system and covering a WF range of +(3.4−5.2) eV for the entire series as far as WF is monitored in situ, but the effect is diminished upon the exposure of the irradiated films to ambient. Two possible mechanisms behind this behavior are considered. Particular strengths of the approach are continuous tunability of the WF by selection of irradiation dose as well as a possibility of WF patterning. The latter was demonstrated by representative examples in framework of proximity printing lithography.

Within the last subproject, the issue of interfacial dipole engineering by selection of a specific docking group was addressed. In this context, molecular organization and electrostatic properties of dithiocarbamate-based SAMs on Au(111) were investigated, taking several representative monolayers as test systems. As the bridge unit, connecting the DTC anchor group and the terminal moiety, either piperazine or piperidine was used. Particular emphasis was put onto investigation of the two most basic compounds, PPd and PPz. They can be substituted with different functional terminal groups, thus allowing a wide range of molecular dipoles and offering a promising avenue for work function engineering at metal-organic interfaces. From this study, it emerges that the DTC anchor group represents a useful building block for monomolecular self-assembly on coinage metal substrates. Its combination with the piperidine or piperazine moiety allows for a sufficient flexibility, enabling the self-assembly of more rigid terminal groups (such as the phenyl rings in the case of PPd, PPz, and FP-Pz). It also allows the substitution with additional groups such as secondary amines, alkoxy groups, cyano groups, and many more (e.g. for C12N-PPd and OMe-PPz). Importantly, both sulfur atoms in the DTC anchor group bind to the substrate in a bidentate fashion, a very advantageous feature distinguishing the DTC moiety from other thiol-based dipodal and tripodal docking groups, that frequently show a heterogeneous chemistry for each individual sulfur atom (with coexisting thiolate, atomic sulfur, unbound sulfur, and disulfide configurations). Significantly, the DTC anchor, in combination with either piperidine or piperazine linker, allows a dense molecular packing, with almost the same density as for monodentate docking groups, such as thiolates in alkanethiolate and arylthiolate SAMs on Au(111). Such a dense molecular packing is characterized by small molecular inclination, as evidenced by both NEXAFS experiments and theoretical simulations performed by our partners. This inclination is only slightly altered upon substitution of the PPd and PPz

backbones with dipolar tail groups, or by partial fluorination of these moieties, which is a very favorable property in context of interfacial dipole engineering. The most important conclusion concerning the electrostatic properties of PPd and PPz SAMs concerns the location of the electrostatic dipole layer within these films, found to be in a region immediately adjacent to the metal/SAM interface. The most relevant difference found between the PPd and PPz platforms is a more upright orientation of the molecular backbone associated with a higher coverage for PPz, making especially this platform highly promising in view of further substitution of the terminal phenyl ring by polar groups, thereby providing access to a broad variety of interface dipoles.

The obtained results regarding the use of embedded dipoles for interfacial engineering in organic electronics and photovoltaics look quite promising and show high potential for further improvement. In particular, other dipolar groups than pyrimidine and ester can be tried, embedded dipole can be combined with a terminal dipole, adaptation of embedded dipole SAMs to other substrates can be tested, the concept can be extended to distributed dipoles, etc. In addition, a tailored design of the docking group and molecular architectures involving multiple anchoring groups can be promising as well. We have already performed some preliminary experiments in this context, but their results lie beyond the given PhD thesis.

A. Supplementary Data

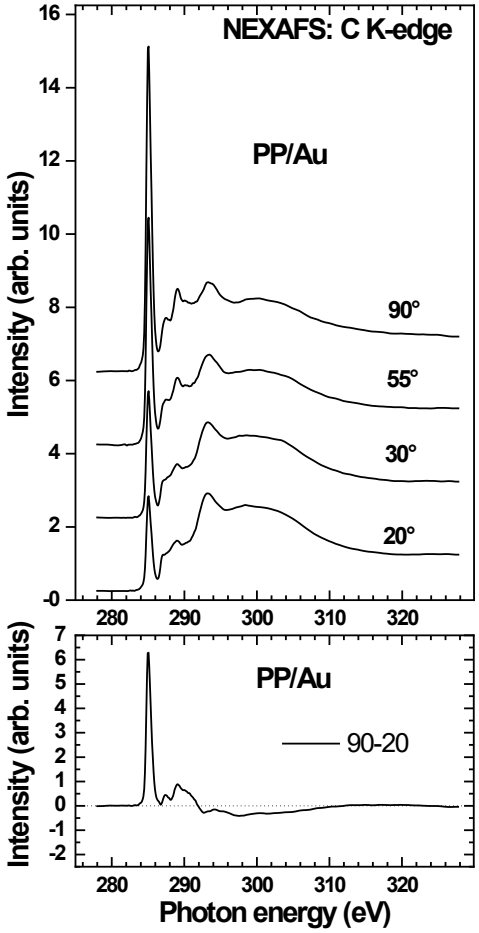

Figure A.1: C K-edge NEXAFS spectra of the reference PP (BPT) SAMs acquired at different X-ray incidence angles (top panel), along with the respective difference between the spectra collected under the normal (90°) and grazing (20°) incidence geometry (bottom panel). The horizontal dashed lines correspond to zero.

B. Supplementary Data by our Partners

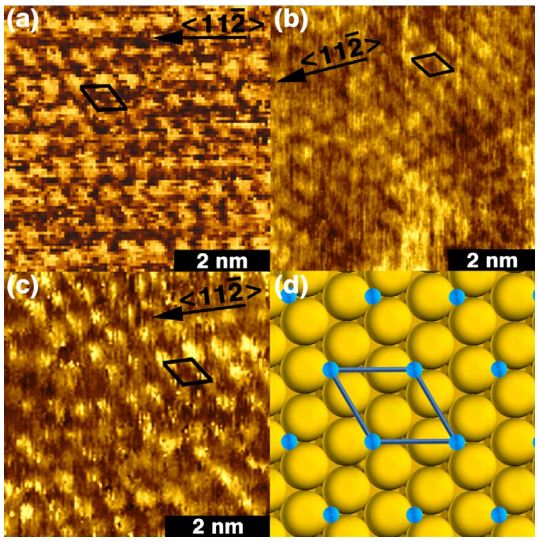

Figure B.1: STM images of the dominant (√3×√3)R30° phase in the PmP-up (a), PP (b) and PPm-down (c) along with a scheme of the respective molecular arrangement (d; it is assumed that the sulfur is sitting on top of a three-fold hollow side). In the STM images, the unit cell and a representative low-index direction are marked. (measured by the group of A. Terfort, Frankfurt University)

Table B.2: DFT calculated average tilt angles of the π* orbitals α, molecular tilt angle β and molecular twist angle γ in the PmP-up and PPm-down SAMs. 1, and 2 denote the values for the two symmetry inequivalent molecules in the unit cell. The value of α_{av} is obtained employing the averaging described in the main text. The twist angle is considered to be zero, when the tilt occurs perpendicular to the molecular plane.[132] (calculated by the group of E. Zojer, TU Graz, Austria)

Monolayer	α_{av}	α_1	α_2	β_1	β_2	γ_1	γ_2
PmP-up/Au	69.5°	75.8°	64.6°	29.6°	25.6°	60.2°	7.7°
PPm-down/Au	66.5°	75.7°	59.5°	31.5°	30.8°	61.8°	7.2°

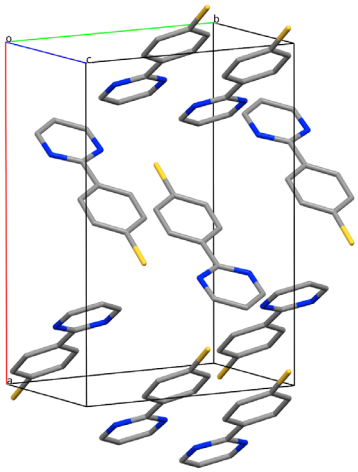

Figure B.3: 3D structure of the PmP-up crystal. (measured by M. Bolte, Frankfurt University)

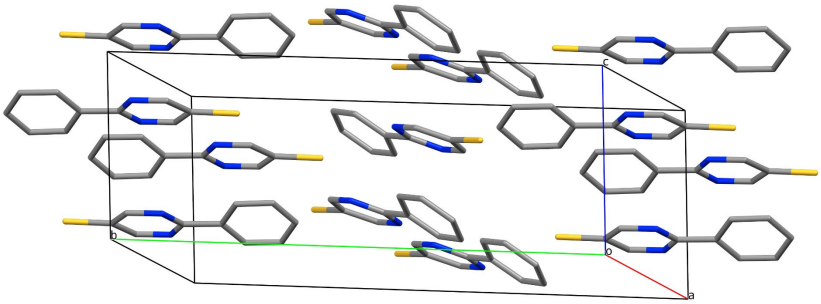

Figure B.4: 3D structure of the PPm-down crystal. (measured by M. Bolte, Frankfurt University)

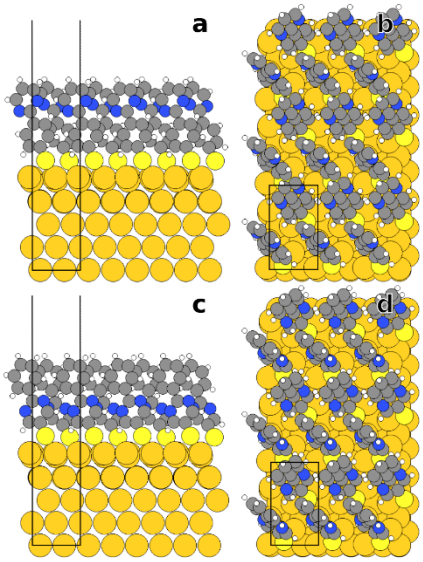

Figure B.5: DFT-optimized structures of the PmP-up (a,b) and PPm-down (c,d) SAMs. Color code: H – white, C – grey, N – blue, S – light yellow, Au-dark yellow. (calculated by the group of E. Zojer, TU Graz, Austria)

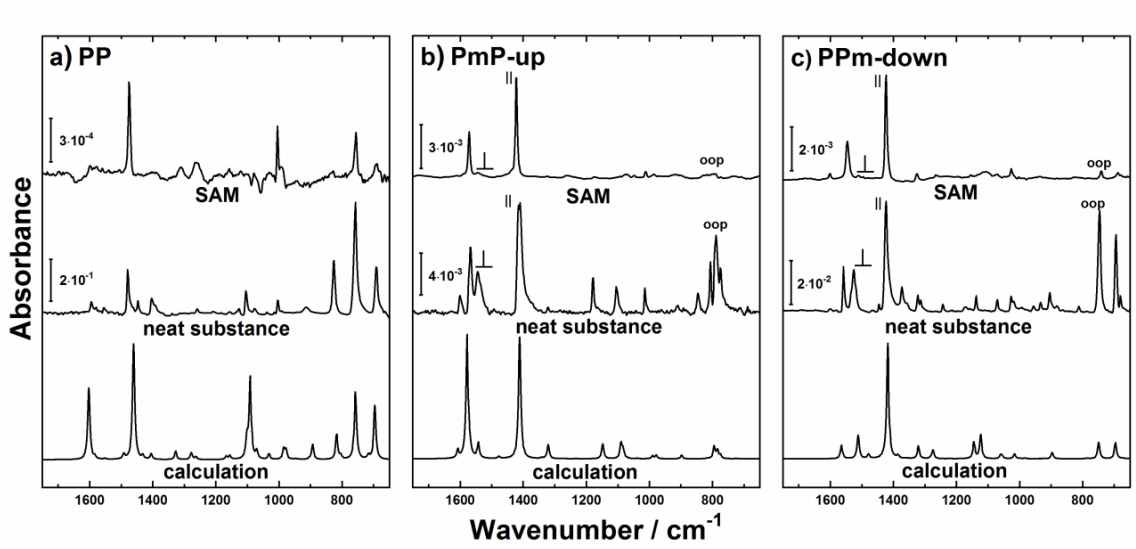

Figure B.6: IRRA spectra of PP (a), PmP-up (b), and PPm-down (c) SAMs (upper curves) along with the IR spectra of the neat substances (middle curves) and the DFT calculated spectra (bottom curves). Absorbance scale bars are given for the experimental spectra while the calculated spectra are displayed in arbitrary units. The modes which were used for the calculation of the tilt and twist angles are labeled as "||", "⊥" and "oop". (measured by the group of A. Terfort, Frankfurt University).

Table B.7: Positions (given in cm^{-1}) of most important vibrational modes in the IR spectra of the PPm-down and PmP-up molecules and corresponding SAMs, along with the respective theoretical values (DFT). The assignments of the vibrational modes was carried out on the basis of DFT calculations, which also provided the orientations of the respective TDMs. (measured by the group of A. Terfort, Frankfurt University).

			PPm-down			PmP-up		
No.	Mode[a)]	TDM[b)]	DFT	Neat[c)]	SAM[c)]	DFT	Neat[c)]	SAM[c)]
1	γ CH ring twist	oop	696	695 s	688 w			
2	γ CH ring twist	oop	749	747 s	741 w	794	789 s	790 w
3	ν CC, δ NCN	||				979	1014 m	1012 w
4	δ CH	||				1148	1179 m	1175 vw
5	ν CC, δ NCN	||				1321	1322 w	1324 w
6	ν CC CN, δ CH	⊥	1386	1373 m				
7	ν $CN^{(s)}$	||	1418	1424 vs	1424 vs	1412	1410 vs	1422 vs
8	ν $CN^{(as)}$	⊥	1512	1526 m	1511 w	1542	1544 m	1544 w
9	δ CH, ν CN	||	1565	1558 m	1546 m	1578	1567 s	1572 m
10	ν SH		2604	2535 m		2617	2578	

[a)] ν: stretch mode, δ: in plane bending mode, γ: out of plane bending mode, s: symmetric, as: asymmetric; [b)] ||: parallel to molecular backbone, ⊥: perpendicular to main molecular backbone and in plane of the aromatic ring, oop: perpendicular to the aromatic plane; [c)] vs: very strong, s: strong, m: medium, w: weak, vw: very weak.

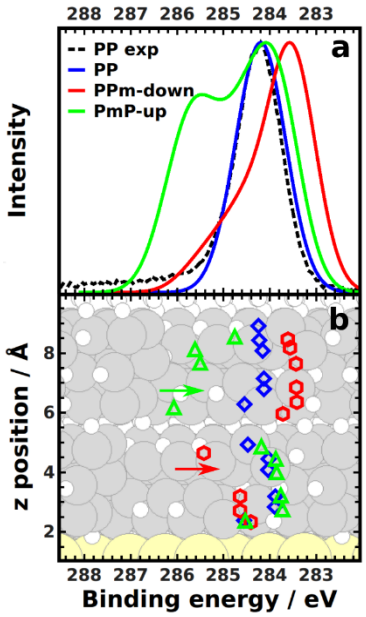

Figure B.8: top: DFT-calculated XPS spectra for the PP (blue), the PPm-down (red), and the PmP-up (green) SAMs. The spectra have been aligned to the experimental spectrum of PP and a damping consistent with a primary photon energy of 580 eV is assumed (for details see the main text; respectively, the Supporting Information). bottom: (shifted) core-level binding energies of individual C atoms averaged over equivalent atoms in the two molecules contained in the unit cell. For both spectra and energies of the individual levels, screening effects by the substrate according to the electrostatic model sketched in section 2 were considered. The average positions of the N atoms in the PPm-down and PmP-up SAMs are indicated by red, respectively green arrows. (calculated by the group of E. Zojer, TU Graz, Austria)

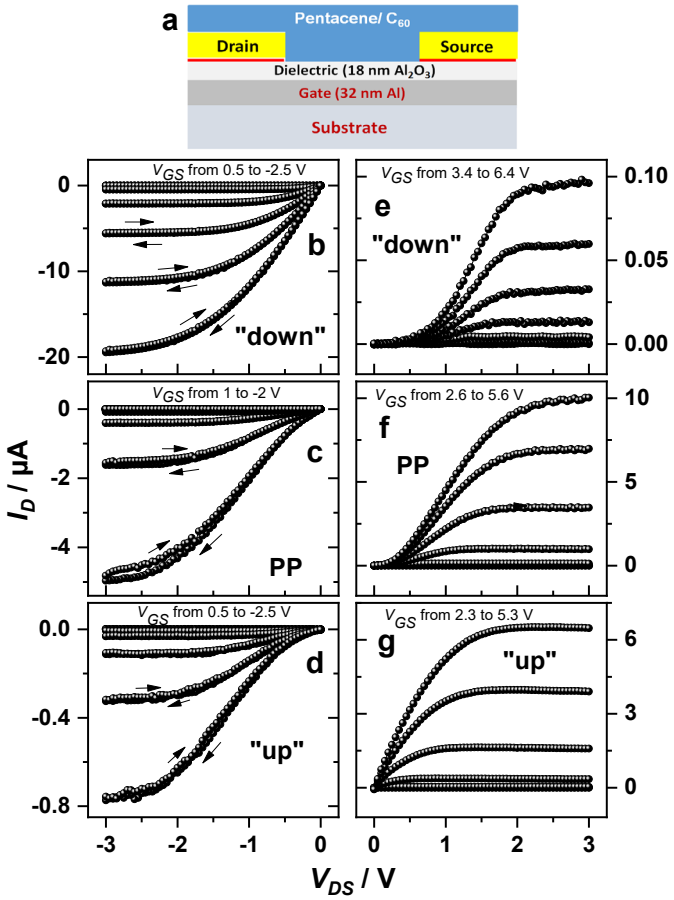

Figure B.9: Schematic of the bottom gate, bottom contact OFETs (a) featuring SAM-modified source and drain gold electrodes (50 nm) and either pentacene or C60 OSC; description of the fabrication process and the technical details can be found elsewhere.[183] Typical output characteristics of a p-type pentacene OFET with the electrodes modified by the PPm-down (b; "down"), PP (c), and PmP-up (d; "up") SAMs; typical output characteristics of a n-type C60 OFET with the electrodes modified by the PPm-down (e; "down"), PP (f), and PmP-up (g; "up") SAMs. The curves were acquired at several different VGS values varied in 0.5 steps in the ranges given in the panels. The channel length was 7.5 µm. The OFETs were fabricated either on glass (pentacene) or polycarbonate plastic film (C60). (measured by A. Petritz, Johanneum Research, Weiz, Austria)

Lists

List of Figures

List of Tables

List of Abbrevations

AFM	atomic force microscopy
AT	alkanethiol
BE	binding energy
CNM	carbon nanomembrane
DFT	density functional theory
DOS	density of states
DTC	dithiocarbamates
FWHM	full width at half maximum
EGaIn	eutectic gallium-indium
ESCA	electron spectroscopy for chemical analysis
EtOH	ethanol
HDT	hexadecanethiol, C16
HOMO	highest occupied molecule orbital
HRXPS	high resolution X-ray photoelectron spectroscopy
IMFP	inelastic mean free path
IP	ionization potential
IR	infrared
I-V	current-voltage
KP	kelvin probe
L	liquid
LUMO	lowest unoccupied molecule orbital
NEXAFS	near-edge X-ray absorption fine structure
OFET	organic field-effect transistor
OSC	organic semiconductor
PE	pass energy
PEY	partial electron yield
PVD	physical vapor deposition
RMS	root mean square
S	surface
SAM	self-assembled monolayer
STM	scanning tunneling microscope

TDMI	transition dipole moment
THF	tetrahydrofurane
TSG	template stripped gold
UHV	ultra-high vacuum
UV	ultraviolet
UPS	ultraviolet photoelectron spectroscopy
V	vapour
WCA	water contact angle
WF	work function
XPS	X-ray photoelectron spectroscopy

List of Chemicals

EtOH	ethanol
THF	tetrahydrofurane
PPP1	[1,1':4',1''-terphenyl]-4-ylmethanethiol
PPmP1-up	[1,1':4',1''-terphenyl]-4-ylmethanethiol
PPmP1-down	(4-(2-phenylpyrimidin-5-yl)phenyl)methanethiol
PP	[1,1'-biphenyl]-4-ylmethanethiol
PmP-up	(4-(pyrimidin-2-yl)phenyl)methanethiol
PPm-down	(2-phenylpyrimidin-5-yl)methanethiol
PmPm-up	[2,5'-bipyrimidin]-2'-ylmethanethiol
PmPm-down	[2,5'-bipyrimidin]-5-ylmethanethiol
PPd	4-phenylpiperidine-1-dithiocarbamate
C12N-PPd	4-(4-(dihexylamino)phenyl)piperidine-1-dithiocarbamatel
PPz	4-phenylpiperazine-1-dithiocarbamate
OMe-PPz	4-(4-methoxyphenyl)piperazine-1-dithiocarbamate
FP-Pz	4-(perfluorophenyl)piperazine-1-dithiocarbamate

List of Symbols

d	nm	thickness
e	V/m	electric field vector
E_b	eV	binding energy
E_f	eV	fermi level
E_{kin}	eV	kinetic energy
I	A	current
I	arb. Units	intensity
J	A/cm^2	current density
P	C/m^2	electric polarization
p	D	dipole transition operator
V	V	voltage
α	°	tilt angle of the π* orbitals
β	°	molecular tilt-angle
β	A^{-1}	tunneling decay constant
γ	°	molecular twist angle
θ	°	incidence angle
λ	nm	attenuation length
v	s^{-1}	frequency
σ	cm^2	cross-section
Φ	eV	work function
$\psi_{i/f}$		initial and final states
T	°C	temperature
m	kg	electron mass
h	$6.63x10^{14}$ Js	planck constant
e	1.6x10-19 C	elementary charge
k	$1.3x10^{-23}$	boltzmann constant

List of Pulications

Included in this thesis

1) C. Yildirim, E. Sauter, A. Terfort, and M. Zharnikov, The effect of electron irradiation on electric transport properties of aromatic self-assembled monolayers. Phys. Chem. C **121**, 7355−7364 (2017).
2) C. Yildirim, E. Sauter, A. Terfort, and M. Zharnikov, Modification of pyridine-terminated aromatic self-assembled monolayers by electron irradiation J. Phys. Chem. C **121**, 9982−9990 (2017).
3) E. Sauter, C. Yildirim, A. Terfort, and M. Zharnikov, Adjustment of the work function of pyridine and pyrimidine substituted aromatic self-assembled monolayers by electron irradiation, J. Phys. Chem. C **121**, 12834–12841 (2017).
4) E. Sauter, C.-O. Gilbert, J. Boismenu-Lavoie, J.-F. Morin, and M. Zharnikov, Mixed aliphatic self-assembled monolayers with embedded polar group, J. Phys. Chem. C **121**, 23017–23024 (2017).
5) E. Sauter, C.-O. Gilbert, J.-F. Morin, A. Terfort, and M. Zharnikov, Mixed monomolecular films with embedded dipolar groups on Ag(111), J. Phys. Chem. C **122**, 34, 19514-19523.
6) A. Petritz, M. Krammer, E. Sauter, M. Gärtner, G. Nascimbeni, B. Schrode, A. Fian, H. Gold, A. Cojocaru, E. Karner-Petritz, R. Resel, A. Terfort, M. Zharnikov, E. Zojer, K. Zojer, and B. Stadlober, Embedded dipole self-assembled monolayers for contact resistance tuning in p- and n-type organic thin film transistors and flexible electronic circuits, Adv. Funct. Mater., in press.
7) Eric Sauter,[#] Giulia Nascimbeni,[#] Daniel Trefz, Sabine Ludwigs, Egbert Zojer, Florian von Wrochem, and Michael Zharnikov, Dithiocarbamate Anchoring Group as Flexible Platform for Interface Engineering, prepared for submission (J. Phys. Chem. C), waiting for approval by Sony Deutschland GmBH.
8) Michael Gärtner,[#] Eric Sauter,[#] Giulia Nascimbeni,[#] Andreas Petritz, Adrian Wiesner, Martin Kind, Tarek Abu Husein, Michael Bolte, Barbara Stadlober, Egbert Zojer, Andreas Terfort, and Michael Zharnikov, Tailor-Made Self-Assembled Monolayers with Embedded Dipole Moments for Interface Engineering in Organic Electronics, in preparation (final stage).

[#] these authors have provided equivalent contributions

Besides this thesis

1) A. Bashir, E. Sauter, M. Rohwerder, M. Zharnikov, and W. Azzam, Side group induced polymorphism in self-assembled monolayers: 3,5-bis(trifluromethyl)benzenethiolate films on Au(111), Chem. Phys. Chem. **18**, 702 –714 (2017)
2) Y. Zhang, G. Ye, S. Soni, X. Qiu, T. L.Krijger, H. T. Jonkman, M. Carlotti, E. Sauter, M. Zharnikov, and R. C Chiechi, Cross-conjugation vs quinones: Controlling quantum interference in tunneling junctions comprising self-assembled monolayers via bond topology and functional groups, Chem. Sci. **9**, 4414-4423 (2018).
3) C.-Yu Chi, C.-H. Shih, E. Sauter, S. K. Das, H.-T. Lien, S.-T. Chang, M. Zharnikov and Y. Tai, Poly(styrenesulfonate)-doped ZnO as effective hole transport layer for humidity resistant organic solar cells, J. Mater. Chem. A **6**, 6542–6550 (2018).
4) S. Schneider, M. Brohmann, R. Lorenz, Y. J. Hofstetter, M. Rother, E. Sauter, M. Zharnikov, Y. Vaynzof, H.-J. Himmel and J. Zaumseil, Efficient n-doping and hole-blocking in single-walled carbon nanotube transistors with 1,2,4,5-tetrakis(tetramethyl-guanidino)benzene, ACS Nano **12**, 5895−5902 (2018).
5) M. Torres-Miranda, A. Petritz, E. Karner-Petritz, C. Prietl, E. Sauter, M. Zharnikov, H. Gold and B. Stadlober, Characterization & compact modeling of self-aligned short channel organic transistors, IEEE Transactions on Electron Devices, DOI: 10.1109/TED.2018.2867364.
6) M. Sánchez-Molina, A. Díaz, E. Sauter, M. Zharnikov and J. M. López-Romero, Synthesis of Novel Tripod-Shaped Molecules and their Immobilization on Au(111) Substrates, Appl. Surf. Sci., submitted.
7) M. Carlotti, S. Soni, S. Kumar, Y. Ai, E. Sauter, M. Zharnikov, and R. C. Chiechi, Two-Terminal Molecular Memory via Reversible Switching of Quantum Interference Features in Tunneling Junctions, Angew. Chem. Int. Ed., submitted.
8) M. Füser, E. Sauter, M. Zharnikov, and A. Terfort, Synergism in bond strength modulation opens an alternative concept for protective groups in surface chemistry: the example of selenolate monolayers, in preparation (final stage; Chem. Sci.).

List of conference contributions

1) E. Sauter*, A. Terfort, and M. Zharnikov, Adjustment of the properties of pyridine and pyrimidine substituted self-assembled monolayers by electron irradiation, DPG Spring Meeting, Berlin, Germany, **Mar. 2017**
2) E. Sauter*, A. Terfort, and M. Zharnikov, Adjustment of the properties of pyridine and pyrimidine substituted self-assembled monolayers by electron irradiation, π-System Figuration Workshop, Heidelberg, Germany, **Nov. 2017**
3) E. Sauter*, J.-F. Morin, and M. Zharnikov, Mixed aliphatic self-assembled monolayers with embedded polar group, DPG Spring Meeting, Berlin, Germany, **Mar. 2018**
4) E. Sauter, A. Terfort, and M. Zharnikov*, Work Function Tuning by Electron Irradiation of Homo- and Heteroaromatic Self-Assembled Monolayers, Materials for Organic Electronics: Synthesis, Spectroscopy and Theory, Heidelberg, Germany, **Jun. 2018**

*presenting person

References

1) Campbell, I. H.; Rubin, S.; Zawodzinski, T. A.; Kress, J. D.; Martin, R. L.; Smith, D. L.; Barashkov, N. N.; Ferraris, J. P. *Phys. Rev. B*, **54**, 14321–14324 (1996).

2) de Boer, B.; Hadipour, A.; Mandoc, M. M.; van Woudenbergh, T.; Blom, P. W. M. *Adv. Mater.*, **17**, 621–625 (2005).

3) Heimel, G.; Romaner, L.; Brédas, J.-L.; Zojer, E. *Phys. Rev. Lett.*, **96**, 196806 (2006).

4) Hamadani, B. H.; Corley, D. A.; Ciszek, J. W.; Tour, J. M.; Natelson, D. *Nano Lett*., **6**, 1303-1306 (2006).

5) Heimel, G.; Romaner, L.; Zojer, E. Brédas, J.-L., *Acc. Chem. Res.*, **41**, 721-729 (2008).

6) Cheng, X.; Noh, Y.-Y.; Wang, J.; Tello, M.; Frisch, J.; Blum, R.-P.; Vollmer, A.; Rabe, J. P.; Koch, N.; Sirringhaus, H., *Adv. Funct. Mater.*, **19**, 2407–2415 (2009).

7) Boudinet, D.; Benwadih, M.; Qi, Y.; Altazin, S.; Verilhac, J.-M.; Kroger, M.; Serbutoviez, C.; Gwoziecki, R.; Coppard, R.; Le Blevennec, G.; *et al*., *Org. Electron.*, **11**, 227–237 (2010).

8) Schmidt, C.; Witt, A.; Witte, G., *J. Phys. Chem. A*, **115**, 7234–7241 (2011).

9) Chiu, J. M.; Tai, Y., *ACS Appl. Mater. Interfaces*, **5**, 6946-6950 (2013).

10) Crivillers, N.; Osella, S.; Van Dyck, C.; Lazzerini, G. M.; Cornil, D.; Liscio, A.; Di Stasio, F.; Mian, S.; Fenwick, O.; Reinders, F.; *et al*., *Adv. Mater.*, **25**, 432–436 (2013).

11) Lange, I.; Reiter, S.; Pätzel, M.; Zykov, A.; Nefedov, A.; Hildebrandt, J.; Hecht, S.; Kowarik, S.; Wöll, C.; Heimel, G.; *et al*., *Adv. Funct. Mater*., **24**, 7014–7024 (2014).

12) Ford, W. E.; Gao, D.; Knorr, N.; Wirtz, R.; Scholz, F.; Karipidou, Z.; Ogasawara, K.; Rosselli, S.; Rodin, V.; Nelles, G.; *et al*., *ACS Nano*, **8**, 9173–9180 (2014).

13) Piersimoni, F.; Schlesinger, R.; Benduhn, J.; Spoltore, D.; Reiter, S.; Lange, I.; Koch, N.; Vandewal, K.; Neher, D., *J. Phys. Chem. Lett.*, **6**, 500−504 (2015).

14) Casalini, S.; Bortolotti, C. A.; Leonardi, F.; Biscarini, F., *Chem. Soc. Rev*., **46**, 40-71 (2017).

15) Ulman, A., *Chem. Rev.*, **96**, 1533-1554 (1996).

16) Schreiber, F. Self-Assembled Monolayers, *J. Phys.: Condens. Matter*, **16**, R881–R900 (2004).

17) Love, J. C.; Estroff, L. A.; Kriebel, J. K.; Nuzzo, R. G.; Whitesides, G. M., *Chem. Rev*., **105**, 1103-1169 (2005).

18) Kim, J.; Rim, Y. S.; Liu, Y.; Serino, A. C.; Thomas, J. C.; Chen, H.; Yang, Y.; Weiss, P. S., *Nano Lett*., **14**, 2946−2951 (2014).

19) Abu-Husein, T.; Schuster, S.; Egger, D. A.; Kind, M.; Santowski, T.; Wiesner, A.; Chiechi, R.; Zojer, E.; Terfort, A.; Zharnikov, M., *Adv. Funct. Mater*., **25**, 3943–3957 (2015).

20) Hehn, I.; Schuster, S.; Wachter, T.; Abu-Husein, T.; Terfort, A.: Zharnikov, M.; Zojer, E., *J. Phys. Chem. Lett*., **7**, 2994−3000 (2016).

21) Vetushka, A.; Bernard, L.; Guseva, O.; Bastl, Z.; Plocek, J.; Tomandl, I.; Fejfar, A.; Base, T.; Schmutz, P., *Phys. Stat. Sol. B*, **253**, 591–600 (2016).

22) Cabarcos, O. M.; Schuster, S.; Hehn, I.; Zhang, P. P.; Maitani, M. M.; Sullivan, N.; Giguere, J.-B.; Morin, J.-F.; Weiss, P. S.; Zojer, E.; *et al*., *J. Phys. Chem. C*, **121**, 15815–15830 (2017).

23) Cabarcos, O. M.; Shaporenko, A.; Weidner, T.; Uppili, S.; Dake, L. S.; Zharnikov, M.; Allara, D. L., *J. Phys. Chem. C*, **112**, 10842−10854 (2008).

24) Yoon, H. J.; Bowers, C. M.; Baghbanzadeh, M.; Whitesides, G. M., *J. Am. Chem. Soc.,* **136**, 16−19 (2014).

25) Taucher, T. C.; Hehn, I.; Hofmann, O. T.; Zharnikov, M.; Zojer, E., *J. Phys. Chem. C*, **120**, 3428−3437 (2016).

26) E. Sauter, C.-O. Gilbert, J. Boismenu-Lavoie, J.-F. Morin, and M. Zharnikov, *J. Phys. Chem. C,* **121**, 23017–23024 (2017)

27) Laibinis, P. E.; Whitesides, G. M.; Allara, D. L.; Tao, Yu T.; Parikh, A. N.; Nuzzo, R. G., *J. Am. Chem. Soc.*, **113**, 7152–7167 (1991).

28) Holmlin, R. E., Haag, R.; Chabinyc, M. L.; Ismagilov, R. F.; Cohen, A. E.; Terfort, A.; Rampi, M. A.; Whitesides, G. M., *J. Am. Chem. Soc.*, **123**, 5075-5085 (2001).

29) Adams, D. M.; Brus, L.; Chidsey, C. E. D.; Creager, S.; Creutz, C.; Kagan, C. R.; Kamat, P. V.; Lieberman, M.; Lindsay, S.; Marcus, R. A.; *et al*., *J. Phys. Chem. B*, **107**, 6668-6697 (2003).

30) Branchi, B.; Simeone, F. C.; Rampi, M. A., *Top Curr. Chem.*, **313**, 85–120 (2012).

31) Simmons, J. G., *J. Appl. Phys.*, **34**, 1793−1803 (1963).

32) Heimel, G.; Romaner, L.; Bredas, J.-L.; Zojer, E., *Langmuir*, **24**, 474-482 (2008).

33) Bowers, C. M.; Rappoport, D.; Baghbanzadeh, M.; Simeone, F. C.; Liao, K.-C.; Semenov, S. N.; Żaba, T.; Cyganik, P.; Aspuru-Guzik, A.; Whitesides, G. M., *J. Phys. Chem. C*, **120**, 11331−11337 (2016).

34) Wächter, T.; Weinhardt, L.; Terfort, A.; Zharnikov, M., *J. Phys. Chem. C*, **122**, 12534−12548 (2018).

35) G. Yang, G. Liu, *J. Phys. Chem. B*, **107**, 8746–8759 (2003).

36) Shaporenko, A.; Brunnbauer, M.; Terfort, A.; Grunze, M.; Zharnikov, M., *J. Phys. Chem. B*, **108**, 14462-14469 (2004).

37) Azzam, W.; Bashir, A.; Terfort, A.; Strunskus, T.; Wöll, Ch., *Langmuir*, **22**, 3647-3655 (2006).

38) Ballav, N.; Shaporenko, A.; Terfort, A.; Zharnikov, M., *Adv. Mater.*, **19**, 998−1000 (2007).

39) Jeyachandran, Y. L.; Zharnikov, M., *J. Phys. Chem. C*, **116**, 14950−14959 (2012).

40) Ballav, N.; Thomas, H.; Winkler, T.; Terfort, A.; Zharnikov, M., *Angew. Chem., Int. Ed.*, **48**, 5833−5836 (2009).

41) Tai, Y.; Shaporenko, A.; Noda, H.; Grunze, M.; Zharnikov, M., *Adv. Mater.*, **17**, 1745−1749 (2005).

42) Noda, H.; Tai, Y.; Shaporenko, A.; Grunze, M.; Zharnikov, M., *J. Phys. Chem. B*, **109**, 22371−22376 (2005).

43) Geyer, W.; Stadler, V.; Eck, W.; Zharnikov, M.; Gölzhäuser, A.; Grunze, M., *Appl. Phys. Lett.*, **75**, 2401−2403 (1999).

44) Eck, W.; Stadler, V.; Geyer, W.; Zharnikov, M.; Gölzhäuser, A.; Grunze, M., *Adv. Mater.*, **12**, 805−808 (2000).

45) Gölzhäuser, A.; Geyer, W.; Stadler, V.; Eck, W.; Grunze, M.; Edinger, K.; Weimann, Th.; Hinze, P., *J. Vac. Sci. Technol., B: Microelectron. Process. Phenom*., **18**, 3414−3418 (2000).

46) Gölzhäuser, A.; Eck, W.; Geyer, W.; Stadler, V.; Weimann, T.; Hinze, P.; Grunze, M., *Adv. Mater.*, **13**, 803−806 (2001).

47) Schmelmer, U.; Jordan, R.; Geyer, W.; Eck, W.; Gölzhäuser, A.; Grunze, M.; Ulman, *Angew. Chem., Int. Ed.*, **42**, 559−563 (2003).

48) Gates, B. D.; Xu, Q.; Stewart, M.; Ryan, D.; Willson, C. G.; Whitesides, G. M. *Chem. Rev.*, **105**, 1171−1196 (2005).

49) Turchanin, A.; Tinazli, A.; El-Desawy, M.; Grossann, H.; Schnietz, M.; Solak, H. H.; Tampe, R.; Gölzhäuser,, *Adv. Mater.*, **20**, 471−477 (2008).

50) Shah, S. S.; Howland, M. C.; Chen, Li-J.; Silangcruz, J.; Verkhoturov, S. V.; Schweikert, E. A.; Parikh, A. N.; Revzin, A., *ACS Appl. Mater. Interfaces*, **1**, 2592−2601 (2009).

51) Saavedra, H. M.; Mullen, T. J.; Zhang, P.; Dewey, D. C.; Claridge, S. A.; Weiss, P. S., *Rep. Prog. Phys.*, **73**, 036501 (2010).

52) Shestopalov, A. A.; Clark, R. L.; Toone, E. J. *Nano Lett.*, **10**, 43−46 (2010).

53) Khan, M. N.; Tjong, V.; Chilkoti, A.; Zharnikov, M., *Angew. Chem., Int. Ed.*, **51**, 10303−10306 (2012).

54) Eck, W.; Küller, A.; Grunze, M.; Volkel, B.; Gölzhäuser, A., *Adv. Mater.*, **17**, 2583−2586 (2005).

55) Nottbohm, C. T.; Sopher, R.; Heilemann, M.; Sauer, M.; Gölzhäuser, A. J., *Biotechnol.*, **149**, 267−271 (2010).

56) Rhinow, D.; Vonck, J.; Schranz, M.; Beyer, A.; Gölzhäuser, A.; Hampp, N., *Phys. Chem. Chem. Phys*., **12**, 4345−4350 (2010).

57) Zheng, Z.; Nottbohm, C. T.; Turchanin, A.; Muzik, H.; Beyer, A.; Heilemann, M.; Sauer, M.; Gölzhäuser, A. Janus Nanomembranes:, *Angew. Chem., Int. Ed*., **49**, 8493−8497 (2010).

58) Meyerbröker, N.; Li, Zi-An; Eck, W.; Zharnikov, M., *Chem. Mater*., **24**, 2965−2972 (2012).

59) Angelova, P.; Vieker, H.; Weber, N.-E.; Matei, D.; Reimer, O.; Meier, I.; Kurasch, S.; Biskupek, J.; Lorbach, D.; Wunderlich, K.; *et al*., *ACS Nano*, **7**, 6489−6497 (2013).

60) Turchanin, A.; Gölzhäuser, A., *Adv. Mater.*, **28**, 6075−6103 (2016).

61) Zharnikov, M.; Grunze, M., *J. Vac. Sci. Technol., B: Microelectron. Process. Phenom.,* **20**, 1793−1807 (2002).

62) Cyganik, P.; Vandeweert, E.; Postawa, Z.; Bastiaansen, J.; Vervaecke, F.; Lievens, P.; Silverans, R. E.; Winograd, N., *J. Phys. Chem. B*, **109**, 5085−5094 (2005).

63) Turchanin, A.; Käfer, D.; El-Desawy, M.; Wöll, C.; Witte, G.; Gölzhäuser, *Langmuir*, **25**, 7342−7352 (2009).

64) Amiaud, L.; Houplin, J.; Bourdier, M.; Humblot, V.; Azria, R.; Pradier, C.-M.; Lafosse, A., *Phys. Chem. Chem. Phys.*, **16**, 1050−1059 (2014).

65) Matei, D. G.; Weber, N.-E.; Kurasch, S.; Wundrack, S.; Woszczyna, M.; Grothe, M.; Weimann, T.; Ahlers, F.; Stosch, R.; Kaiser, U.; *et al.*, *Adv. Mater.*, **25**, 4146−4151 (2013).

66) Himmel, H.-J.; Terfort, A.; Wöll, C., *J. Am. Chem. Soc.*, **120**, 12069−12074 (1998).

67) Ishida, T.; Mizutani, W.; Akiba, U.; Umemura, K.; Inoue, A.; Choi, N.; Fujihira, M.; Tokumoto, H., *J. Phys. Chem. B*, **103**, 1686−1690 (1999).

68) Ishida, T.; Choi, N.; Mizutani, W.; Tokumoto, H.; Kojima, I.; Azehara, H.; Hokari, H.; Akiba, U.; Fujihira, M., *Langmuir*, **15**, 6799−6806 (1999).

69) Liu, J.; Schüpbach, B.; Bashir, A.; Shekhah, O.; Nefedov, A.; Kind, M.; Terfort, A.; Wöll, C., *Phys. Chem. Chem. Phys.*, **12**, 4459−4472 (2010).

70) Yildirim, C.; Sauter, E.; Terfort, A.; Zharnikov, M., *J. Phys. Chem. C*, **121**, 9982−9990 (2017).

71) Paniagua, S. A.; Giordano, A. J.; Smith, O. N. L.; Barlow, S.; Li, H.; Armstrong, N. R.; Pemberton, J. E.; Brédas, J.-L.; Ginger, D.; Marder, S. R., *Chem. Rev.*, **116**, 7117−7158 (2016).

72) Knesting, K. M.; Hotchkiss, P. J.; MacLeod, B. A.; Marder, S. R.; Ginger, D. S., *Adv. Mater.*, **24**, 642–646 (2012).

73) Zhao, Y.; Pérez-Segarra, W.; Shi, Q.; Wei, A., *J. Am. Chem. Soc.*, **127**, 7328-7329 (2005).

74) Gao, D.; Scholz, F.; Nothofer, H.-G.; Ford, W. E.; Scherf, U.; Wessels, J. M.; Yasuda, A. von Wrochem, F., *J. Am. Chem. Soc.*, **133**, 5921–5930 (2011).

75) Reeler, N. E. A.; Lerstrup, K. A.; Somerville, W.; Speder, J.; Petersen, S. V.; Laursen, Bo W.; Arenz, M.; Qiu, X.; Vosch, T.; Nørgaard. K., *Sci. Rep.*, **5**, 15273 (2015).

76) Simonsen, J. B.; Reeler, N. E. A.; Fossum, A.; Lerstrup, K. A.; Laursen, Bo W.; Nørgaard, K., *Nano Res.*, **9**, 3093–3098 (2016).

77) Meyer, D.; Schäfer, T.; Schulz, P.; Jung, S.; Rittich, J.; Mokros, D.; Segger, I.; Maercks, F.; Effertz, C.; Mazzarello, R.; Wuttig, M., *Langmuir*, **32**, 8812–8817 (2016).

78) Zhao, Y.; Newton, J. N.; Liu, J.; Wei, A., *Langmuir*, **25**, 13833–13839 (2009).

79) Ford, W. E.; Gao, D.; Scholz, F.; Nelles, G.; von Wrochem, F., *ACS Nano*, **7**, 1943–1951 (2013).

80) Naumann, R.; Schiller, S. M.; Giess, F.; Grohe, B.; Hartman, K. B.; Karcher, I.; Koper, I.; Lubben, J.; Vasilev, K.; Knoll, W. *Langmuir*, **19**, 5435-5443 (2003).

81) Nakamaru, S.; Scholz, F.; Ford, W.E.; Goto, Y.; von Wrochem, F., *Adv. Mater.*, **29**, 1605924 (2017).

82) E. Poirier, E. D. Pylant, *Science*, **272**, 1145-1148 (1996).

83) R. G. Nuzzo, D. L. Allara, *J. Am. Chem. Soc.*, **105**, 4481-4483 (1983).

84) M. D. Porter, T. B. Bright, D. L. Allara, C. E. D. Chidsey, *J. Am. Chem. Soc.*, **109**, 3559-3568 (1987).

85) L. H. Dubois, R. G. Nuzzo, Annu. *Rev. Phys. Chem.*, **43**, 437-463 (1992).

86) C. D. Bain, J. Evall, G. M. Whitesides, *J. Am. Chem. Soc.*,**111**, 7155-7164 (1989).

87) C. D. Bain, G. M. Whitesides, *Science*, **240**, 62-63 (1988).

88) H. A. Biebuyck, C. D. Bain, G. M. Whitesides, *Langmuir*, **10**, 1825-1831 (1994).

89) L. H. Dubois, B. R. Zegarski, R. G. Nuzzo, *J. of Chem. Phys.*, **98**, 678 (1993).

90) M. M. Walczak, C. Chung, S. M. Stole, C. A. Widrig, M. D. Porter, *J. Am. Chem. Soc.*, **113**, 2370-2378 (1991).

91) P. Fenter, P. Eisenberger, J. Li, N. Camillone, S. Bernasek, G. Scoles, T. A. Ramanarayanan, K. S. Liang, *Langmuir*, **7**, 2013-2016 (1991).

92) J. C. Love, D. B. Wolfe, R. Haasch, M. L. Chabinyc, K. E. Paul, G. M.Whitesides, R. G. Nuzzo, *J. Am. Chem. Soc.*, **125**, 2597-2609 (2003).

93) A. Carvalho, M. Geissler, H. Schmid, B. Michel, E. Delamarche, *Langmuir*, **18**, 2406-2412 (2002).

94) Z. Li, S.-C. Chang, R. S. Williams, *Langmuir*, **19**, 6744-6749 (2003).

95) N. Muskal, I. Turyan, D. Mandler, *J. Electroanal. Chem.*, **409**, 131-136 (1996).

96) CambridgeSoft, ChemDraw 16.0, *Software*, 2018.

97) Hofmann, S., Auger- and X-ray photoelectron spectroscopy in materials science: A User-Oriented Guide. 1st ed., Springer-Verlag Berlin Heidelberg, 2013.

98) van der Heide, P., X-ray Photoelectron Spectroscopy: An introduction to Principles and Practices. 2011: Wiley.

99) Ratner, B.D. and D.G. Castner, Electron Spectroscopy for Chemical Analysis, in Surface Analysis – The Principal Techniques. 2009, John Wiley & Sons, Ltd. 47-112.

100) https://en.wikipedia.org/wiki/Angle-resolved_photoemission_spectroscopy#/media/File:ARPESgeneral.png

101) D. A. Shirley, *Phys. Rev. B*, **5**, 4709-4714 (1972).

102) S. Tougaard, *Surf. Interface Anal.*, **25**, 137-154 (1997).

103) C. L. A. Lamont, J. Wilkes, *Langmuir*, **15**, 2037-2042 (1999).

104) F. Schreiber, *Prog. Surf. Sci.*, **65**, 151-257 (2000).

105) H. Kondoh, M. Iwasaki, T. Shimada, K. Amemiya, T. Yokoyama, T. Ohta, M. Shimomura, S. Kono, *Phys. Rev. Lett.*, **90**, 066102 (2003).

106) P. W. Atkins, J. de Paula, Physikalische Chemie, 4th ed., Wiley-VCH, 2006

107) Meyerbröker, N. and M. Zharnikov, *Langmuir*, **28**(25), 9583-9592 (2012).

108) Olsen, C. and P.A. Rowntree, *J. Chem. Phys.*, **108**(9), 3750-3764 (1998).

109) S. Frey, H.-T. Rong, K. Heister, Y.-J. Yang, M. Buck, and, M. Zharnikov, *Langmuir*, **18**(8), 3142-3150 (2002).
110) M. Zharnikov, S. Frey, K. Heister, and M. Grunze, Langmuir, **16**(6), 2697-2705 (**2000**).
111) David A. Hutt, Elaine Cooper, and, and Graham J. Leggett, *J. Phys. Chem. B*, **102**, 174-184 (1998).
112) H. Rieley, G. K. Kendall, F. W. Zemicael, T. L. Smith, and S. Yang., *Langmuir*, **14**, 5147-5153 (1998).
113) Y. L. Jeyachandran, T. Weber, A. Terfort, and M. Zharnikov, *J. Phys. Chem. C*, **117**, 5824-5830 (2013).
114) A. Turchanin, M. Schnietz, M. El-Desawy, H. H. Solak, *Small*, **3**(12): 2114-2119 (2007).
115) P. E. Laibinis, R. L. Graham, H. A. Biebuyck, G. M. Whitesides, *Science*, **254**(5034): 981-983 (1991).
116) K Heister, M. Zharnikov, and M. Grunze, *Langmuir*, **17**(1): 8-11 (2001).
117) M. A. Huels, P.C. Dugal, and L. Sanche, *J. Chem. Phys.*, 2003. **118**(24): 11168-11178 (2001).
118) H. U. Müller, M. Zharnikov, B. Völkel, A. Schertel, P. Harder, and M. Grunze, *J. Phys. Chem. B*, **102**(41): 7949-7959 (1998).
119) N. Ballav, C.-H. Chen, and M. Zharnikov, *J. Photopolym. Sci. Tec.*, **21**(4): 511-517 (2008).
120) P. A: Waske, N. Meyerbröker, W. Eck, and M. Zharnikov, *J. Phys. Chem. C*, **116**(25): 13559-13568 (2012).
121) A. Beyer, A. Godt, I. Amin, C. T. Nottbohm, C. Schmidt, J. Zhao, A. Golzhäuser, *Phys. Chem. Chem. Phys.*, **10**(48): 7233-7238 (2008).
122) M. Schnietz, A. Turchanin, C. T. Nottbohm, A. Beyer, H. H. Solak, P. Hinze, T. Weimann, A. Golzhäuser, *Small*, **5**(23): 2651-2655 (2009).
123) A. Turchanin, A. Beyer, C. T. Nottbohm, X. Zhang, R. Stosch, A. Sologubenko, J. Mayer, P. Hinze, T. Weimann, A. Golzhäuser, *Adv. Mat.*, **21**(12): 1233-1237 (2009)
124) C. T. Nottbohm, A. turchanin, A. Beyer, R. Stosch, A. Golzhäuser, *Small*, **7**(7): 874-883 (2011).
125) D. Rhinow, M. Büenfeld, N.-E. Weber, A. Beyer, A. Golzhäuser, W. Kühlbrand, N. Hampp, A. Turchanin, *Ultramicroscopy*, **111**(5): 342-349 (2011).
126) A. Turchanin, D. Weber, M. Büenfeld, C. Kisielowski, M. V. Fistul, K. B. Efetov, T. Weimann, R. Stosch, J. Mayer, and A. Gölzhäuser, *ACS Nano*, **5**(5): 3896-3904 (2011).
127) X. Zhang, C. Neumann, P. Angelova, A. Beyer, and A. Gölzhäuser., *Langmuir*, **30**(27): 8221-8227 (2014).
128) T.A Carlson. Basic Assumptions and Recent Developments in Quantitative XPS. SURFACE AND INTERFACE ANALYSIS, VOL. 4, NO. 4, (1982)
129) P. Bagus, K.Weiss, A. Schertel, C. Wöll, W. Braun, C. Hellwig, C. Jung, *Chem. Phys. Lett.*, **248**, 129-135 (1996).
130) A. Nefedov, C. Wöll in Surface Science Techniques, Springer Science + Business Media, 277-303 (2013).
131) J. Stöhr, NEXAFS spectroscopy, 1st ed. 1992. Corr. 2nd printing, Springer, 2010.
132) N. Ballav, B. Schüpbach, O. Dethlo_, P. Feulner, A. Terfort, M. Zharnikov, J. *Am. Chem. Soc.*, **129**, 15416 (2007).
133) P. Jiang, A. Nion, A. Marchenko, L. Piot, D. Fichou, *J. Am. Chem. Soc.*, **128**, 12390-12391 (2006)
134) Palermo, V., M. Palma, and P. Samori, *Adv. Mat.*, **18**(2): 145-164 (2006).
135) UHV Kelvin Probe Manual, KPTechnology

136) Seong Ho Choi, Chad Risko, M. Carmen Ruiz Delgado, BongSoo Kim, Jean-Luc Brédas, and C. Daniel Frisbie, *J. Am. Chem. Soc*., **132**(12): 4358-4368 (2010).
137) Jeremy M. Beebe, Bongsoo Kim, J. W. Gadzuk, C. Daniel Frisbie, and James G. Kushmerick, *Phys. Rev. Lett*., **97**(2): 026801 (2006).
138) Jeremy M. Beebe, BongSoo Kim, C. Daniel Frisbie, and James G. Kushmerick, *ACS Nano*, **2**(5): 827-832 (2008).
139) BongSoo Kim, Jeremy M. Beebe, Yongseok Jun, X.-Y. Zhu, and C. Daniel Frisbie, *J. Am. Chem. Soc*., **128**(15): 4970-4971 (2006).
140) Rainer Haag, Maria Anita Rampi, R. Erik Holmlin, and George M. Whitesides, *J. Am. Chem. Soc*., **121**(34): 7895-7906 (1999).
141) C. Grave, C. Risko, A. Shaparenko, Y. Wang, C. Nuckols, M. A. Rampi, M. Zharnikov, *Adv. Funct. Mater*., **17**(18): 3816-3828 (2007).
142) Christine Joy Querebillo, Andreas Terfort, David L. Allara, and Michael Zharnikov, *J. Phys. Chem. C*, **117**(48): 25556-25561 (2013).
143) Paul Penner, Xianghui Zhang, Emanuel Marschewski, Florian Behler, Polina Angelova, André Beyer, Jens Christoffers, and Armin Gölzhäuser, *J. Phys. Chem. C*, **118**(37): 21687-21694 (2014).
144) Davide Fracasso, Mutlu Iskender Muglali, Michael Rohwerder, Andreas Terfort, and Ryan C. Chiechi, *J. Phys. Chem. C*, **117**(21): 11367-11376 (2013).
145) H. B. Akkerman, P. W. Blom, D. M. de Leeuw, B. de Boer, *Nature*, **441**(7089): 69-72 (2006).
146) Kilgour, M. and D. Segal, *J Chem Phys*, **143**(2): 024111 (2015).
147) Christian A. Nijhuis, William F. Reus, Jabulani R. Barber, Michael D. Dickey, and George M. Whitesides, *Nano Lett*., **10**(9): 3611-3619 (2010).
148) Wang, W.Y., T. Lee, and M.A. Reed, *Phys. Rev. B*, **68**(3), 035416 (2003).
149) Mirjani, F., J.M. Thijssen, and S.J. van der Molen, *Phys. Rev. B*, **84**(11), 115402, (2011).
150) Tan, A. R., J. Balachandran, B. D. Dunietz, S.-Y. Jang, V. Gavini, and P. Reddy, *Appl. Phys. Lett*., **101**(24), 243107 (2012).
151) de Gennes, P. G. *Rev. Mod. Phys*. **57**, 827 (1985).
152) Tadmor, R. *Langmuir*, **20**, 7659–7664 (2004).
153) Frederick Chesneau, Hicham Hamoudi, Björn Schüpbach, Andreas Terfort, and Michael Zharnikov, *J. Phys. Chem. C*, **115**(11): 4773-4782 (2011).
154) Meyer, E., *Prog. Surf. Sci. Surface Science*, **41**(1): 3-49 (1992).
155) Eaton, P. and P. West, Atomic Force Microscopy. 2010: OUP Oxford. 248.
156) West, P.E., Introduction to Atomic Force Microscopy: Theory, Practice, Applications. 2006.
157) Howland, R.S. and M.D. Kirk, 2.3 - STM and SFM: Scanning Tunneling Microscopy and Scanning Force Microscopy, in Encyclopedia of Materials Characterization. 1992, Butterworth-Heinemann: Boston.
158) Zhou, W. and Z.L. Wang, Scanning microscopy for nanotechnology: techniques and applications. 2007, New York: Springer.
159) adapted from https://www.researchgate.net/figure/The-working-principle-of-an-AFM_fig1_271512657
160) J. Moulder, J. Chastain, Handbook of X-ray Photoelectron Spectroscopy: A Reference Book of Standard Spectra for Identi_cation and Interpreta-tion of XPS Data, Physical Electronics Division, Perkin-Elmer Corporation, Eden Prairie, MN, USA, 1992.

161) R. W. Kwok, XPSPeak 4.1, Department of Chemistry The Chinese University of Hong Kong 1999.
162) H. Kondoh, M. Iwasaki, T. Shimada, K. Amemiya, T. Yokohama, T. Ohta, M. Shimomura, K. Kono, *Phys. Rev. Lett*., **90**, 066102 (2003).
163) F. Chesneau, B. Schüpbach, K. Szel¡gowska-Kunstman, N. Ballav, P. Cyganik, A. Terfort, M. Zharnikov, *Phys. Chem. Chem. Phys*., **12**, 12123 (2010).
164) H. Hamoudi, K. Döring, F. Chesneau, H. Lang, M. Zharnikov, *J. Phys. Chem. C*, **116**, 861 (2012).
165) Batson, P. E. *Phys. Rev. B*, **48**, 2608-2610 (1993).
166) Chiechi, R. C.; Weiss, E. A.; Dickey, M. D.; Whitesides, G. M. *Angew. Chem. Int. Ed.*, **120**, 148–150 (2008).
167) Zharnikov, M.; Grunze, M. *J. Phys.: Condens. Matter*, **13**, 11333−11365 (2001).
168) Hähner, G.; Kinzler, M.; Thümmler, C.; Wöll, Ch.; Grunze, M., *J. Vac. Sci. Technol., A*, **10**, 2758−2763 (1992).
169) Urquhart, S. G.; Ade, H., *J. Phys. Chem. B*, **106**, 8531−8538 (2002).
170) Zharnikov, M., *J. Electron Spectrosc. Relat. Phenom*., **178−179**, 380−393 (2010).
171) Heister, K.; Johansson, L. S. O.; Grunze, M.; Zharnikov, M., *Surf. Sci*., **529**, 36−46 (2003).
172) Derry, G. N.; Kern, M. E.; Worth, E. H., *J. Vac. Sci. Technol. A*, **33**, 060801 (2015).
173) Okajima, T.; Teramoto, K.; Mitsumoto, R.; Oji, H.; Yamamoto, Y.; Mori, I.; Ishii, H.; Ouchi, Y.; Seki, K., *J. Phys. Chem. A*, **102**, 7093-7099 (1998).
174) Ballav, N.; Shaporenko, A.; Krakert, S.; Terfort, A.; Zharnikov, M., *J. Phys. Chem. C,* **111**, 7772-7782 (2007).
175) Frey, S.; Shaporenko, A.; Zharnikov, M.; Harder, P.; Allara, D. L., *J. Phys. Chem. B*, **107**, 7716-7725 (2003).
176) Bolognesi, P.; O'Keeffe, P.; Ovcharenko, Y.; Coreno, M.; Avaldi, L.; Feyer, V.; Plekan, O.; Prince, K. C.; Zhang, W.; Carravetta, V., *J. Chem. Phys*., **133**, 034302 (2010).
177) Lin, Yi-S.; Lin, H.-Ru; Liu, W.-L.; Lee, Y. T.; Tseng, C.-M.; Ni, C.-K.; Liu, C.-L.; Tsai, C.-C.; Chen, J.-L.; Hu, W.-P., *Chem. Phys. Lett*., **636**, 146-153 (2015).
178) Kovalchuk, A.; Abu-Husein, T.; Fracasso, D.; Egger, D. A.; Zojer, E.; Zharnikov, M.; Terfort, A.; Chiechi, R. C., *Chem. Sci*., **7**, 781−787 (2016).
179) Kovalchuk, A.; Egger, D. A.; Abu-Husein, T.; Zojer, E.; Terfort, A.; Chiechi, R. C., *RSC Adv*., **6**, 69479−69483 (2016).
180) Shaporenko, A.; Adlkofer, K.; Johansson, L. S. O.; Tanaka, M.; Zharnikov, M., *Langmuir*, **19**, 4992−4998 (2003).
181) McGuiness, C. L.; Shaporenko, A.; Mars, C. K.; Uppili, S.; Zharnikov, M.; Allara, D. L., *J. Am. Chem. Soc*., **128**, 5231−5243 (2006).
182) McGuiness, C. L.; Diehl, G. A.; Blasini, D.; Smilgies, D.-M.;Zhu, M.; Samarath, N.; Weidner, T.; Ballav, N.; Zharnikov, M.; Allara, D. L., *ACS Nano*, **4**, 3447−3465 (2010).
183) A. Petritz, M. Krammer, E. Sauter, M. Gärtner, G. Nascimbeni, B. Schrode, A. Fian, H. Gold, A. Cojocaru, E. Karner-Petritz, R. Resel, A. Terfort, M. Zharnikov, E. Zojer, K. Zojer, and B. Stadlober, *Adv. Funct. Mater., in press*.
184) Kang, J. F.; Ulman, A.; Liao, S.; Jordan, R.; Yang, G. H.; Liu, G. Y., *Langmuir*, **17**, 95–106 (2001).
185) Cabellos, J. L.; Mowbray, D. J.; Goiri, E.; El-Sayed, A.; Floreano, L.; de Oteyza, D. G.; Rogero, C.; Ortega, J. E.; Rubio, A., *J. Phys. Chem. C*, **116**, 17991-18001 (2012).

186) El-Sayed, A.; Borghetti, P.; Goiri, E.; Rogero, C.; Floreano, L.; Lovat, G.; Mowbray, D. J.; Cabellos, J. L.; Wakayama, Y.; Rubio, A.; Ortega, J. E.; de Oteyza, D. G., *ACS Nano*, **7**, 6914-6920 (2013).

187) Horsley, J.; Stöhr, J.; Hitchcock, A. P.; Newbury, D. C.; Johnson, A. L.; Sette, F. *J. Chem. Phys*., **83**, 6099-6107 (1985).

188) Yokoyama, T.; Seki, K.; Morisada, I.; Edamatsu, K.; Ohta, T., *Phys. Scr*., **41**, 189-192 (1990).

189) Frey, S.; Stadler, V.; Heister, K.; Eck, W.; Zharnikov, M.; Grunze, M.; Zeysing, B.; Terfort, A. *Langmuir*, **17**, 2408-2415 (2001).

190) Zharnikov, M.; Frey, S.; Heister, K.; Grunze, M., *J. Electron Spectr. Relat. Phenom.,* **124**, 15-24 (2002).

191) Zharnikov, M.; Kuller, A.; Shaporenko, A.; Schmidt, E.; Eck, W., *Langmuir*, **19**, 4682-4687 (2003).

192) Wu, K.-Y.; Yu, S.-Y.; Tao, Y.-T., *Langmuir*, **25**, 6232–6238 (2009).

193) Rissner, F.; Egger, D. A.; Romaner, L.; Heimel, G.; Zojer, E., *ACS Nano*, **4**, 6735–6746 (2010).

194) Chen, C.-Y.; Wu, K.-Y.; Chao, Y.-C.; Zan, H.-W.; Meng, H.-F.; Tao, Y.-T., *Org. Electron.*, **12**, 148–153 (2011).

195) E. Sauter, C.-O. Gilbert, J.-F. Morin, A. Terfort, and M. Zharnikov, *J. Phys. Chem. C, in press.*

196) Ishida, T.; Choi, N.; Mizutani, W.; Tokumoto, H.; Kojima, I.; Azehara, H.; Hokari, H.; Akiba, U.; Fujihira, M., *Langmuir*, **15**, 6799−6806 (1999).

197) Weiler-Feilchenfeld, H.; Bergmann, E. d., *Isr. J. Chem*., **6**, 823−826 (1968).

198) Blackman, G. L.; Brown, R. D.; Burden, F. R., *J. Mol. Spectrosc*., **35**, 444−454 (1970).

199) Yildirim, C.; Sauter, E.; Terfort, A.; Zharnikov, M., *J. Phys. Chem. C*, **121**, 7355−7364 (2017)

200) Yildirim, C.; Füser, M.; Terfort, A.; Zharnikov, M. *J. Phys. Chem. C*, **121**, 567−576 (2017).

201) Zubavichus, Y.; Zharnikov, M.; Yang, Y.-J.; Fuchs, O.; Heske, C.; Umbach, E.; Ulman, A.; Grunze, M., *Langmuir*, **20**, 11022−11029 (2004).

202) Lukasczyk, T.; Schirmer, M.; Steinrück, H.-P.; Marbach, H., *Small*, **4**, 841−846 (2008).

203) Walz, M.-M.; Schirmer, M.; Vollnhals, F.; Lukasczyk, T.; Steinrück, H.-P.; Marbach, H., *Angew. Chem., Int. Ed*., **49**, 4669−4673 (2010).

204) Kankate, L.; Turchanin, A.; Gölzhäuser, A., *Langmuir*, **25**, 10435−10438 (2009).

205) Schilp, S.; Ballav, N.; Zharnikov, M., *Angew. Chem., Int. Ed*., **47**, 6786−6789 (2008).

206) Brondijk, J. J.; Li, X.; Akkerman, H. B.; Blom, P. W. M.; de Boer, B., *Appl. Phys. A: Mater. Sci. Process.*, **95**, 1−5 (2009).

207) Watanabe, T.; Fujihira, M., *Ultramicroscopy*, **109**, 1035−1039 (2009).

208) Rentenberger, S.; Vollmer, A.; Zojer, E.; Schennach, R.; Koch, N., *J. Appl. Phys*., **100**, 053701 (2006).

209) E. Sauter, C. Yildirim, A. Terfort, and M. Zharnikov, *J. Phys. Chem. C*, **121** (23), pp 12834–12841 (2017)

210) von Wrochem, F.; Gao, D.; Scholz, F.; Nothofer, H. G.; Nelles, G.; Wessels, J. M., *Nat. Nanotech*., **5**, 618-624 (2010).

211) Park, J.-S.; Vo, A. N.; Barriet, D.; Shon, Y. S.; Lee, T. R., *Langmuir*, **21**, 2902–2911 (2005).

212) Weidner, T.; Ballav, N.; Siemeling, U.; Troegel, D.; Walter, T.; Tacke, R.; Castner, D. G.; Zharnikov, M., *J. Phys. Chem. C*, **113**, 19609–19617 (2009).

213) Sander, F.; Peterle, T.; Ballav, N.; von Wrochem, F.; Zharnikov, M.; Mayor, M., *J. Phys. Chem. C*, **114**, 4118–4125 (2010).

214) Lindner, M.; Valášek, M.; Homberg, J.; Edelmann, K.; Gerhard, L.; Wulfhekel, W.; Fuhr, O.; Wächter, T.; Zharnikov, M.; Kolivoška, V.; *et al*., *Chem. Eur. J*., **22**, 13218–13235 (2016).

215) Chesneau, F.; Zhao, J.; Shen, C.; Buck, M.; Zharnikov, M., *J. Phys. Chem. C*, **114**, 7112–7119 (2010).

216) Ford, W. E.; Abraham, F.; Scholz, F.; Nelles, G.; Sandford, G.; von Wrochem, F., *J. Phys. Chem. C*, **121**, 1690–1703 (2017).

217) Plashkevych, O.; Snis, A.; Yang, L.; Ågren, H.; Matar, S. F., *Phys. Scripta*, **63**, 70-86 (2001).

218) Zubavichus, Y.; Zharnikov, M.; Shaporenko, A.; Grunze, M., *J. Electron Spectrosc. Relat. Phenom*., **134**, 25-33 (2004).

219) Plashkevych, O.; Yang, L.; Vahtras, O.; Agren, H.; Pettersson L. G. M., *Chem. Phys.*, **222**, 125-137 (1997).

220) Hitchcock, A. P.; Fisher, P.; Gedanken, A.; Robin M. B., *J. Phys. Chem*. **91**, 531-540 (1987.)

221) Zhang, Z.; Wächter, T.; Kind, M.; Schuster, S.; Bats, J. W.; Nefedov, A.; Zharnikov, M.; Terfort, A., *ACS Appl. Mater. Interfaces*, **8**, 7308–7319 (2016).

Acknowledgements

I would like to thank my supervisor Prof. (apl.) Dr. Michael Zharnikov for giving me this great opportunity and the possibility to conduct research in such an interesting and versatile topic. I also want to thank him for all his support and advice during the last three years.

Many thanks to Prof. (apl.) Dr. H.-R. Volpp for taking the position as the second referee.

I would also like to thank all of my co-workers, with whom it has been a pleasure to work together. This includes all former and actual members of the Group, namely Swen Schuster, Tobias Wächter, Can Yildirim, Mustafa Sayin, and Yan Rui as well as the technical staff of our institute: Günter Meinusch, Peter Jeschka and Reinhold Jehle. Thank you for all the interesting discussions and valuable support in my PhD time.

I am thankful to our colleagues from all over the world, who collaborated with our group in various projects: from the Frankfurt University, the group of Prof. Dr. A. Terfort, who provided most of the SAM precursors for our experiments, especially M. Gärtner, A. Wiesner, Dr. M. Kind, Dr. M. Bolte and T. Abu Husein; Dr. Florian von Wrochem from Sony Deutschland GmbH; Prof. Dr. S. Ludwigs and D. Treftz from the Stuttgart University; the group of Prof. J.-F. Morin from the Université Laval, Quebec, Canada and his group members C.-O. Gilbert and J. Boismenu-Lavoie for their cooperation and the synthesis of the aliphatic esters. Additionally I want to thank our collaboratours from Austria, viz. the groups from the TU Graz, Prof. E. Zojer and G. Nascimbeni; Dr. K. Zojer and M. Krammer, as well as Dr. Roland Resel for their supplementary experiments and theoretical calculations; the Johanneum Research, Weiz, Austria, with Dr. B. Stadlober, Dr. A. Petritz, A. Fian, Dr. H. Gold, A. Cojocaru and E. Karner-Petritz for the device experiments in the framework of the joint project.

I would also like to thank the HZB staff for the allocation of the beamtimes at the German synchrotron radiation facility, BESSY II in Berlin, and the BESSY II staff for their technical support during the experiments at the synchrotron. I also want to acknowledge Dr. A. Nefedov and Prof. Dr. Ch. Wöll for the technical cooperation at the HE-SGM beamline at Bessy II.

Thanks goes to the German Research Society (DFG) for financially supporting this work as part of a joint project within the D-A-CH framework.

Thanks goes to my family, for always supporting me and helping me to reach my goals.

Finally yet importantly, my deepest gratitude for all the support and that she always had faith in me and my abilities goes to my wife Désirée.